University of California
Santa Barbara

Polymeric vehicles for the optimal delivery of synergistic chemotherapeutics

A dissertation submitted in partial satisfaction
of the requirements for the degree

Doctor of Philosophy
in
Chemical Engineering

by

Douglas R. Vogus

Committee in charge:

Professor Samir Mitragotri, Chair
Professor Todd Squires
Professor Matt Helgeson
Professor Leslie Wilson

September 2017

The Dissertation of Douglas R. Vogus is approved.

Professor Todd Squires

Professor Matt Helgeson

Professor Leslie Wilson

Professor Samir Mitragotri, Committee Chair

June 2017

Polymeric vehicles for the optimal delivery of synergistic chemotherapeutics

by

Douglas R. Vogus

Acknowledgements

I would like to take this opportunity to thank all of those who have helped me throughout my time leading up to and during graduate school. Your support has helped guide me to where I am today.

First, to my graduate school advisors, I thank you both for being so supportive and patient during graduate school. You both gave me the time and space to explore projects that I was personally interested in and were always willing to help. Samir, thank you for teaching me how to ask the right questions and to always be aware of the big picture. Todd, thank you for teaching me how to think about complicated physical systems and the importance of being creative in science. Both of your enthusiasm for research, made it much more enjoyable to keep working when research became challenging.

Next, to my undergraduate professors Prof. Wakabayashi and Prof. Vogel. You both encouraged me to go to graduate school, and I am grateful to you that I made this decision.

To my labmates in Samir's lab, thank you for keeping lab interesting and being always willing to help. To Anusha, Vinu, and Max, thank you for helping me with animal studies. Your help made it possible for me to still have a life during these long studies. To Michael and Alexandra, thank you for helping me with and teaching me chemistry. Your assistance helped me overcome many roadblocks that I ran into during my Ph.D. To Gwen, thank you for your help with cryo TEM. To Kat, thank you for teaching me many techniques in lab and giving me assistance throughout the early years of graduate school. You were always willing to help, and you provided the foundation for many of my projects. To Aaron, thank you for helping me get involved with many projects early on and for paying for my parking pass. To Renwei, thank you for always being willing to provide your expertise with regards to cell culture, molecular biology, and *in vivo* studies.

To my labmates in Todd's lab, I am equally grateful for you assistance. To Vincent, Joel,

and Rodrigo, thank you for teaching me microfluidics. To Vincent, I really appreciated your help while we worked on interferometry together. To Craig, thank you for doing experiments on various projects the past few years without complaining too much. To Arash and Anirudha, thank you for helping me with various experiments in lab.

To Nick, John, Geoff, Kelsey, Ali (not Allie), Rodrigo, Ian, Anirudha, Arash, and the many other friends that I have made here at UCSB, thank you all for making the past 5 years a lot of fun. Between going surfing, brewing beer, playing basketball, and going out downtown, my time here has been a blast. While doing research was often not fun, I never had a dull moment outside of lab. To Maggie, thank you for making the past year a great one and for always making me laugh. I am excited to have an excuse to come back to surf in Santa Barbara next year.

Most importantly, I would like to thank my family for being so supportive of me growing up and during graduate school. Your support has made it possible for me to pursue anything that I want to. To dad, thank you for always being interested in my research and agreeing to go on (and funding) many ski trips while I lived out west. To mom, thank you for sending me all the cookies and candy during graduate school. To Nicole and Jill, thank you for coming out to visit me, and, sorry, but I will always be mom's favorite.

Curriculum Vitæ

Douglas R. Vogus

Education

2012-2017	**Ph.D. in Chemical Engineering** (Expected) University of California, Santa Barbara, CA
2008-2012	**B.S. in Chemical Engineering** Bucknell University, Lewisburg, PA

Professional Experience

2012-2017	**Graduate Researcher and Teaching Assistant** University of California, Santa Barbara, CA
2010-2012	**Undergraduate Researcher and Teaching Assistant** Bucknell University, Lewisburg, PA.
2011	**Process Engineering Intern** First Quality Tissue, Lock Haven, PA
2010	**Undergraduate Researcher** Carnegie Mellon University, Pittsburgh, PA.

Publications and Patents

- **Vogus, D.R.**, Evans, M.A., Pusuluri, A., Krishnan, V., Menegatti, S., Zhang, M., Nowak, M., & Mitragotri, S. (2017). A hyaluronic acid conjugate engineered to synergistically deliver gemcitabine prior to doxorubicin to treat triple negative breast cancer. *Submitted* to *Journal of Controlled Release*.
- **Vogus, D.R.**, Angulo, C.D., Banerjee, A., Nowbahar, A., & Squires, T.M. (2017). Measuring the effect of molecular adsorption on transport in PEG diacrylate hydrogels. *In prep.*
- **Vogus, D.R.**, Krishnan, V., & Mitragotri, S. (2017). Review: The effectiveness of polymer drug conjugates in delivering combinations of chemotherapeutic agents. *In review* at *Current Opinion in Colloid & Interface Science*.
- **Vogus, D.R.**, Gregory, J., Barajas, A., Lahann, J., & Mitragotri, S. (2017). Bi-phasic polymeric nanoparticles to synergistically deliver lapatinib prior to paclitaxel. *In prep.*
- **Vogus, D.R.**, Mansard, V., Rapp, M.V., & Squires, T.M. (2015). Measuring concentration fields in microfluidic channels in situ with a FabryPerot interferometer. *Lab on a Chip, 15*(7), 1689-1696.
- Camacho, K.M., Menegatti, S., Kumar, S., **Vogus, D.R.**, & Mitragotri, S. Polymer-Drug Conjugates for Combination Anticancer Therapy PCT/US2016/021587.

- Sanoja, G.E., **Vogus, D.R.**, Mitragotri, S., & Segalman, R.A. (2017) Magnetic and Biocompatible Polymers as 1H Nuclei Relaxation Agents for Magnetic Resonance Imaging. *Submitted.*
- Camacho, K.M., Menegatti, S., **Vogus, D.R.**, Pusuluri, A., Fuchs, Z., Jarvis, M., Zakrewski, M., Evans, M. A., Chen, R., & Mitragotri, S. (2016). DAFODIL: A novel liposome-encapsulated synergistic combination of doxorubicin and 5FU for low dose chemotherapy. *Journal of Controlled Release, 229*, 154-162.
- Camacho, K.M., Kumar, S., Menegatti, S., **Vogus, D.R.**, Anselmo, A.C., & Mitragotri, S. (2015). Synergistic antitumor activity of camptothecindoxorubicin combinations and their conjugates with hyaluronic acid. *Journal of Controlled Release, 210*, 198-207.
- Anselmo, A.C., Zhang, M., Kumar, S., **Vogus, D.R.**, Menegatti, S., Helgeson, M.E., & Mitragotri, S. (2015). Elasticity of nanoparticles influences their blood circulation, phagocytosis, endocytosis, and targeting. *ACS nano, 9*(3), 3169-3177.
- Anselmo, A.C., Modery-Pawlowski, C.L., Menegatti, S., Kumar, S., **Vogus, D.R.**, Tian, L.L., Chen, M., Squires, T.M., Sen Gupta, A., & Mitragotri, S. (2014). Platelet-like nanoparticles: mimicking shape, flexibility, and surface biology of platelets to target vascular injuries. *ACS Nano, 8*(11), 11243-11253.
- Alvarez, N.J., **Vogus, D.R.**, Walker, L.M., & Anna, S.L. (2012). Using bulk convection in a microtensiometer to approach kinetic-limited surfactant dynamics at fluidfluid interfaces. *Journal of Colloid and Interface Science, 372*(1), 183-191.

Presentations

- **Vogus, D.R.** & Mitragotri, S. Engineering polymer drug conjugates to synergistically schedule chemotherapeutics, AIChE Annual Meeting, Nov 13-18, 2016; San Francisco, CA, USA. *Oral*.
- **Vogus, D.R.** & Mitragotri, S. Engineering polymer drug conjugates to synergistically schedule gemcitabine and doxorubicin, Gordon Research Conference and Symposium: Drug Carriers in Medicine and Biology, Aug 6-12, 2016; Waterville Valley, NH, USA. *Poster*.
- **Vogus, D.R.**, Camacho, K.C., & Mitragotri, S. Polymer drug conjugates for the delivery of synergistic chemotherapeutics, ECI Nanotechnology in Medicine: From Molecules to Humans, July 3-7, 2016; Hernstein, Austria. *Oral*.
- **Vogus, D.R.**, Mansard, V., Rapp, M.J., & Squires, T.M. Measuring concentration fields in microfluidic channels in situ with a Fabry-Perot interferometer, AIChE Annual Meeting, Nov 8-13, 2015; Salt Lake City, UT, USA. *Oral*.

Honors and Awards

2012-2017	National Science Foundation Graduate Research Fellowship (NSF GRFP)
2009-2012	Presidents Award for Distinguished Academic Achievement, Bucknell University (Highest GPA)

Abstract

Polymeric vehicles for the optimal delivery of synergistic chemotherapeutics

by

Douglas R. Vogus

Combination chemotherapy is the current gold standard for treating advanced malignancies, but treatment is often limited by systemic toxicity. Polymeric delivery vehicles have emerged as a useful tool to deliver chemotherapeutics with greater tumor selectivity and reduced healthy tissue toxicity than standard chemotherapy. As a result, many nano-sized polymeric systems containing a single drug have recently entered clinical trials for the treatment of advanced cancers; however, few have been approved due to lack of improvements in tumor regression. This thesis focuses on engineering more therapeutically active polymeric vehicles by optimally delivering combinations of synergistic chemotherapy drugs. Polymer drug conjugates and bi-phasic nanoparticles are engineered to precisely deliver synergistic drugs, and I show that relative drug release rates govern the therapeutic activity of a given combination delivery vehicle. I further show that combination polymer drug conjugates can effectively inhibit the growth of an aggressive, orthothopic tumor model *in vivo* more effectively than single drug conjugates and the free drug combination. The conjugates are capable of preventing tumor growth through various parenteral administration routes, motivating future development for clinical translation.

In addition to new vehicle development, continued improvements in therapeutic activity rely on fundamentally understanding the mechanisms by which vehicles interact with biological systems and release their therapeutic payloads. In the latter part of this thesis, I develop a microfluidic technique capable of measuring concentration profiles with high spatio-temporal resolution. The technique is used to measure the transport of a model drug in hydrogels. I show

that interactions between the polymeric mesh and the solute significantly impact solute transport and resulting drug release properties. Understanding the physical mechanisms in which drugs interact with their carrier can govern drug release kinetics and is critical for the future development of effective polymeric delivery vehicles.

Contents

Chapter 1

Overview of dissertation

Pharmaceutical companies spend billions of dollars in research to bring a single therapeutic compound to the market. The astronomical costs associated with drug development is often attributed to the failure to translate compounds which were effective on the bench top to the patient. For example, approximately only 10 % of all drugs entering Phase I clinical trials reach approval status [1]. Fortunately, new therapies can effectively treat diseases without getting a new drug approved by delivering the current therapeutic options more effectively.

The field of drug delivery focuses on improving the administration of existing drugs to improve treatment efficacy in various diseases. While each disease offers a unique challenge, a common goal of all delivery vehicles is to deliver the therapeutic agent to the disease site while minimizing negative side effects on the patient. The development of an effective delivery vehicle requires optimizing the loading and release of therapeutics and how the vehicle interacts with the patient's body. Broadly, my Ph.D. research has focused on developing new drug delivery vehicles for cancer therapy and fundamentally understanding how current delivery systems release their therapeutic payloads.

In this thesis, I first discuss the development of new delivery vehicles to deliver combinations of chemotherapeutic agents for the treatment of late stage cancer (Chapters 2-6).

In Chapter 2, I provide background information on combination chemotherapy, the use of nanomedicine in cancer, and the application of polymeric carriers to co-deliver multiple drugs. In Chapter 3, I summarize the experimental methods used in this thesis, including *in vitro* and *in vivo* assays, chemical synthesis, and material characterization techniques. In Chapter 4, I screen through different drug pairs to identify synergistic drugs to deliver together, and study how schedule impacts drug synergy. I proceed to discuss the development of two different delivery systems: polymer drug conjugates (Chapter 5) and bi-phasic polymeric nanoparticles (Chapter 6) for the co-delivery of synergistic chemotherapy drug pairs.

I then discuss the development of a new experimental, microfluidic technique which is capable of measuring drug release in future research (Chapters 7-8). In Chapter 7, the microfluidic technique is characterized with respect to its ability to measure solute concentration with high spatio-temporal resolution. In Chapter 8, the technique is used to measure solute transport in PEG hydrogels to develop more accurate physical models for solute transport in gels.

I conclude the thesis in Chapter 9 by summarizing the main findings of this research. I also offer insight into future research pathways which can build upon the knowledge which was gained in this dissertation.

Permissions and Attributions

1. Some content in Chapter 2 has been adapted from a review article which is currently in review at *Current Opinion in Colloid & Interface Science*.

2. The content of Chapter 5 has been submitted to the *Journal of Controlled Release* for review.

3. The content of Chapter 6 is the result of a collaboration with Jason Gregory from the Lahann lab at the University of Michigan.

4. The content of Chapter 7 has previously appeared in *Lab on a Chip*. The chapter is adapted from Ref. [2] with permission from The Royal Society of Chemistry.

Chapter 2

Combination chemotherapy and nanomedicines in cancer

2.1 The use of combination chemotherapy

Cancer places a significant medical and financial burden on society; therefore, it continues to remain an active area of scientific research. Being as two in every five people will be diagnosed with a form of invasive cancer during their lifetime, almost every individual is affected by cancer in some manner [3]. Although mortality rates have been on a steady decline since 1990, additional treatment options must be developed to exacerbate this process as cancer remains the second leading cause of death in the United States, following cardiovascular disease [4].

While each cancer subtype has distinct characteristics, a unifying characteristic of all cancer cells is uncontrolled growth and proliferation [5]. The same general processes are typically responsible for uncontrolled growth in cancer, even though cancer evolves from different oncogenes [6]. Due to vast pathological and genetic differences when comparing different types of cancer, many treatments have been developed, including surgical resection, chemotherapy,

radiation, targeted therapies, and immunotherapies. The success of a given treatment is determined by its ability to eradicate tumor cells, prevent the relapse of future tumor cell proliferation, and minimize healthy tissue toxicity.

Systemic chemotherapy is commonly employed singularly or in combination with other therapies for all types of cancer, due to its ability to target fast proliferating cells. However, tumor cells are often unresponsive to single chemotherapy drugs. While some cells show resistance to therapies at the onset of treatment, other cells, which are initially responsive to therapy, develop increasing levels of resistance throughout the treatment [7]. Various mechanisms of acquired drug resistance at both the cellular and tissue level have been identified in different types of cancer and therapies [7]. Both upstream processes, such as over-expression of protein pumps and overactive metabolic processes, and downstream processes, such as the inhibition of apoptotic pathways and the activation of prosurvival signals, can limit the cytotoxicity of accumulated drug [8, 9].

To overcome the development of drug resistance, combinations of chemotherapy drugs with different cytotoxic mechanisms are commonly used in an attempt to improve therapeutic outcome. Consistent throughout all types of cancer, combination chemotherapy is commonly employed as front line therapy or as a last resort to treat late stage cancer subtypes [10, 11, 12, 13, 14]. Unfortunately, while patients tumors often respond to combination chemotherapy, overall efficacy is limited due to increased toxicity associated with the combination treatment [15].

2.2 Synergy in combination chemotherapy

The methodology behind using a combination of drugs is that drug combinations can overcome various mechanisms of drug resistance and/or demonstrate enhanced antitumor activity compared to single drugs. This includes combining traditional small molecule therapeu-

tics with other small molecule drugs or biologics [16]. In theory, combination chemotherapy should allow oncologists to administer lower drug doses leading to less side effects [17]. Unfortunately, in the clinic, many combination treatments demonstrate increased toxicity with minimal improvement in tumor reduction [15].

To reduce systemic toxicity, many researchers have identified drug pairs which work favorably together *in vitro*. Drugs which enhance the activity of one another are commonly referred to synergistic, while those which do not work favorably together are referred to as antagonistic [18, 19, 20, 21]. Fundamentally, synergism will result when one drug enhances the performance of another drug through some molecular mechanism. For example, if one inhibitor enhances the binding of another inhibitor, the two drugs would be considered synergistic [22]. Although it would be convenient to be able to predict synergistic drug pairs in cancer simply from mechanism alone, this is not possible due to the vast differences in cancer cell response to chemotherapeutic agents [23]. For this reason, an empirical approach is commonly taken to identify synergistic drug pairs. This approach is described in detail mathematically in Chapter 3. *In vitro* studies demonstrate that drug synergy is dependent upon many variables including the molar ratio of the drugs in the combination [21]; therefore, precision is required in translating these synergistic drug pairs effectively to the clinic.

In the clinic, doctors will typically administer each drug in a combination, similar to how the individual drugs are administered with monotherapy. Monotherapy dosing and scheduling is based upon the maximum tolerated dose (MTD) determined during preclinical and clinical trials [24, 25]. Because dosing is optimized for single drugs, the potential benefits from using the combination of drugs may not be realized due to sub-optimal drug dosing regimes. For example, shown schematically in a cartoon in Fig. 2.1, lower drug doses can be effective when the drug pair is administered in a synergistic ratio; however, a high drug dose must still be administered if the drugs are given in an antagonistic ratio.

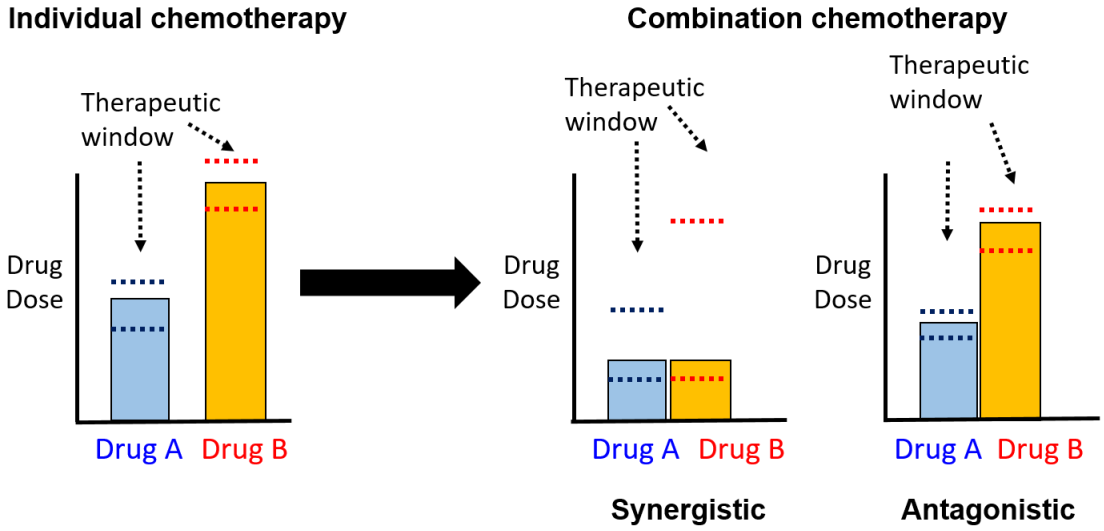

Figure 2.1: Cartoon demonstrating how the therapeutic window can be increased by using a synergistic drug pair

2.3 Scheduling in combination chemotherapy

Many variables contribute to whether a combination of drugs enhances antitumor activity, including the dose of each drug and the schedule in which the drugs are administered. The majority of combination studies examine the effect of drug ratio on synergy during concurrent drug exposure [21], while less *in vitro* studies study the impact of drug exposure schedule on synergy. Fundamental cancer cell biology is now presented, placing an emphasis on why drug administration schedule should significantly impact the efficacy of a given treatment. Furthermore, examples of *in vitro* studies which have studied scheduling in combination chemotherapy are presented.

2.3.1 Time-dependent processes in combination chemotherapy

While drug schedule is often overlooked, many time dependent cellular processes exist which impact cellular response to different drug schedules. In particular, the progression of the

cell cycle, induction of cell death, and development of drug resistance are all processes that are critical to the efficacy of a given treatment. The time scales of these processes occur on the order of minutes to days, which give further motivation that drug scheduling is critical to the success of a given treatment.

Cell cycle progression and cell death

Cell growth, replication, and death are all highly regulated processes controlled by the progression of the cell cycle. The cell cycle consists of four stages and the progression is regulated by a family of proteins, cyclin dependent kinases (CDKs). Two primary checkpoints are in place in the cell cycle: between the first gap phase (G1) and DNA synthesis stage (S) and between the second gap phase (G2) and mitotic stage (M). Typically in cancer, abnormalities in the CDKs, cyclins, CDK activating enzymes, CDK inhibitors, and/or CDK substrates disrupt these regulated processes and induce uncontrolled cell division [26].

Many toxic cancer drugs target specific stages of the cell cycle. In the body, healthy, somatic cells are usually in a reversible quiescent state (G0 phase) until exposure to mitogenic signals trigger reentry into the cell cycle and cell division [6]. Therefore, cancer drugs commonly target cells in the S or M phase to reduce side effects because a higher fraction of cancer cells are in these stages as compared to healthy cells [27].

In order for a chemotherapy drug to be effective, it must disrupt the uncontrolled proliferation, which requires either inducing cellular senescence or cell death. On a fundamental level, many different molecular pathways evoking cell death have been identified including necrosis, intrinsic and extrinsic apoptosis, and autophagic induced cell death [28]. Typically, the effectiveness of chemotherapy can be correlated to the ability to induce apoptosis in cancer cells; however, evading apoptosis is one of the main hallmarks of a cancer cell [29, 5]. The molecules involved in regulating apoptosis are often also involved in the progression of the cell cycle and temporally cycling [30]; therefore, the timing in which a drug is given can have a significant

impact on outcome.

Development of cancer drug resistance

The success of chemotherapy is often dependent upon avoiding the development of drug resistance and targeting cells which are already resistant to specific therapeutics. Often times, the mechanisms involved with drug resistance include complicated regulatory networks with nonlinear dynamics; therefore, drug scheduling also plays a significant role in the development of drug resistance and efficacy of treating resistant cancer cells [31, 32].

For example, tumor cells have shown the ability to acquire drug resistance though the expression of membrane drug pumps. Specifically, the overexpression of ATP-dependent transporters is known to induce multidrug resistance in cancer cells by increasing the efflux of small, hydrophobic molecules, such as doxorubicin [8]. One common member of the family, P-glycoprotein 1 (P-gp), is commonly associated with multidrug resistance and is responsible for cellular resistance to doxorubicin treatment [33]. Acute exposure to doxorubicin increase the expression of P-gp both *in vitro* and *in vivo* [34, 35, 36]. The overexpression is dependent upon both drug concentration and exposure time [37]. After drug exposure, P-gp expression either returns to an initial state to reestablish homeostasis or maintains the elevated levels [35, 36]. Due to the complicated interactions between P-gp expression and DOX exposure, it is likely that schedule will have a significant impact on clinical efficacy for this drug-cell pair.

2.3.2 *In vitro* studies examining the effect of drug schedule on synergy

When considering cellular response to a drug, a temporal profile of various signaling molecules develop which then become responsible for carrying out different cellular tasks, such as promoting cell death or evoking the induction of drug resistance [38]. In cancer, these processes often behave in an uncontrolled and unpredictable manner. Although it seems plau-

sible that there exists an optimal sequence in which a drug or pair of drugs can be given, this sequence is not something that can be predicted *a priori*; therefore, *in vitro* experiments provide a useful tool to understand how cancer cells respond to various therapies.

Many *in vitro studies* have demonstrated that the synergy of a chemotherapy drug combination is dependent upon drug administration schedule (Table 2.1). For each drug pair and cell line, sequential drug exposure (Drug A$\Rightarrow$ Drug B versus Drug B $\Rightarrow$ Drug A) was compared to concurrent drug exposure. Many times, the sequential exposure of one drug (hours to days) prior to another drug significantly enhanced the activity of the drug combination [39, 40, 41]. In addition, some drugs which were antagonistic when given concurrently, were found to be synergistic when given sequentially, motivating the importance of understanding drug scheduling in combination treatment. Many common mechanisms were found to be responsible for the schedule-dependent synergy, typically involving apoptosis [32, 42, 43] or a cell cycle mediated effect [44, 45].

While many of these studies show mechanistically that schedule impacts drug synergy *in vitro*, the majority fail to discuss how this synergy translates to *in vivo* conditions. Furthermore, a discussion on how the synergistic schedules can be translated to a clinical setting is required to fully understand the utility of the drug combination. An emphasis on both identifying synergistic drug pairs and designing therapies to translate this synergy to the clinic is a necessity to take advantage of the benefits of using combinations of chemotherapeutic agents.

2.4 Drug delivery vehicles in oncology

While effective for various cancers and stages, traditional chemotherapy is severely limited by systemic toxicity. The majority of chemotherapy drugs are administered intravenously, and then distribute throughout the body, with minimal preference to accumulate at the tumor site. Recent advances in the fields of drug delivery and nanotechnology have made it possible

Table 2.1: Examples of *in vitro* tumor cell studies identifying schedule dependent combination synergy

First author, year	*Cancer*	*Synergistic schedule*	*Proposed mechanism*
Amadori, 1996[39]	Breast	Doxorubicin (4h) ⇒ Paclitaxel (24 h)	-
Budman, 2000[46]	Breast	Vinorelbine (48-72 h) ⇒ Paclitaxel	-
Cheng, 2011[44]	Lung	Paclitaxel (24 h) ⇒ Gefitinib (48 h)	Increase in pEGFR induced by paclitaxel inhibited by Gefitinib
Chou, 1996[40]	Breast	Edatrexate (3 h) ⇒ Taxol	-
Kano, 1998[47]	Breast, ovarian, colon, and lung	Paclitaxel (24 h) ⇒ Methotrexate (24 h)	-
Lee, 2012[32]	Breast	Erlotinib (24 h) ⇒ Doxorubicin	Reactivation of extrinsic apoptotic pathway by inhibition of EGFR
McHugh, 2007[48]	Bladder	Lapatinib (24 h) ⇒ Gemcitabine or Cisplatin (24 h)	-
Oliveras-Ferraros, 2008[42]	Breast	Paclitaxel (24 h) ⇒ Gemcitabine (48 h)	Increase in Bcl-2 family, inducing more apoptosis
Perez, 1993[41]	Lung	Edatrexate (3 h) ⇒ Cisplatin	-
Takahashi, 2002[45]	Breast	Paclitaxel (24 h) ⇒ Ecteinascidin 743 (72 h)	Accumulation into G1 phase after first exposure, increasing toxicity of 2nd drug
Tanaka, 2005[43]	Gastric, tongue	Pactlitaxel (24 h) ⇒ Oxaliplatin	Induction of G2 arrest, followed by increase in apoptosis in sub G2 phase

to deliver chemotherapeutic agents within a nano-sized delivery vehicle which preferentially delivers more drug to the tumor site. In addition, more recently, there has been a significant focus on delivering multiple therapeutics in a single delivery vehicle to increase the potency of the delivered therapeutic payload.

2.4.1 Nanomedicines in oncology

In 1995, the first FDA approved nanodrug (Doxil®) was approved for the treatment of AIDS-related Kaposis sarcoma [49]. Doxil®, which is a liposomal formulation of doxorubicin, accumulated more at the tumor site and was more tolerable in patients than free doxorubicin. Based on early success, Doxil® has subsequently been approved to treat other advanced malignancies.

Since the early development of Doxil®, researchers have developed many other nano-sized delivery vehicles to carry chemotherapeutic agents (Fig. 2.2). The delivery vehicles consist of both polymeric, lipid, and inorganic material scaffolds, and drugs are both physically entrapped within the vehicles or chemically conjugated. While each delivery vehicle is unique, many of the nano-sized delivery systems distribute in the body and are cleared through similar clearance pathways. In order for a delivery vehicle to be effective, it needs to both circulate for extended periods of time and to target tumor tissue either through passive or active mechanisms.

Contrary to small molecule therapeutics, most nano-sized delivery vehicles are too large to be cleared renally because the glomerular epithelium cutoff is approximately 4 to 6 nm. Therefore, the majority of nanoparticles are cleared by the reticuloendothelial system (RES). By avoiding fast uptake by the RES, particles can circulate for extended periods of time in the body, giving more opportunity for the particles to accumulate at the tumor site. Strategies to avoid RES clearance include coating particle surfaces with polyethylene glycol (PEG) or hyaluronic acid (HA) [51] or modifying physical properties such as size, shape, and flexibility [52, 53].

Delivery vehicles which circulate for extended periods of time have the ability to accumulate in solid tumors passively through the Enhanced Permeability and Retention (EPR) effect [54, 55]. The tumor vasculature in solid tumors is highly irregular leading to large gaps between the endothelial cells lining the tumor vasculature and poor lymphatic drainage due to uniform

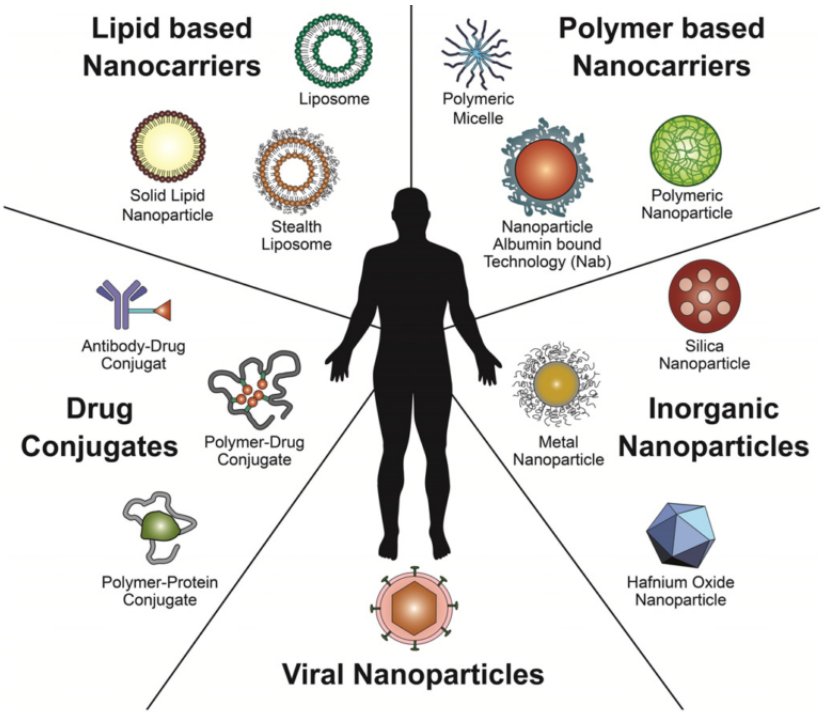

Figure 2.2: Types of nano-sized delivery vehicles used in oncology. Reprinted from [50], with permission from Elsevier.

interstitial fluid pressure throughout the tumor and the lack of lymphatic vessels (Fig. 2.3). Due to these irregularities, macromolecules which are larger than 40 kDa, tend to accumulate and retain in the tumor [56]. While utilizing the EPR effect has proven to be an effective way in treating subcutaneous mouse models, many of the nano delivery vehicles which have entered human clinical trials have been ineffective [57, 58]. The discrepancy in treatment efficacy in murine cancer models to human cancers is largely believed to be due to significant differences in tumor vasculature. The use of more advanced murine cancer models and diagnostic tools to identify human patients which the EPR effect is effective are solutions to this serious issue.

In addition to passive targeting, many drug delivery systems utilize active targeting to increase the delivery of drugs to the tumor. In many cancers, the cancer cells or local tumor environment overexpress various extracellular receptors which provide a target to bind to. Nano-sized delivery vehicles have been coated with small molecules, such as sugars, or

macromolecules, such as antibodies, aptamers, peptides, and oligonucleotides, which bind to the overexpressed receptors with great selectivity [50]. Most notably, antibody drug conjugates (ADC), which consist of a monoclonal antibody conjugated to a cytotoxic drug, have been evaluated in the clinic over the past few decades, with a few recent products improving treatment efficacy over standard care [59]. Unfortunately, many of the targeted therapies are still limited by off-site toxicity. In addition, a recent review on nanoparticle delivery has shown that active targeting mechanisms only improved the average delivery of nanoparticles to murine, solid tumors from 0.6 % to 0.9 % of the injected nanoparticle dose [57].

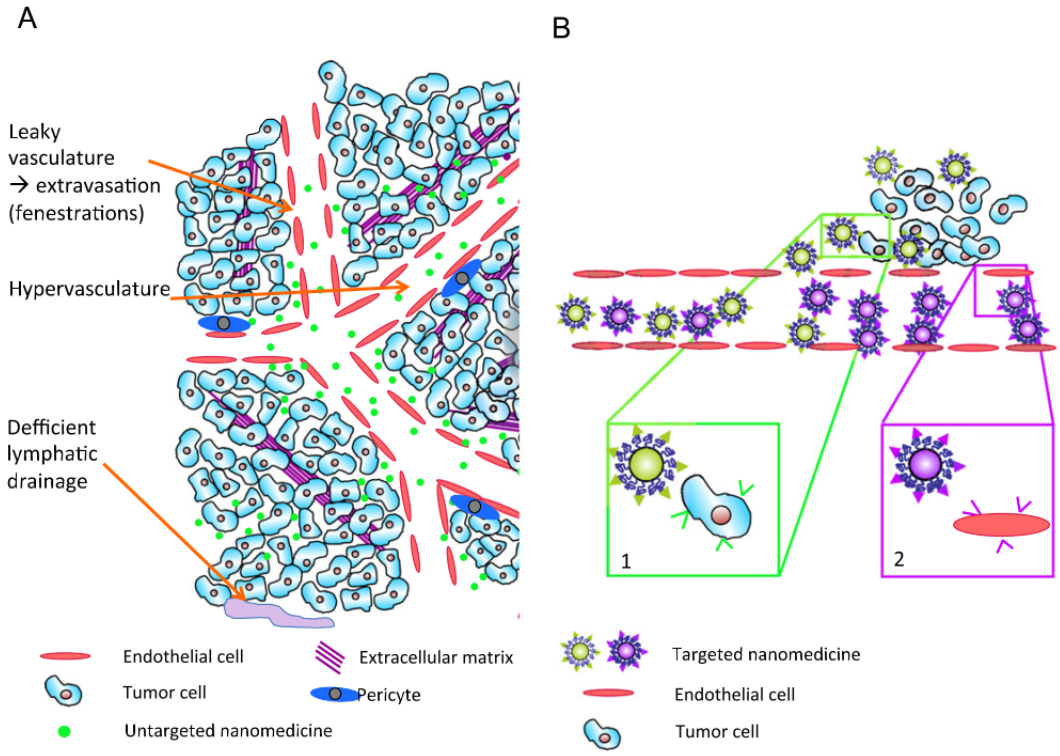

Figure 2.3: (A) Cartoon schematic demonstrating nanoparticle delivery to solid tumors utilizing the EPR effect. (B) Active targeting of nanoparticles to tumor cells (1) or to tumor vasculature (2). Reprinted from [58], with permission from Elsevier.

Regardless of how the delivery vehicle reaches the tumor site, the therapeutic payload needs to be released to be effective. Most systems which have been evaluated in the clinic release

drugs through passive mechanisms, such as the degradation of the delivery vehicle or hydrolysis of chemical bonds. Many vehicle designs take advantage of the tumor microenvironment, consisting of a slightly acidic pH, abundance of specific enzymes, and hypoxic conditions, to release drugs more quickly at the tumor site. More recently, there has been significant effort in designing systems which release their payloads when triggered externally, typically using light or ultrasound [50, 60].

After the initial approval of Doxil® 20 years ago, there has been a significant amount of research devoted to developing new nanomedicines and optimizing the biodistribution and drug release of these vehicles. Unfortunately, many of the deliver systems which initially showed promise in preclinical trials, were ineffective in clinical trial for reasons just discussed. More recently, various nanomedicines have started to perform well in clinical trials, and there are currently over 12 products approved for cancer treatment [61]. For example, liposomes, antibody drug conjugates (such as Kadcyla), and polymeric nanoparticles (such as Abraxane) have all been approved for various malignancies. From the accumulation of clinical trials, it is clear that using delivery systems can drastically alter the biodistribution of chemotherapeutics leading to less systemic toxicity, and more research is currently underway to continue to unleash the full therapeutic potential of nanomedicine. One area of research which is sparking a lot of interest is using delivery systems to deliver multiple therapeutics, which will now be discussed.

2.4.2 Use of delivery vehicles to deliver multiple chemotherapy drugs

Many drug pairs which are identified as effective (and often synergistic) in pre-clinical studies will be ineffective in the clinic. The failure in translation can be attributed to many variables, such as the inability to deliver both drugs simultaneously to the tumor site. Chemotherapy drugs have vastly different chemical and physical properties, and, therefore, are cleared through different pathways with different pharmacokinetics. It is generally believed that if

both drugs can circulate together, translation of drug combination from *in vitro* assays to the clinic can be significantly improved. Therefore, many nano-scaled delivery systems have been designed to carry combinations of chemotherapeutic agents directly to the tumor site (Fig. 2.4).

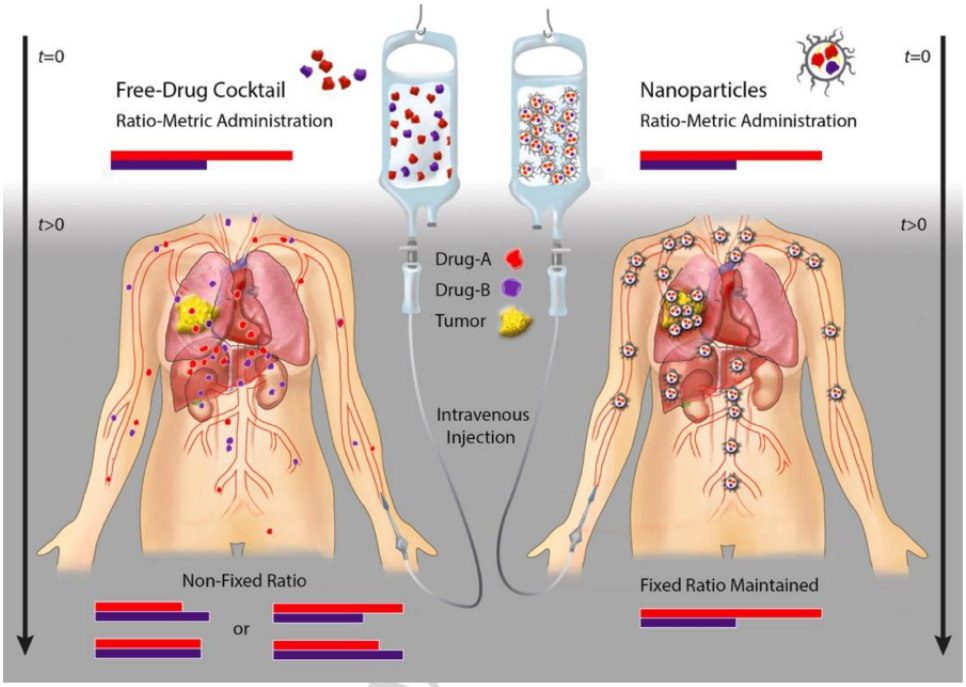

Figure 2.4: Cartoon demonstrating how nanoparticles can be used to deliver combinations of chemotherapeutic agents together throughout the body. Reprinted from [62], with permission from Elsevier.

In an attempt to increase the overall efficacy and reduce toxicity, drug delivery systems (DDS) carrying various combinations of chemotherapeutic agents have been engineered and tested [63, 62]. Liposomes, polymeric nanoparticles, inorganic nanoparticles, polymeric micelles, and polymer drug conjugates (PDCs) designed to carry combinations of chemotherapy agents have shown better efficacy in preclinical models compared to free drug combinations. Furthermore, VYXEOS (CPX-351), a liposomal formulation carrying daunorubicin and cytarabine, significantly extended patient survival over the standard care in a phase III clinical trial while treating secondary acute myeloid leukemia (AML).

When considering drug delivery in combination therapy, the ability to deliver a combination

of drugs at specific ratios is only half of the challenge because most synergistic drug pairs exhibit schedule dependent synergy. Typically, drug pairs are identified as synergistic when given concurrently; however, many drug pairs need to be sequenced correctly to exhibit synergy as discussed in a previous section. Many nanocarriers have been designed to deliver specific ratios of multiple drugs or to deliver drugs at specified times; however, the ability to control both these features in the same vehicle offer a significant synthetic and design challenge [64].

A few nano-sized delivery vehicles have been synthesized which control the relative release rate of multiple therapeutics by incorporating each drug into distinct regions in the particle. For example, particle systems which incorporate one drug into an outer particle shell and another drug into the particle core, can release the drugs at distinctly, different rates. Multiple studies have used this core-shell design methodology to release drugs with different release kinetics to improve the efficacy of a given drug pair [65, 66, 67, 68, 69]. While these studies demonstrate the potential benefits of using core-shell particles to stagger the release of multiple drugs, the particle design requires drastically changing particle structure to change release kinetics. In addition, the loading and release of each drug is dependent upon the physical properties of the drug, limiting the possible release profiles for any given particle design. More research into the development of combination delivery vehicles which control release rates with external stimuli or chemical linkers will help develop particle systems with more control over relative release kinetics.

2.5 Polymer drug conjugates

Of all systems engineered thus far to deliver chemotherapy agents, PDCs are unique and offer multiple advantages. Instead of physical encapsulation, drugs are chemically conjugated to a polymer, and the drug ratio and subsequent release rates are governed by the chemistry used to incorporate the drugs. While only a few combination PDCs have entered the clinic,

the success of single agent PDCs in clinical trials, most notably the ability to decrease toxicity, give rise to further motivation in continuing the development of PDC-based combination chemotherapy [70, 71, 72, 73, 74, 75].

2.5.1 Single drug polymer drug conjugates in clinical trials

Helmut Ringsdorf first proposed the idea of linking drugs to a polymeric carrier via a covalent bond in 1975 [76]. Since then, a variety of polymeric-based drug delivery systems have been engineered to deliver therapeutic agents and studied extensively in vivo [77, 78, 79, 80, 81, 82]. When compared to traditional small molecule therapeutics, polymer-drug conjugates (PDCs) can improve the drugs solubility in water, protect it from systemic degradation, and increase drug circulation time. This increases the drugs bioavailability at the desired site of action, thereby reducing the dose required to elicit the desired outcome.

A wide range of natural and synthetic water-soluble polymers, which are biocompatible, have been synthesized to deliver drugs. While each polymer drug system has its own physical characteristics, a few general trends have been observed in the field. For example, studies have shown that polymers with a higher molecular weight tend to circulate longer in the plasma due to reduced renal clearance rates, and can accumulate higher at the tumor [83, 84]. On the contrary, polymer architecture and structure has shown minimal effect on tumor extravasation [85]. The polymer drug conjugates which have been evaluated in the clinic are now discussed and summarized in Table 2.2.

HPMA copolymer-drug conjugates

Although a synthetic polymer, N-(2-hydroxypropyl) methacrylamide (HPMA) copolymer is the most versatile and greatly explored polymer used in PDCs. HPMA is highly soluble in water, nontoxic, non-immunogenic, and capable of circulating in the blood for extended

periods due to non-adsorption of plasma proteins [86]. The HPMA copolymer is generally synthesized via free radical polymerization of co-monomers HPMA and methacrylated (MA)-peptidyl-nitrophenylester (ONp). Although non-biodegradable, HPMA-drug conjugates with a molecular weight (MW) less than 40 kDA can be eliminated from the body via renal filtration. Further, multi-block degradable HPMA conjugates have been designed to allow for larger constructs to be administered systemically and still be cleared [87].

Various HPMA products have been evaluated in clinical trials, including conjugates carrying doxorubicin (DOX), paclitaxel (PTX), camptothecin (CPT), and DACHPt (oxaliplatin parent complex) [73, 75, 88, 89]. In all of the trials, 20 to 30 kDa HPMA copolymers were used with the peptide cleavable linker GFLG or acid labile linkers. In addition, a targeting ligand was also evaluated by conjugating both galactosamine and DOX to HPMA (PK2) [90]. The majority of the phase I and II clinical trials reported acceptable toxicity with partial responses during treatment of various cancers. All conjugates reported improved drug bioavailability and tolerable toxicity profiles, and the conjugate carrying DACHPt (ProLindac) has shown very promising clinical results. Phase I/II clinical evaluation of ProLindac in patients with recurrent ovarian cancer demonstrated an excellent safety profile and antitumor efficacy. Subsequently, a multicenter-based evaluation of ProLindac in combination with Paclitaxel (PTX) is being pursued in Europe for treatment of late stage ovarian cancer [91].

Polysaccharide-drug conjugates

Polysaccharide-based systems are highly attractive due to their biocompatibility, biodegradability, and relatively low synthesis costs. Polysaccharides are highly soluble in water and have various functional groups to conjugate drugs. Due to their ability to be degraded naturally, higher MW conjugates can be administered to enhance plasma retention times. In addition, certain polysaccharides are capable of specifically binding to cancer cells, such as hyaluronic acid (HA) which binds to CD44 (a cell surface receptor that is highly expressed on cancer

cells).

Polysaccharide-drug conjugates that have entered clinical trials were primarily based upon hyaluronic acid (HA), dextran (DEX), and cyclodextrin. Many of these conjugates, including AD-70 (oxDEX-DOX), DE-310 (cmDEX-exatecan), and MEN 4901/T-0128 (cmDEX-T-2513) showed excellent response rates, but severe toxicity limited the treatments [92, 93, 94]. A paclitaxel conjugate with HA administered with intravesical therapy showed excellent efficacy while treating bladder cancer locally [95]. In addition, a -Cyclodextrin-PEG copolymer with CPT (CRLX-101) is currently being evaluated for treating various types of cancers in phase 2 trials due to promising phase 1 results [72].

PEG-drug conjugates

Poly (ethylene glycol) (PEG) is an FDA approved commercial polymer widely used for biological applications. Due to its hydrophilic nature and reduced uptake by the reticuloendothelial system (RES), PEG can enhance the plasma half-life ($t_{1/2}$) and therapeutic index of drugs or proteins conjugated to its backbone. PEG conjugates with MW in the range of 20-50 kDa can avoid renal elimination, and nanoparticles formed from PEG with MW (2-5 kDa) circulate in the blood longer and avoid hepatic clearance [96]. In the clinic, drugs have been conjugated directly to the ends of single and multi-arm PEG and to block-copolymers containing PEG, which typically self-assemble into micelles.

PEG conjugates of CPT and active metabolites of CPT including Irinotecan (CPT-11) and SN38 were evaluated in clinical trials [97, 98, 99]. In PROTHECAN (PEG-CPT), CPT is conjugated to both ends of PEG with glycine spacers, while in EZN-2208 (PEG-SN38) and NKTR-102 (PEG-CPT-11), four drug molecules are conjugated to 4-arm PEG polymers. In all of the clinical studies, conjugation to PEG significantly increased drug bioavailability, and the PEG-drug constructs showed partial responses in the trials.

Various ampiphilic block copolymers of PEG-polypeptides were also tested in the clinical

setting. DOX (NK911) and epirubicin (EPI) (NC-6300) were conjugated to PEG-b-poly(aspartic acid) which self-assemble into 40 nm and 60 nm micelles, respectively [100, 101]. Similarly, SN38 was conjugated to PEG-b-poly(l-glutamic acid) with an ester bond, forming 20 nm micelles (NK012) [102]. In addition, the platinum drugs Cisplatin (CIS) and DACHPt were conjugated to PEG-b-poly(l-glutamic acid) with Pt coordination linkers (NC6004 and NC4016, respectively) forming micelles of approximately 30 nm [70, 103]. Having demonstrated good tolerability and acceptable efficacy in early clinical studies, NC6004 is now being tested in combination with gemcitabine (GEM) for the treatment of locally advanced or metastatic pancreatic cancer in a phase 3 study.

PG-drug Conjugates

Poly(α, L-glutamic acid) (PG) is a naturally occurring polypeptide composed of repeating units of L-glutamic acid. The polymer is highly soluble in water due to a negative charge that exists at neutral pH on the pendent free carboxyl group in each repeating unit of glutamic acid. PG is biocompatible and can undergo lysosomal degradation. It is primarily cleared via renal pathways with limited involvement of the reticuloendothelial system.

The poorly soluble drugs PTX and CPT have been conjugated to PG and evaluated in clinical trials, as XYOTAX and CT-2106, respectively [**?**, 104, 105]. PTX and CPT were conjugated to 39 kDa and 49 kDa PG, respectively, with an ester bond. Both drugs showed a significant increase in plasma half life upon conjugation with better tolerability than the single drugs.

2.5.2 Use of polymer drug conjugates in combination chemotherapy

Tumor cells often develop resistance to single drug therapy, minimizing treatment efficacy of polymer therapeutics carrying a single drug. To more effectively inhibit tumor growth,

Table 2.2: Single drug polymer drug conjugates evaluated in the clinic

Conjugate Name	Polymer-Drug	MW (kDa)	Clinical trials (cancer, phase)
HPMA-drug conjugates			
PK1 [11,13]	HPMA-DOX	30	Non small cell lung, breast cancers (Phase III)
PK2 [31]	HPMA-DOX-galactosamine	25	Hepatocellular carcinoma (Phase I/II)
PNU-166945 [29]	HPMA-PTX	25	Refractory solid tumors (Phase I)
PNU-166148 [30]	HPMA-CPT	18	Gastric and gastroesophageal tumors (Phase I)
AP-5346 [15]	HPMA-DACHPt	25	Ovarian cancer (Phase I/II)
Polysaccharide-drug conjugates			
ONCOFID-P-B [36]	HA-PTX	200	Bladder carcinoma refractory to BCG (Phase I)
AD-70 [33]	oxDEX-DOX	70	Various advanced cancers (Phase I)
DE-310 [34]	cmDEX-exatecan	360	Metastatic adenocarcinoma (Phase I)
MEN 4901/T-0128 [35]	cmDEX-T-2513	130	
CRLX101, IT-101 [12]	-Cyclodextrin-PEG-CPT	57	Advanced tumors (Phase I)
PEG-drug conjugates			
PROTHECAN [38]	PEG-CPT	40	Advanced solid malignancies (Phase I)
EZN-2208 [39]	PEG-SN38	40	Metastatic colorectal and breast cancers and pediatric cancer (Phase II)
NKTR-102 [40]	PEG-Irinotecan	20	Ovarian, breast, colorectal, and cervical (Phase II)
NK911 [41]	PEG-b-PASA-DOX	16	Metastatic pancreatic cancer (Phase II)
NC-6300 [42]	PEG-b-PASA-EPI	20	Advanced or metastatic solid tumors (Phase I)
NK012 [43]	PEG-b-PG-SN38	19	Small cell lung cancer (Phase II)
NC-6004 [10]	PEG-b-PG-CIS	26	Locally advanced or metastatic pancreatic cancer (Phase III)
NC-4016 [44]	PEG-b-PG-DACHPt	18	Advanced solid tumors or lymphoma (Phase I)
PG-drug conjugates			
XYOTAX, CT-2103 [45,47]	PG-PTX	39	Stage III or IV ovarian or primary peritoneal cancer (Phase II)
CT-2106 [46]	PG-CPT	49	Advanced solid malignancies (Phase I)

treatments can be designed to use PDCs to deliver a combination of chemotherapeutic agents. As originally discussed in the review by Greco *et al.* [106], there are many ways to incorporate PDCs into a combination chemotherapy platform. Most simply, two single drug PDCs can be administered simultaneously or at different time points. However, it may be advantageous for the drugs to circulate together, in which case a single delivery vehicle should be used. This vehicle can be a self-assembled structure of a single drug PDC with an adsorbed drug, a self-assembled structure of multiple single drug PDCs, or a polymer with multiple drugs conjugated to the same polymer backbone. Examples of these differences are shown schematically in Fig. 2.5.

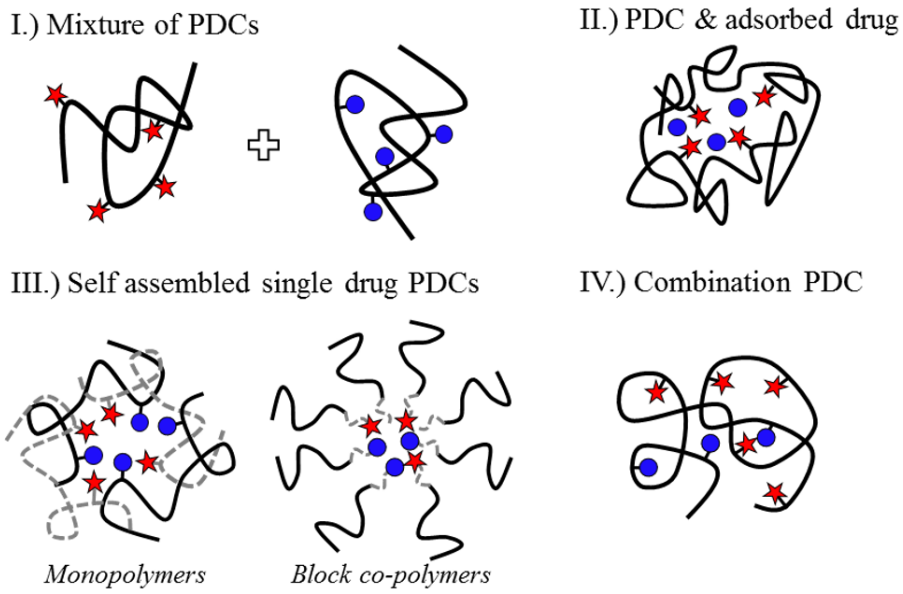

Figure 2.5: Cartoon schematic of the physical structure of polymer drug conjugates (PDCs) used to deliver combinations of chemotherapeutic agents.

Combination of drug pairs

Many PDC systems have been designed to deliver combinations of synergistic chemotherapeutic agents for various cancers. Block copolymers of PEG, which all self assemble into

micelles, have delivered DACHPt/EPI [107], CIS/DOX [108], CIS/PTX [109], and CPT/DOX [110] for treating advanced gastric cancer, hepatocellular carcinoma, cervical cancer, and breast cancer, respectively. The polysaccharides HA [111] and dextran [112] have also co-delivered CPT/DOX and HA has co-delivered CIS/DOX [113] for treatment of breast cancer. PG [114] and a pegylated polyglycerol dendrimer [115] have carried PTX/DOX for treatment of breast cancer. HPMA has also been used to deliver DOX/GEM [116] and DOX/DTX [117] for treatment of prostate and lymphoma, respectively.

The majority of these combination PDC systems demonstrate less toxicity and improved tumor growth inhibition compared to delivering the free drug combinations *in vivo*. Of the studies which report biodistribution, significantly more of each drug accumulates at the tumor site when delivered with a PDC compared to free drug administration. In addition, the combination conjugates show improved efficacy compared to control conjugates carrying single drugs, demonstrating the importance of using synergistic drug pairs.

In addition to delivering synergistic drug pairs, PDCs can often overcome the resistance typically associated with traditional chemotherapy. Drug resistance can be specific to a single drug, or to a large class of chemotherapeutics, often due to the over-expression of P-glycoprotein (P-gp) pumps which pump out small molecule drugs. Conjugation to a polymer can eliminate drug efflux from P-gp pumps, resulting in improved efficacy in many drug resistant cells.

Sensitivity to a specific drug can also be restored by delivering another drug simultaneously with the PDC which re-sensitizes the cell. Taxane-resistant prostate tumor cells have been effectively treated with an HPMA conjugate carrying DTX with cyclopamine [118] and PEG block copolymers carrying PTX with cyclopamine [119]. DOX resistant cancer cells have been treated with a xyloglucan conjugate carrying DOX and mitomycin C [120], an HPMA conjugate delivering DOX with P-gp inhibitors [121], and a polystyrene block copolymer carrying DOX and the P-gp inhibitor disulfiram [122].

Polymer carriers can also carry therapeutics which improve tumor targeting. The clinical product PK2 (HPMA-DOX-galactosamine), used galactosamine to specifically target the PDC to liver cells. Similarly, alendronate has been combined with PTX to target bone metastases in breast cancer using both an HPMA conjugate [123, 124] and a PEG dendrimer construct [125, 126]. In addition, chemotherapeutic agents can be combined with anti-vasculature drugs to simultaneously inhibit cancer cell growth and prevent the tumor from getting nutrients. For example, Wang *et al.* demonstrated the usefulness of forming a combination PDC which targets the tumor vasculature along with the tumor cells by using a PEG block copolymer to co-deliver PTX with Combretastin A4 [81]. There are also many examples of PDCs which deliver a nucleic acid, protein, or peptide with a small molecule drug to improve cancer cell sensitivity or carrier targeting [127, 128].

Physical combination compared to dual construct

For each PDC system, a critical parameter to address is whether or not it is satisfactory to physically mix together single drug PDCs, or if further therapeutic benefits can be obtained by incorporating multiple therapeutics into the same delivery vehicle. While a combined vehicle ensures that both drugs distribute similarly in the body, physically combining single drug PDCs allows for more flexibility in changing the drug ratio and schedule of administration of each drug.

Many studies have shown that using a combination conjugate is more effective than the physical mixture of single drug PDCs because both drugs are delivered simultaneously to the tumor site. For example, Makovsky *et al.* clearly demonstrated the improved therapeutic benefits of the dual construct PG-PTX-DOX compared to the physical mixture of PG-PTX and PG-DOX [114]. Furthermore, other studies have demonstrated the importance of controlling drug ratio on polymer backbone to maximize synergy and minimize administration dose, using the Chou-Talalay method [108, 111, 112, 23]. Interestingly, the optimal drug ratio can change

upon conjugation to a polymeric carrier due to new drug availability kinetics. For example, Camacho *et al.* have shown that the internalization of CPT and DOX is drastically different after conjugation to HA, leading to differences in sub-cellular concentrations of each drug [111].

On the contrary, a significant benefit of physically mixing together single drug PDCs is the ability to simply optimize the administration sequence of the carriers. For example, Zhang *et al.* demonstrated that giving an HPMA conjugate carrying GEM prior to an HPMA conjugate carrying PTX was more effective than other administration sequences [129]. Similarly, another report demonstrated that giving an HPMA-GEM conjugate prior to an HPMA-DACHPt conjugate was more effective than other schedules at inhibiting ovarian cancer cell growth *in vitro* [130].

Vehicle structure

While there are a plethora of studies which show the benefits of using a polymeric carrier to deliver a combination of drugs compared to free drug administration, few studies compare how effective the particular carrier is to other possible carriers. Variables such as vehicle structure (size, drug loading, etc.) and polymer properties (molecular weight, architecture, etc.) will play a role in affecting the performance *in vivo*. A few studies have explored how the physical architecture of a PDC with multiple drugs affects its efficacy *in vitro* and *in vivo*.

In one study, two combination PDCs, both carrying DOX and PTX were compared [115]. A dendritic conjugate (PGlycerol-PTX-DOX-PEG) was similar in efficacy to the physical combination of PGlycerol-PTX-PEG and PGlycerol-DOX-PEG, while the linear conjugate (PG-PTX-DOX) was much more effective than the physical combination of PG-PTX and PG-DOX. The authors hypothesize that the individual linear PDCs have different pharmacokinetic profiles, while the individual dendritic PDCs distribute similarly allowing for both drugs to reach the tumor site at the same time as with the combination conjugate.

In another report, two HPMA conjugates carrying DOX and DTX with different architectures were directly compared [117]. DOX and DTX were conjugated to both linear HPMA ($\sim$25 kDa) and degradable, dendritic HPMA ($\sim$250 kDa) with a hydrazone bond and levulinate linker, respectively. In a subcutaneous tumor model, both linear P-DOX and dendritic P-DOX were extremely effective at inhibiting tumor growth. Interestingly, the physical combination of linear PDCs was slightly more effective than linear P-DOX, but the physical combination of dendritic PDCs was significantly less effective than dendritic P-DOX. Less dendritic P-DOX accumulates at the tumor site when administered with dendritic P-DTX, giving insight into the additive behavior between the dendritic PDCs in vivo. The authors hypothesize that the normalization of the blood vessels at the tumor site after DTX exposure, makes it more difficult for dendritic P-DOX (as opposed to linear P-DOX which is smaller) to accumulate at the tumor site with the EPR effect. This study clearly demonstrates that the interactions between drugs is not just limited to tumor cell toxicity but also to tumor accumulation.

Chapter 3

Experimental methods

3.1 *In vitro* cell assays

All cell lines were cultured in a humidified incubator maintained at 37 °C and 5% CO_2. MDA-MB-231 and 4T1 cells were cultured in RPMI-1640 media supplemented with 10 % FBS and 0.5 % Pen Strep. BT-474 cells were cultured in Hybricare media supplemented with 10 % FBS and 1 % Pen Strep. MCF-10a cells were cultured in MEBM media supplemented with hydrocortisone, hEGF, insulin, BPBPE, 100 ng/mL cholera toxin, and 1 % Pen Strep.

3.1.1 Toxicity

The toxicity of all drug formulations was measured with the MTT assay. Cells (5 x 10^3 MDA-MB-231, 5 x 10^2 4T1, 1 x 10^4 BT-474, or 1 x 10^4 MCF-10a) were seeded in 100 μL of media into the wells of a 96 well plate and allowed to adhere overnight. Media was aspirated and replaced with drug formulations and cells were incubated with the drug solutions for 72 h (unless specified otherwise). If a shorter drug exposure, or delayed drug exposure was required, drug formulations were added and/or removed at the time points specified. After 72 h, all drug formulations were replaced with an MTT solution in media (0.5 mg/mL) and incubated for

3.5-4 h. The MTT solution was then aspirated and replaced with DMSO, and the plates were shaken for 30 min. Finally, cellular viability was measured by reading the absorbance of each well at 570 nm (Tecan Infinite M200 Pro).

Dose response curves were fit to each drug formulation with the median effect model [21]. For combination treatment, synergy was quantified with the combination index (CI), described in detail in an upcoming section. Error bars for the combination index were calculated by propagating the confidence intervals from the individual drug fits and the error in toxicity for the combination treatment. When calculating the combination index, single drug dose response curves were used with the identical schedule as given in the combination treatment.

3.1.2 Cell cycle analysis

Cell cycle distribution was determined after exposure to drug formulations with propidium iodide (PI). MDA-MB-231 or BT-474 cells were seeded into T25 flasks (7.5 mL; 1 x 10^5 cells/mL) and allowed to adhere overnight. Media was replaced with drug solutions, and cells were incubated with the drugs for 1 d, 2 d, or 3 d. At the endpoint, adherent and floating cells were collected with trypsin and centrifugation. Cells were washed 2x in PBS (5 mL) and then fixed by slowly adding 70 % ethanol (5 mL) with vortexing. Cells were maintained at 4 °C for at least 1 d and then washed again 2x with PBS (5 mL). The cells were then suspended into a PBS solution (500 μL) containing RNase A (100 μg/mL) and Tween 20 (0.01 vol. %). PI (5 μL) was added and the cells were gently vortexed and incubated in the dark at 25 °C for 30 min. After dye incubation, cells were placed on ice until analysis. Fluorescence of each cell was immediately quantified with flow cytometry using a Becton Dickinson FACSAria cell sorter (Franklin Lakes, NJ, USA) with a 633 nm laser with 660 PMT.

3.1.3 Apoptosis analysis

Apoptosis activity was determined by measuring Caspase 3 activity. Caspase 3 activity was determined using the EnzChek Caspase-3 assay kit. Briefly, cells were seeded into T25 flasks (7.5 mL; 1x10^5 cells/mL) and allowed to adhere overnight. Following incubation with drug formulations, floating cells and adherent cells were collected with trypsin and centrifugation. The cells were washed 1x in PBS, and then lysed in 75 μL of 1x lysis buffer for 30 min on ice. Lysed cells were then centrifuged at 5000 rpm for 5 min to remove cell debris, and the supernatant was collected. Caspase activity was quantified by mixing 50 μL of the supernatant with 50 μL of the 2x working solution containing the substrate Z-DEVD-AMC and incubated for 30 min. The fluorescence of each well was then measured with a Tecan Plate Reader (342/441 nm) for 30 min, and total caspase activity was calculated with respect to an AMC standard curve.

Caspase activity was then normalized to the total protein content, using the micro BCA assay (Thermo Scientific). Briefly, 15 μL of the leftover supernatant was diluted with 135 μL of DI water and incubated with 150 μL of the BCA solution for 1.5 h at 37 °C. After incubation, protein content was determined by reading the absorbance at 562 nm (Tecan Plate Reader) with internal protein standards of bovine serum albumin (BSA).

3.1.4 Confocal internalization studies

To allow cells to adhere to glass, 8 well plates (cover glass thickness) were incubated with fibronectin (20 μg/mL) for 30 min at 25 °C. MDA-MB-231 cells (2.5 x 10^4 cells/well) were allowed to adhere overnight, and then cells were incubated with HA-DOX conjugates or DOX for 4 or 24 h. After incubation, cells were immediately washed with PBS 2x, and then the nuclei were stained for 15 min at 37 °C with Hoechst 33342 in live cell imaging buffer. After staining, cells were imaged live with confocal microscopy using a temperature

controlled stage (Olympus Fluoview 1000 Spectral Confocal). Hoechst and DOX were imaged using excitation/emissions of 350/461 and 480/570 nm, respectively.

3.2 Determination of synergy with combination index (CI)

In order to screen through drug pairs, a metric needs to be used to quantify the degree in which two or more drugs produce a synergistic effect without any knowledge of biological mechanism [22]. Over ten different analysis methods have been proposed to quantify synergy [20]. The most encompassing technique used is the calculation of a combination index (CI), which also involves using the median effect model to describe the toxicity induced from a single drug. The technique, developed by Chou and Talalay, is consistent with many previous methods including the isobologram method from Frazer, the idea of Loewe additivity, Bliss independence, and the interaction index method developed by Berenbaum [131, 132, 20, 22].

Assuming two drugs are mutually exclusive, the median effect analysis says that the dose response to a drug combination should be a summation of the response to each of the individual drugs:

$$\left[\frac{(f_a)_{1,2}}{(f_u)_{1,2}}\right]^m = \left[\frac{(f_a)_1}{(f_u)_1}\right]^m + \left[\frac{(f_a)_2}{(f_u)_2}\right]^m = \frac{(D)_1}{(D_{med})_1} + \frac{(D)_2}{(D_{med})_2}$$

where m indicates the order, $(D)_i$ the dose given of drug *i*, and $(D_{med})_i$ the dose of drug i required to produce a median effect [21]. Any interactions between the two drugs, whether synergistic or antagonistic, will produce a fraction affected that is not consistent with this analysis. The combination index is an adaptation of this equation and is used to quantify the degree in which the two drugs interact with each other. Using the previous equation as a basis, the combination index, for any number of drugs, is defined as:

$$CI = \sum_i \frac{(D)_i}{(D_x)_i}$$

where i indicates each drug used in the study, D_x represents the dose required to produce the specific fraction affected with the median effect analysis, and D represents the actual dose given in the combination study. A CI > 1 indicates an antagonistic interaction, a CI = 1 indicates an additive effect, and a CI < 1 indicates a synergistic effect. Typically, a CI < 0.8 is required for two drugs to exhibit "moderate synergism" [21].

The previous analysis was developed to quantify synergy for the concurrent exposure of multiple drugs. It has been suggested that the analysis can also be used to quantify synergy when drugs are exposed sequentially, if a dose response curve is generated for each individual drug that matches the exposure time and schedule used in the combination scheduling study [21]. For example, if drug A is pulsed for 1 day and then drug B is pulsed for 1 day, the dose response curves for each drug must be generated for a 1 day pulse of drug A and a 1 day pulse of drug B with the 1 day initial time delay. This analysis has been used to show that specific combinations of cancer drugs exhibit schedule dependent synergy in various studies [43, 41, 45, 40]. However, whether or not this analysis is the optimal way to quantify schedule dependent synergism is unclear. It is important to consider the effect that individual drug schedules have on cellular response because this is inherently removed from the combination index, which is calculated using the relevant individual drug schedules.

3.3 Synthesis of polymer drug conjugates

3.3.1 Synthesis of amino acid GEM amide prodrugs

3, 5-O-Bis(tert-Butoxycarbonyl)gemcitabine (1)

The alcohols on GEM were protected with BOC groups similarly as reported previously [133]. Briefly, DBDC (3.63 g) dissolved into anhydrous dioxane (33 mL) was added dropwise to GEM-HCl (500 mg) dissolved in 1 M KOH (33 mL) over 20 min. Reaction progress was monitored via TLC (5:4:1 DCM:acetone:ethanol). After 40 min, the reaction was extracted 3x with ethyl acetate (70 mL) and then the oil was washed 2x with saturated brine (10 mL). Solvent was removed with rotary evaporation and the product was dissolved into dioxane (33 mL) with more DBDC (3.63 g). 1 M KOH (33 mL) was added to the flask and allowed to stir for 30 min. The crude product was isolated by repeating the same extraction steps in addition to drying over $MgSO_4$. Pure (1) was then obtained with SiO_2 chromatography using a 1:1 DCM:acetone mixture. Yield: 55-60 %,1H NMR (DMSO) δ 1.41 (s, 9H, BOC), 1.44 (s, 9H, BOC), 4.30-4.41 (m, 3H, 4 and 5), 5.23 (b, 1H, 3), 5.79 (d, 1H, 5), 6.20 (b, 1H, 1), 7.44 (s, 2H, NH2), 7.52 (d, 1H, 6).

4-glycl-gemcitabine (2)

Glycine was conjugated to the amine on GEM to form (2). Briefly, the carboxylic acid on BOC-glycine (45.4 mg) was activated with TBTU (83.1 mg) and DIPEA (67.7 L) in anhydrous DMF (2 mL) for 30 min. Product (1) (100 mg), dissolved into anhydrous DMF (2 mL) with DIPEA (37.5 L) was mixed with activated BOC-glycine and reacted for at least 30 min. After removing the DMF with rotary evaporation at 65 °C, the product was dissolved into ethyl acetate and washed with DI water, saturated $NaNHCO_3$, and saturated brine. The crude product was then dried over $MgSO_4$ and then isolated with SiO_2 chromatography (20:1

ethyl acetate:hexanes). The BOC groups were then deprotected in a 1:1 TFA:DCM mixture and the solvents were removed with rotary evaporation. Yield: 60-65 %, 1H NMR (DMSO) δ 3.62-3.66 (q, 1H, 5), 3.76-3.83 (m, 1H, 5), 3.86-3.92 (m, 3H, 4 + glycine side), 4.17 (m, 1H, 3), 6.16 (m, 1H, 1), 7.10 (d, 1H, 5), 8.15 (b, 3H, NH3), 8.30 (d, 1H, 6), 11.42 (b, 1H, NH).

4-L-valyl-gemcitabine (3)

Valine was conjugated to GEM to form (3) identically to how (2) was synthesized. Yield: 50-55 %, 1H NMR (DMSO) δ 0.91-0.97 (dd, 6H, valine methyl), 1.96 (s, 1H, valine), 3.62-64 (q, 1H, 5), 3.77-3.82 (m, 1H, 5), 3.85-3.91 (m, 2H, 4 + valine side), 4.16 (m, 1H, 3), 6.16 (m, 1H, 1), 7.22 (d, 1H, 5), 8.33 (d, 1H, 6), 11.4 (b, 1H, NH).

3.3.2 Synthesis of HA polymer drug conjugates

DOX-HA amide, GEM-gly-HA, and GEM-val-HA were all synthesized using a similar procedure. Briefly, sodium hyaluronate (50 kDa, 7.5 mg/mL) was dissolved in 1:1 deionized water:DMSO. Sulfo-NHS (20-40 mol % relative to dissacharide repeat unit) was dissolved into DI Water and EDC-HCl (20-40 mol %) was dissolved into DMSO, and both solutions were added to the HA solution. DOX-HCl (10-40 mol %) or the GEM prodrug (10-40 mol %) was dissolved into DMSO and added to the reaction. The reaction proceeded overnight at room temperature, and the polymer drug conjugate was purified through repeated precipitation and washing steps in ethanol/PBS mixtures.

DOX-HA hydrazone was synthesized similar to previous reports [134, 135]. Briefly, HA (50 kDa, 10 mg/mL) and adipic acid dihydrazide (300 mol % relative to dissacharide repeat unit) were dissolved into DI water. The pH was then adjusted to 4.75 with 1 M HCl, and then EDC-HCl (20 mol %) was added to the solution. After reacting for 5 h, the polymer (HA-ADH) was precipitated and washed 2x in ethanol/PBS. HA-ADH was then dissolved into 1:1

DI water:DMSO (1.25 mg/mL) and DOX-HCl (10-20 mol %) was dissolved into DI water (2.5 mg/mL) and added quickly to HA-ADH while stirring vigorously. After reacting for 3 to 5 h, DOX-HA hydrazone was then isolated through repeated precipitation and washing steps in ethanol/PBS.

3.4 Characterization of delivery vehicles

3.4.1 Drug release kinetics

Release kinetics of drugs from delivery vehicles was determined through dialysis. Vehicles were dissolved into either PBS at pH 7.4 or pH 5 (adjusted with 1 M HCl). The vehicles were incubated in dialysis filters (Slide-A-Lyzer MINI Dialysis Device, 10K MWCO), with the same buffer below the filter. The bottom centrifuge was replaced with fresh buffer at each time point. Concentrations of drug in the tubes were determined by measuring the absorbance or drug with a TECAN plate reader.

3.4.2 Dynamic light scattering

HA conjugates were dissolved into PBS at concentrations ranging from 0.01 mg/mL to 0.10 mg/mL. The size of particles were determine using DLS on a Malvern ZetaSizer Nano ZS. Prior to analysis, conjugate samples were centrifuged at 500 rpm for 1-2 min. to remove large dust particles in the sample.

3.4.3 Transmission electron microscopy (TEM)

For Cryo TEM, conjugates were dissolved into PBS at a concentration of 1 mg/mL. Samples were then prepared for imaging using a Vitrobot Mark IV at room temperature and 100 % relative humidity. Prior to sample deposition, Lacey carbon coated copper grids (200 mesh)

were plasma-treated for 20 s. After the surface treatment, samples were deposited (1.2 μL) onto the grids and blotted once (time: 1 s, force: 2), and then immediately plunged into vitrifying liquid. The samples were then transferred to the cryo-TEM holder and viewed under the FEI Tecnai G2 Sphera TEM at 200 kV. Gatan Digital Micrograph was used to record the images acquired by the digital camera.

3.4.4 Nuclear magnetic resonance (NMR)

Synthesis steps were verified with ^{1}H NMR (Varian VNMRS, 600 MHz). Spectrums for small molecule drugs and prodrugs were measured in $(CD_3)_2SO$ with a relaxation period of 1 s and spectrums for HA conjugate were measured in D_2O with a relaxation period of 3 s.

3.4.5 UV-spectroscopy (UV-vis)

Drug loading of HA conjugates was measured with UV-vis spectroscopy (Tecan M220 Plate Reader). Conjugates were dissolved in PBS ($\sim$ 1 mg/mL) and the concentration of drug was determined using drug calibrations. The following molar absorption coefficients were used (for 100 μL of liquid) for Gem-amino acid prodrugs, GEM, and DOX, respectively: $\varepsilon_{250} = 3500\ \mathrm{M}^{-1}$, $\varepsilon_{270} = 2800\ \mathrm{M}^{-1}$, and $\varepsilon_{480} = 2670\ \mathrm{M}^{-1}$.

3.5 *In vivo* efficacy studies

All experiments were performed according to approved protocols by the Institutional Animal Care and Use Committee of the University of California, Santa Barbara.

3.5.1 MDA-MB-231 orthotopic tumor model

A MDA-MB-231 orthotopic mouse breast cancer model was used to evaluate the efficacy of DOX and GEM combination therapy in athymic, nude mice (Charles Rivers Laboratories). MDA-MB-231 cells (2.5 x 10^6 , 100 μL of 1:1 PBS:Matrigel) were injected subcutaneously into the inguinal mammary fat pad of 6-8 week old athymic, nude mice. Starting 11 d after tumor transplantation, when tumors reached 50 mm^3, mice were treated either once, or 4x on a weekly basis. Tumor growth inhibition was measured with a caliper using the following equation: $V = (L * W^2)/2$, where is the L is the longest dimension of the tumor and W is the shortest.

3.5.2 4T1 orthotopic tumor model

A 4T1 orthotopic mouse breast cancer model was used to evaluate the efficacy of the conjugates *in vivo* in BALB/c mice (Charles Rivers Laboratories). 4T1 cells (1 x 10^5 , 100 μL) were injected subcutaneously into the inguinal mammary fat pad of 6-8 week old BALB/c mice. Starting 4 days after tumor transplantation, mice were treated every 3rd or 5th day for a total of 4 injections. All drug formulations were prepared in sterile saline (0.9 wt/vol % NaCl) and injected intravenously through the tail vein or subcutaneously in a mammary fat pad. Tumor growth inhibition was again measured with a caliper using the following equation: $V = (L * W^2)/2$, where is the L is the longest dimension of the tumor and W is the shortest. Due to the aggressive growth of 4T1 tumors, some mice had to be euthanized prior to significant weight loss ($>$ 15% body weight) or large tumor sizes ($>$ 1500 mm^3) due to necrotic, tumor ulcers.

Chapter 4

Identifying schedule-dependent synergy in breast cancer

Breast cancer is the second most common type of cancer in females, representing 29% of female cancer cases and 14% of all female cancer related deaths [136]. Breast cancer mortality rates have decreased by 34% from 1990 to 2010 [137]; however, this is more commonly attributed to increase in early prognosis as opposed to vast improvements in treatment [138]. With an annual death rate of approximately 40,000 [136], breast cancer remains an active area of research.

In the clinic, the primary treatment for most breast cancer cases is the surgical removal of cancerous mass, which can entail breast-conserving surgeries such as a lumpectomy or a quadrentectomy or complete removal of the entire breast with a mastectomy. Depending on the size and location of the initial tumor, chemotherapy, hormonal, and/or targeted therapy will often be given post surgery, called adjuvant therapy, to kill any remaining cancer cells in order to prevent relapse. In addition, chemotherapy is often given prior to surgery, called neoadjuvant therapy, to help reduce the size of the tumor and allow for a smaller surgical operation. For severe cases which are initially inoperable due to their size, this step is necessary for surgical

operation [138]. For advanced cases of breast cancer, prognosis is often poor due to tumor cells not responding to treatment regimens. The lack of response is typically attributed to innate and/or adaptive drug resistant processes [138].

This chapter focuses on the *in vitro* identification of synergistic chemotherapy drug pairs for treating breast cancer cells. The main objective is to identify synergistic drug pairs which can be incorporated into a single delivery vehicle to treat a specific phenotype of breast cancer. A panel of FDA approved chemotherapy drugs are screened against two different breast cancer cell lines, with a focus on understanding how drug administration schedule impacts the ability for a drug pair to inhibit tumor growth. After identifying a drug pair which demonstrates schedule-dependent synergy, the drug pair is evaluated *in vivo* to see the *in vitro* synergy improves efficacy *in vivo*.

4.1 Cell lines and drug panel to probe for synergy

Treatment options for breast cancer depend upon the phenotype of the tumor mass, which is generally based on the expression levels of the estrogen receptor (ER), human epidermal growth factor receptor 2 (HER2), and progesterone receptor (PR). The different phenotypes of breast cancer are generally grouped into the following categories: Luminal A (ER^+, $HER2^-$,$PR^\pm$), Luminal B (ER^+, $HER2^+$,$PR^\pm$), Basal (ER^-, $HER2^-$,PR^-), Claudin-low (ER^-, $HER2^-$,PR^-), and HER2 type (ER^-, $HER2^+$,PR^-) [139, 140, 141]. Generally speaking, tumors which do not over-express ER, HER2, or PR, are also referred to as triple negative [142]. While chemotherapy is often used to treat all late stage breast cancer patients regardless of phenotype, a high fraction of Luminal B and triple negative tumors are treated with chemotherapy.

Luminal B tumors are extremely aggressive and often metastasize elsewhere in the body, and therefore require systemic chemotherapy in combination with targeted therapies to help prevent and slow down disease progression. Similarly, triple negative tumors do not over-

express any of the common receptors and are therefore unresponsive to many of the targeted therapies, and, thus, have to be treated systemically with chemotherapy. In this report, the BT-474 and MDA-MB-231 cells lines are used as representive cell lines for Luminal B and triple negative type breast cancers, respectively. The BT-474 cell line, which was isolated from a solid, invasive ductal breast carcinoma [143], has been established as a representative cell line for Luminal B tumors [140]. MDA-MB-231 is a metastatic cell line which was obtained with a pleural effusion from a patient with an intraductal carcinoma [144], and is commonly used as a model cell line for triple negative breast cancer [142].

With over 60 FDA approved drugs for breast cancer, clinicians have a large repertoire of small molecule therapeutics and targeting agents to utilize for treatment. Many of the drugs share similar structure and mechanisms, and most of the commonly used chemotherapeutic agents can be placed in the following functional categories:

1. Alkylating agents: Induce DNA damage
2. Antimetabolites: Interfere with metabolism of molecules
3. Anthracyline antibiotics: Interfere with DNA replication
4. Estrogen receptor antagonists: Interfere with cell cycle progression
5. Taxanes and epothilones: Inhibit mitosis

Based on the stage and phenotype of the breast cancer, various treatments are used containing one or a combination of these drugs. For preliminary studies examining the effect of drug scheduling on single agent efficacy and combination therapy, five representative drugs were used (Figure 4.1). Each drug is a commonly prescribed agent from its respective category, where doxorubicin (DOX) is an anthracyline antibiotic, paclitaxel (PTX) a taxane, ixabepilone (IXA) an epothilone, gemcitabine (GEM) an antimetabolite, and lapatinib (LAP) an estrogen

receptor antagonist. A brief overview of the clinical application of each drug is now presented along with the relevent cellular mechanisms of drug induced toxicity.

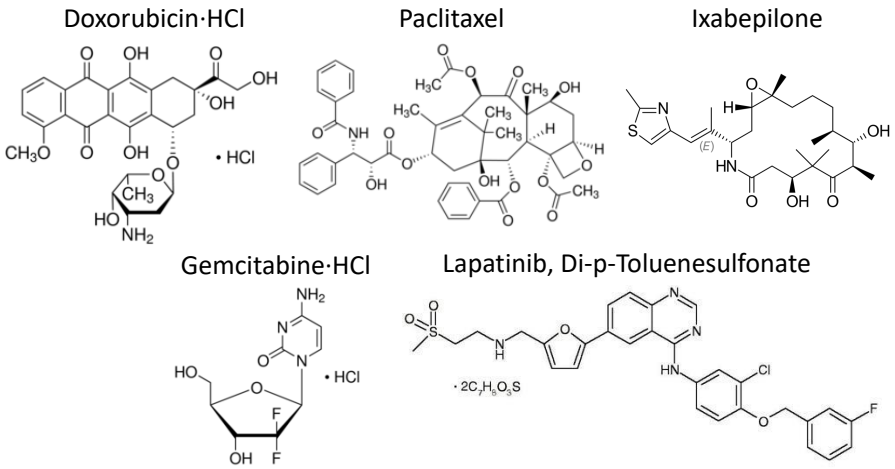

Figure 4.1: Small molecule therapeutics used for cell-drug studies

Doxorubicin (Adriamycin®) is a commonly used anthracyline antibiotic in breast cancer for adjuvant and neoadjuvant therapy. It is used both individually and in various combination therapies, including TAC (docetaxel, doxorubicin, and cyclophosphamide) [145, 146], AC $\rightarrow$ T (doxorubicin and cyclophosphamide followed by paclitaxel) [147, 148], and FAC (5-Fluorouracil, doxorubicin, and cyclophosphamide) [149]. Many mechanisms of drug induced toxicity have been observed *in vitro* including intercalation of drug into DNA, generation of free radicals, and inhibition of topoisomerase II, with the inhibition of topoisomerase II appearing to be the most plausible mechanism under *in vivo* conditions [150, 151].

Paclitaxel (Taxol®), one of the commonly prescribed taxanes, is used in various chemotherapy regimens. It is used in one of the commonly prescribed combination regimens (AC$\rightarrow$ T [147, 148]), and is also used to treat late stage, metastatic HER2+ cancer in combination with trastuzumab [152, 153]. Paclitaxel elicits cell death by binding along the length of microtubules and increasing stability, which both promotes microtubule polymerization and decreases de-

polymerization dynamics [154]. Apoptosis is then triggered by either preventing mitosis and triggering cell cycle arrest during the G2-M phase at high drug concentrations or through other, unclear mechanisms at lower drug concentrations [155].

Ixabepilone, an epothilone analog, was recently approved for the treatment of metastatic breast cancer. In particular, ixabepilone has shown potential in treating metastatic breast cancer patients which have become resistant to taxane therapy [156]. It has also shown activity in taxane resistant breast cancer patients when combined with capecitabine or trastuzumab [157, 158, 159]. Similar to taxanes, ixabepilone binds to microtubules, promoting growth and preventing mitosis. Interestingly, cells which overexpress P-gp and are resistant to paclitaxel, are still sensitive to ixabepilone [156].

Lapatinib (Tykerb®) is a small molecule antagonist of epidermal growth factor receptor (EGFR) and HER2. It has successfully been used in the clinic in combination with Capecitabine [160], an anti metabolite, for late stage HER2+ cancer. It also has shown promise as a potential solution to cells which have become resistant to trastuzumab, a more commonly used HER2 antagonist [161]. As opposed to trastuzumab, which binds to the extracellular portion of HER2, lapatinib binds to the intracellular ATP-binding domain of the receptor tyrosine kinase. All downstream activities of HER2 become blocked, which reduces cell growth and proliferation.

Gemcitabine (Gemzar®) is a pyrmidine antimetabolite which is the gold standard for treating pancreatic cancer. Gemcitabine has also shown promise in treating late stage breast cancer [162], and combinations with trastuzumab or paclitaxel have reported good response in patients already treated with chemotherapy in Phase II/III clinical trials [163, 164]. Gemcitabine inhibits tumor growth by being incorporated into DNA chains and inhibiting DNA synthesis [165].

4.2 Single drug toxicity screening

To identify synergistic drug pairs, the dose response of single drugs was first measured. BT-474 and MDA-MB-231 cells were exposed to each therapeutic agent for 72 h (Fig. 4.2). Cell viability was measured with the MTT assay at the end of drug exposure. To estimate the IC_{50} of each drug, cell viability was fit to the median effect model [21].

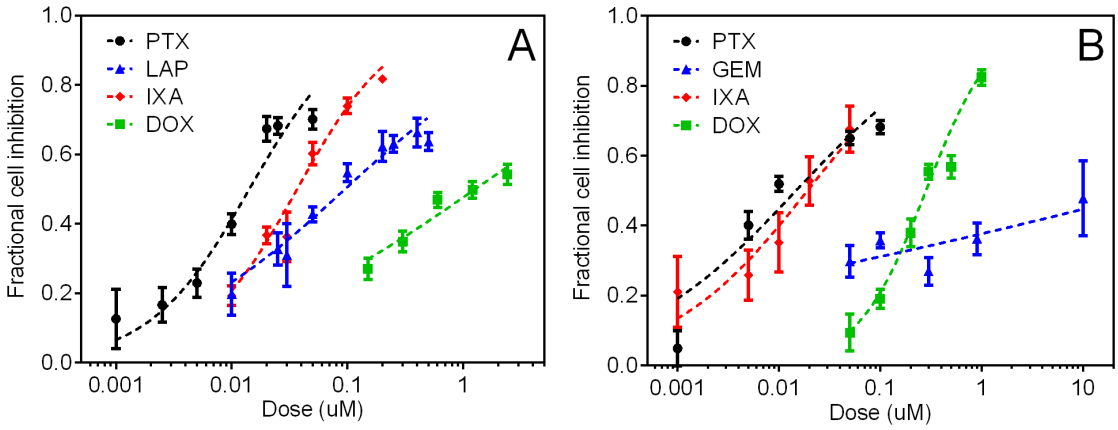

Figure 4.2: Growth inhibition of (a) BT-474 cells and (b) MDA-MB-231 cells after 72 h of single drug exposure. Markers represent experimental data and curves represent best fit median effect model. Error bars represent 95 % CI (n $\geq$ 12 wells).

Table 4.1: IC50 values

Drug	*BT-474 IC_{50} (μM)*	*MDA-MB-231 IC_{50} (μM)*
DOX	1.3 ± 0.2	0.28 ± 0.02
GEM	–	> 50
IXA	0.037 ± 0.002	0.019 ± 0.005
LAP	0.09 ± 0.01	–
PTX	0.014 ± 0.001	0.015 ± 0.003

After 72 h of drug exposure, BT-474 and MDA-MB 231 cells are both responsive to DOX, PTX, and IXA, with similar magnitude IC_{50} concentrations (Table 4.1). On the contrary, BT-474 cells are not responsive to GEM and MDA-MB-231 cells are not responsive to LAP. Con-

sidering that MDA-MB-231 cells are triple negative and do not over express HER2, it is not surprising that LAP does not have any toxic effect on the cell line.

4.3 Screening of drug synergy in BT-474 cells

After establishing the relative toxicity of each drug individually, drugs were tested in combination in attempt to identify synergistic drug pairs. First cells were exposed concurrently to a combination of drugs at single drug doses between the respective IC_{25} and IC_{50} concentrations. This concentration range was used to ensure that the drug dose was high enough to impact cell viability without killing all of the cancer cells. The drug pairs of DOX/LAP, IXA/LAP, and IXA/PTX are found to be synergistic, as the drug combinations inhibit BT-474 cell growth more than the individual drugs, resulting in CI values less than 1 (Fig. 4.3). It is possible the other drug pairs are also synergistic at different drug ratios; however, this was not explored further in this study.

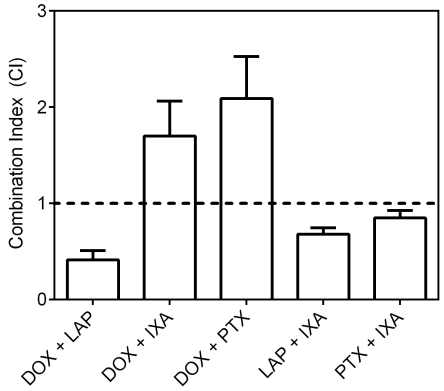

Figure 4.3: Synergy (expressed as CI) of combinations of LAP (0.025 μM), PTX (0.01 μM), IXA (0.03 μM), and DOX (0.6 μM) after 72 h, concurrent drug exposure on BT-474 cells. Error bars represent 95 % CI (n $\geq$ 12 wells)

BT-474 cells were then sequentially exposed to the same drug pairs, to determine if drug administration schedule impacts cellular proliferation (Fig. 4.4). For example, Drug A was

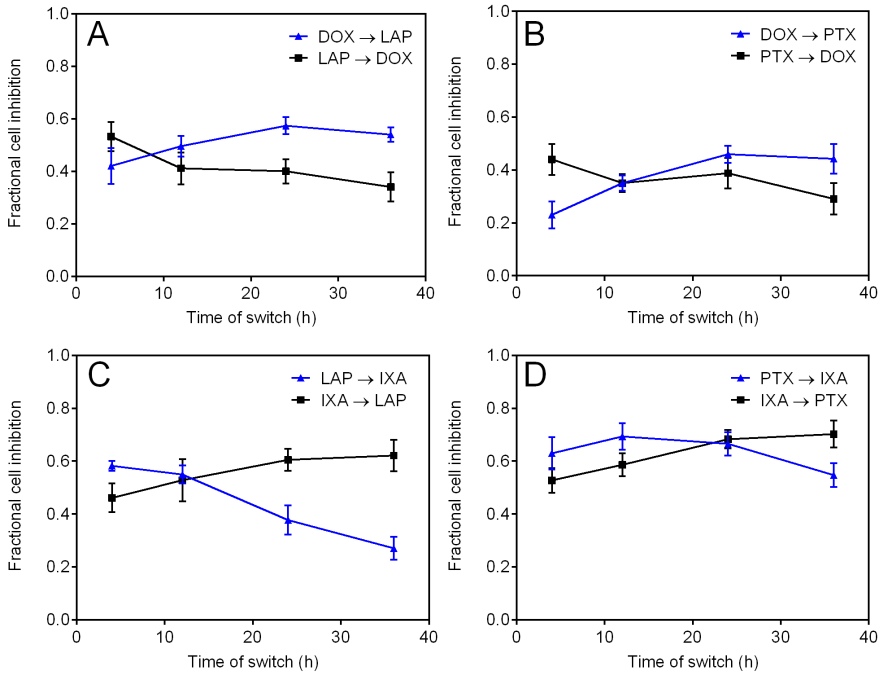

Figure 4.4: Fractional cell inhibition of BT-474 cells after the sequential exposure of (a) DOX (0.6 μM) and LAP (0.025 μM), (b) DOX (0.6 μM) and PTX (0.01 μM), (c) LAP (0.025 μM) and IXA (0.03 μM), and (d) PTX (0.01 μM) and IXA (0.03 μM). The first drug was aspirated and replaced with the second drug at the specified time points and cell viability was measured at 72 h. Error bars represent 95 % CI (n $\geq$ 12 wells).

given to the cells for 4, 12, 24, or 36 h and then replaced with Drug B for the remaining time in the 72 h drug exposure. Drug synergy (or CI) cannot be determined directly from these results because dose response curves were not found for each individual drug at the schedule given in the combination treatment. The effect of schedule on drug synergy will be determined for specific drug pairs in upcoming sections.

The schedule in which BT-474 cells are exposed to PTX and IXA has no impact on cellular viability; however, cell viability is significantly impacted by drug exposure schedule for all of the other drug pairs. The combinations of LAP/IXA and LAP/DOX, which are both synergistic when given concurrently, are most effective at inhibiting cell growth when LAP is given for 4 h prior to IXA or DOX or if LAP is given 24-36 h after IXA or DOX exposure. The combina-

tion of PTX and DOX, which is antagonistic when given concurrently, is more toxic with the following schedules than when given concurrently: PTX (4 h) $\rightarrow$ DOX (68 h) and DOX (36 h) $\rightarrow$ PTX 36 h.

It is clear that the schedule in which most chemotherapy drug pairs are exposed to BT-474 cells significantly impacts cellular toxicity. Because the combinations of LAP/DOX and LAP/IXA are synergistic when given concurrently and induce a different cellular response based on schedule, the effect of drug schedule on synergy should be explored further in future studies. Synergy may be enhanced if the drugs are sequenced more effectively. Based on these results, the effect of schedule on synergy is examined in detail for LAP and PTX, which has a similar mechanism of toxicity as IXA, in Chapter 6. LAP and PTX are incorporated into polymeric nanoparticles to take advantage of these synergistic interactions.

4.4 Screening of drug synergy in MDA-MB-231 cells

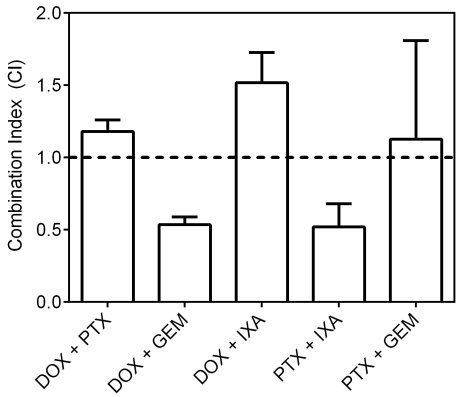

Figure 4.5: Synergy (expressed as CI) of combinations of GEM (0.2 μM), PTX (0.005 μM), IXA (0.015 μM), and DOX (0.3 μM) after 72 h, concurrent drug exposure on MDA-MB-231 cells. Error bars represent 95 % CI (n $\geq$ 12 wells)

MDA-MB-231 cells were also exposed to combinations of therapeutic agents for 72 h at single drug dose between the IC_{25} and IC_{50} concentrations (Fig. 4.5). Only the combinations

of GEM/DOX and IXA/PTX were synergistic at inhibiting tumor cell growth. Interestingly, the combination of IXA and PTX, which have similar mechanisms of toxicity, were also synergistic at inhibiting growth of BT-474 cells.

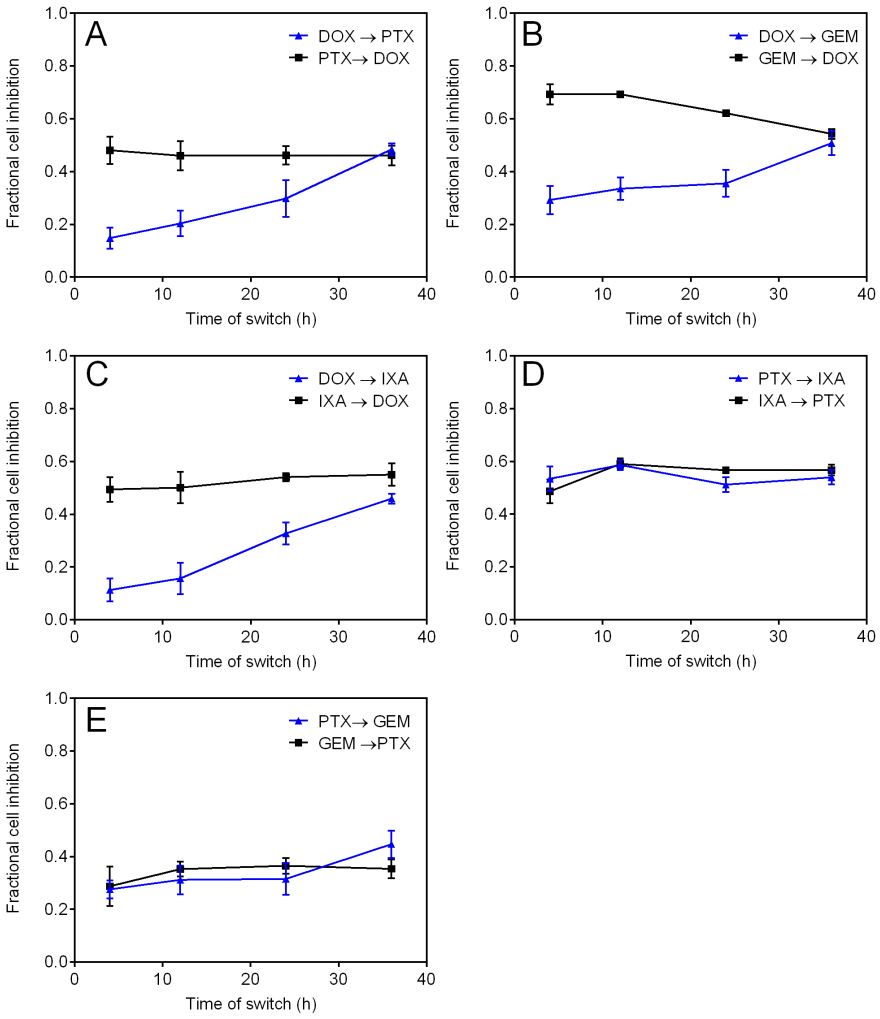

Figure 4.6: Fractional cell inhibition of MDA-MB-231 cells after the sequential exposure of (a) DOX (0.3 μM) and PTX (0.005 μM), (b) DOX (0.3 μM) and GEM (0.2 μM), (c) DOX (0.3 μM) and IXA (0.015 μM), (d) PTX (0.005 μM) and IXA (0.015 μM), and (e) PTX (0.005 μM) and GEM (0.2 μM). The first drug was aspirated and replaced with the second drug at the specified time points and cell viability was measured at 72 h. Error bars represent 95 % CI (n $\geq$ 12 wells).

Consistent with experiments done with BT-474 cells, MDA-MB-231 cells were then ex-

posed sequentially to each drug combination (Fig. 4.6). The combination of GEM and DOX, which is synergistic with a CI of 0.53 $\pm$ 0.05 when given concurrently, is significantly more toxic when cells are exposed to GEM prior to DOX. Furthermore the combinations of DOX with the two mitotic inhibitors (PTX and IXA) are more toxic when PTX or IXA is given prior to DOX. Consistent with BT-474 cells, the toxicity of PTX and IXA showed minimal schedule dependence on MDA-MB-231 cells. Due to the significant difference in cellular toxicity after exposure to different DOX and GEM schedules, the synergy of this drug pair is explored in the upcoming section.

4.5 DOX and GEM synergy *in vitro*

To examine the schedule dependence of synergy between DOX and GEM in more detail, dose response curves of each drug at different schedules were measured on MDA-MB-231 cells (Fig .4.7). The toxicity of each drug decreases as the cells are exposed to the drugs for a shorter time period. In addition, the time point of the initial drug exposure relative to the end point assay influences final cell viability.

Cells were exposed to different schedules of GEM and DOX over 72 h and viability was measured after treatment (Fig. 4.8). The dose selected to determine schedule-dependent synergy (0.3 μM) is approximately the IC_{50} of DOX and less than the IC_{50} of GEM. Simultaneous treatment with both drugs and incubation with GEM prior to DOX induced more toxicity than treatment with DOX prior to GEM. Incubating the cells with GEM 1 day prior to DOX (CI = 0.16 $\pm$ 0.03) is more synergistic compared to the pair's simultaneous treatment (CI = 0.76 $\pm$ 0.10). Furthermore, it is more synergistic if the cells are exposed to GEM prior to DOX compared to DOX prior to GEM, regardless if the first drug is removed (Fig. 4.8 a-c) or not (Fig. 4.8 d-f).

In addition to human, triple negative breast cancer cells (MDA-MB 231), the effect of

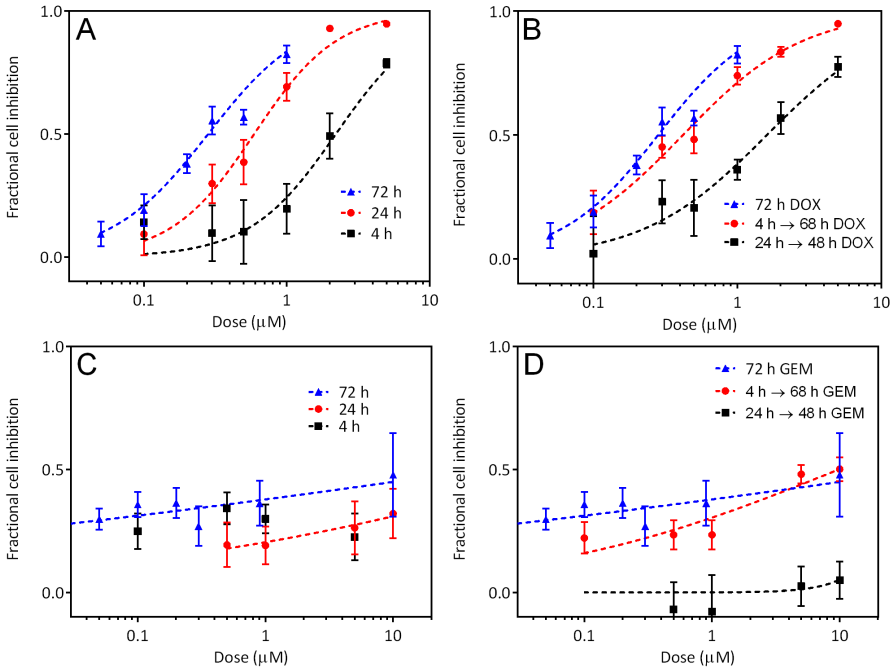

Figure 4.7: Fractional cell inhibition and relevant dose response curves for MDA-MB-231 cells after exposure to (a) DOX → media (b) media → DOX (c) GEM → media (d) media → GEM. Cell viability was assessed at 72 h for each schedule. Error bars represent 95 % CI (n ≥ 18 wells).

schedule on synergy was determined for non-cancerous, immortalized human breast epithelial cells (MCF-10a) and murine, triple negative breast cancer cells (4T1). The schedule of GEM (1 d) → DOX (2 d) is the most synergistic schedule for the MDA-MB-231 and 4T1 cells, while the schedule is the least synergistic for the MCF-10a cells (Fig. 4.9a). Scheduling GEM to DOX is extremely synergistic on the cancer cells (CI $<$ 0.2) across all dose ratios, while it is antagonistic on the non-cancerous cells for GEM:DOX ratios greater than 1 (Fig. 4.9b).

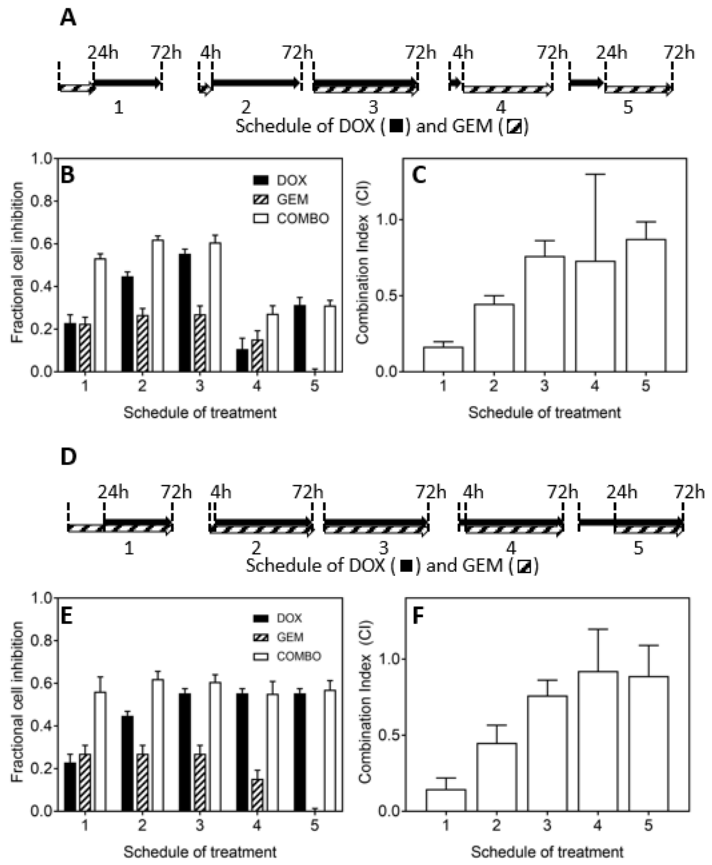

Figure 4.8: Effect of GEM and DOX schedule on synergy. (a) and (d) Schedules of DOX (0.3 μM) and GEM (0.3 μM) incubation on MDA-MB-231 cells. (b) and (e) Cell inhibition of GEM, DOX, and combinations at schedules specified in (a) and (d), respectively. Cell viability measured with the MTT assay. (c) and (f) Combination index of schedules of DOX and GEM calculated with the Chou-Talalay method. Data represent mean $\pm$ 95 % C.I. (n $\geq$ 12 wells).

4.6 Mechanistic studies of DOX and GEM

To further explore the effect of schedule with DOX and GEM on tumor growth inhibition, apoptosis activity was measured. Specifically, the amount of activated Caspase-3, which is the last executor caspase enzyme for both extrinsic and intrinsic apoptotic pathways, was measured after exposure to different drug schedules. Following 3 d of drug exposure, cells treated with GEM prior to DOX show more caspase activity than cells treated both with the drug pair

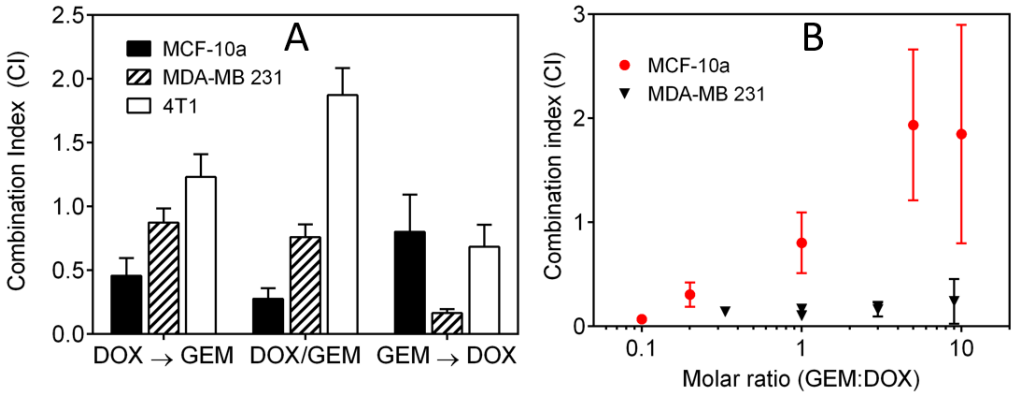

Figure 4.9: Effect of administration schedule on synergy for MCF-10a, MDA-MB-231, and 4T1 cells. GEM and DOX were given at an equimolar ratio near the IC_{50} dose at concentrations of 0.01 μM for MCF-10a and 4T1 cells and 0.30 μM for MDA-MB-231 cells. (b) Synergy for schedule of GEM (1d) $\rightarrow$ DOX (2d) with varying molar ratio of GEM:DOX. Data represent mean $\pm$ 95 % confidence intervals (n $\geq$ 6 wells).

simultaneously and with DOX prior to GEM (Fig. 4.10).

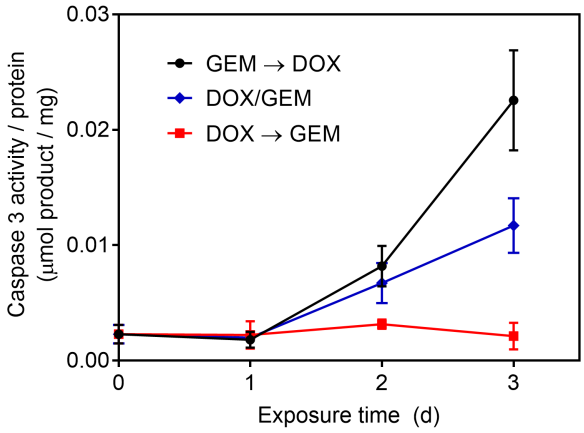

Figure 4.10: Effect of GEM and DOX schedule on initiation of apoptotic pathways measured with Caspase 3 activity normalized to total protein content. Data represents mean $\pm$ SEM (n=3).

GEM and DOX are known to be highly active in specific stages of the cell cycle. Therefore, to gain mechanistic insight on why GEM $\rightarrow$ DOX is more effective at inhibiting cancer cell growth than other schedules, cell cycle distribution after drug exposure was measured by

incubating cells with the nuclear stain P.I. (Fig. 4.11). Exposing MDA-MB-231 cells to GEM or DOX induces cell cycle arrest in the G0/G1 phases or G2/M phases, respectively. After exposure to GEM, the accumulation of cells into the G0/G1 phase is dose-dependent, with more cells accumulating in the S phase at lower GEM doses (Fig. 4.11c). Furthermore, after 1 d exposure to a high GEM dose (0.30 μM), cells remain locked in a similar cell cycle state for at least 2 d after drug exposure.

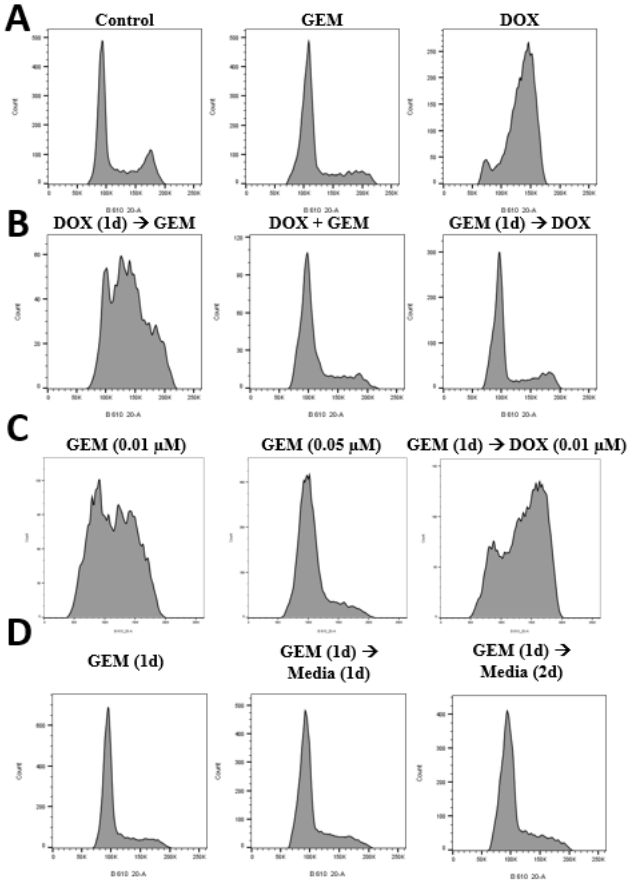

Figure 4.11: Cell cycle distribution of MDA-MB-231 cells after exposure to GEM, DOX, and GEM/DOX combinations measured with P.I. nuclear staining. (a) + (b) 72 h drug exposure (0.30 μM) (c) 72 h drug exposure at noted concentrations (d) 24 h of GEM (0.30 μM) exposure and a media washout

After incubation with GEM, MDA-MB-231 cells reach a similar cell cycle distribution after only 1 d of drug exposure. On the contrary, the cell cycle distribution continues to change

days after DOX exposure (Fig. 4.12). Exposing the cells simultaneously to GEM and DOX or exposing cells to GEM prior to DOX induces arrest in the G0/G1 phases, similar to exposing cells just to GEM. However, exposing cells to DOX prior to GEM induces arrest in the G2 and S phases.

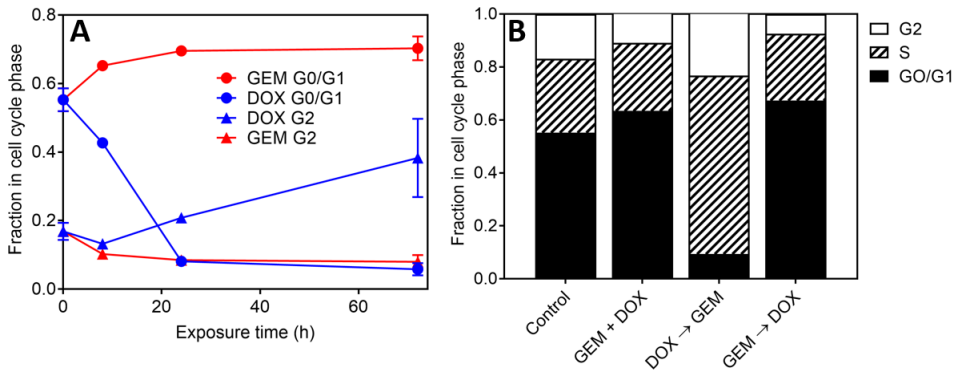

Figure 4.12: (a) Evolution of cell cycle distribution of MDA-MB 231 cells after exposure to DOX (0.3 μM) or GEM (0.3 μM) measured with flow cytometry using PI. (b) Cell cycle distribution of MDA-MB-231 cells after exposure to various schedules of DOX and GEM in combination (0.3 μM).

4.7 *In vivo* tumor studies with DOX and GEM

To determine if the *in vitro* synergy between free DOX and GEM translates to improved efficacy *in vivo*, a MDA-MB 231 orthotopic tumor model was used. In the first study, mice received one cycle of chemotherapy consisting of either DOX, GEM, DOX → GEM, or GEM → DOX. Using low doses of both DOX (2 mg/kg) and GEM (20 mg/kg), the schedule of GEM → DOX stopped tumor growth up to 20 d post treatment, which is significantly more effective than DOX or GEM on its own (Fig. 4.13a-b). The schedule of GEM → DOX (which was determined to be most effective *in vitro*) is only marginally more effective than the reverse schedule of DOX → GEM.

Next, 4 weekly injections of chemotherapy were given to attempt to eradicate the tumors.

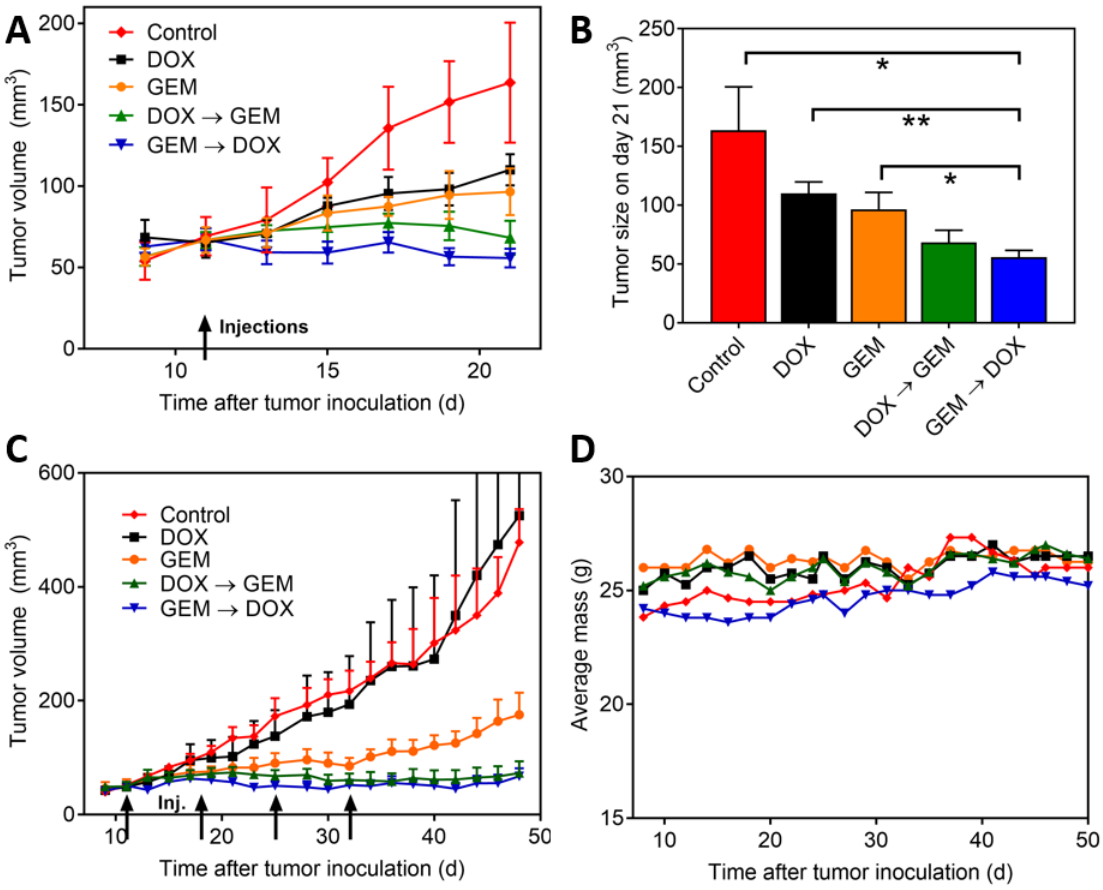

Figure 4.13: Tumor growth studies on MDA-MB-231 orthotopic xenografts in athymic, nude mice. All DOX (2 mg/kg) and GEM (20 mg/kg) doses are consistent for both studies and all experimental groups. The GEM → DOX and DOX → GEM groups have a 1 d delay between the injection of each drug. (a) Tumor growth inhibition with one i/v injection starting on day 11. (b) Final tumor volume for the study in (a). (c) Tumor growth inhibition with 4 x 1w i/v injections starting on day 11. (d) Average body masses throughout the course of injections shown in (c).

Again, the combinations of GEM → DOX and DOX → GEM are significantly more effective in inhibiting tumor growth than the individual drugs (Fig. 4.13c). Both schedules of DOX and GEM were able to stop tumor growth up to approximately 45 d; however, all the tumors eventually relapsed. It is important to note that the repeated injections of the low doses of GEM and DOX caused no observable toxicity as evident by no change in body weight throughout the course of the study (Fig. 4.13d).

4.8 Discussion of GEM and DOX synergy

Prior to engineering a combination vehicle with DOX and GEM, we wanted to fundamentally understand how the drugs interact while inhibiting tumor growth. The effect of drug administration schedule and drug ratio on synergy was studied to minimize drug dose required to inhibit cancer cell growth. Similar to previous reports, DOX and GEM are synergistic while inhibiting the growth of various cancer cell lines [166]. Interestingly, in both human (MDA-MB 231) and murine (4T1) triple negative breast cancer cells, the schedule in which the cells are exposed to the drugs has a larger impact on drug synergy than drug ratio. For both cell lines, it is more synergistic to expose the cells to GEM prior to DOX; furthermore, the CI is as low as 0.2 while giving GEM for 1d followed by DOX on MDA-MB-231 cells indicating that a 5x fold lower dose can be used. Interestingly, the schedule of GEM (1d) $\rightarrow$ DOX (2d) is not synergistic on immortalized, healthy breast epithelial cells (MCF-10a) if GEM is given in molar excess of DOX. This provides evidence that by manipulating the schedule and ratio in which you expose cells to DOX and GEM, it is possible to selectively induce more toxicity towards cancer cells (MDA-MB 231 and 4T1) compared to healthy cells (MCF-10a).

The increase in synergy upon giving GEM prior to DOX is consistent with an increase in caspase dependent apoptosis (Fig. 4.10). Exposing MDA-MB 231 cells to GEM (1d) $\rightarrow$ DOX (2d) compared to the simultaneous treatment with GEM and DOX for 3d leads to two times more caspase activity, even though the cells are exposed to each drug for less time. Previous reports have also shown that the schedule in which cancer cells are exposed to chemotherapeutic drugs can significantly impact the induction of pro-apoptotic pathways [32]. In addition, another study has shown that the pre-exposure of GEM increases the toxicity of topoisomerase inhibitors, such as DOX [167].

The strong dependence of tumor cell death on GEM and DOX administration schedule is likely related to the cell-cycle phase dependent mechanisms of both drugs. After exposure

to GEM, MDA-MB 231 cells accumulate in the G0/G1 and S phases of the cell cycle, while they accumulate in the G2 phase after exposure to DOX (Fig. 4.11 and 4.12), consistent with previous reports [168, 169, 165]. After exposure to combinations of both DOX and GEM, their cell cycle distribution closely matches that of the drug which the cells were exposed initially to. When exposing the cells to GEM and DOX simultaneously, the resulting cell cycle distribution is more similar to GEM, most likely due to the faster kinetics of cell cycle arrest after GEM exposure.

Both the toxicities of DOX and GEM have shown to be enhanced while treating cells in the early S phase of the cell cycle [170, 171]. Because DOX induces cell cycle arrest in the G2 phase, it is not surprising that giving GEM after DOX is the least toxic administration schedule. On the contrary, because GEM arrests cells in the G0/G1 and early S phases, the cells are sensitized to subsequent DOX treatment. From *in vitro* toxicity, it is difficult to identify an optimal pre-exposure time of GEM prior to DOX. Given that the cell cycle distribution remains the same after 1 d exposure of GEM this is not surprising (Fig. 4.12). In addition, because the cells remain in a locked cellular state for days after removing GEM, a longer delay between GEM and DOX exposure also seems satisfactory to induce the synergistic effect.

It is evident that combining GEM and DOX is effective at inhibiting MDA-MB-231 cell growth *in vitro*, and this was verified *in vivo*. In combination, low doses of DOX and GEM (2 mg/kg and 20 mg/kg, respectively) are effective at inhibiting tumor growth up to 50 d in an orthotopic, MDA-MB-231 tumor xenograft. In combination, the cumulative dose of both DOX and GEM is significantly lower than the single drug doses required to inhibit tumor growth in other human xenograft tumor studies [172, 173, 174, 175]. Surprisingly, the schedule of GEM $\rightarrow$ DOX is only marginally more effective at inhibiting tumor growth than the schedule of DOX $\rightarrow$ GEM (Fig. 4.13). While the schedule of DOX $\rightarrow$ GEM was still found to be synergistic *in vitro*, it is surprising that it was as effective *in vivo* as the reverse schedule even with a much higher combination index. Further research is required to understand why the optimal schedule

of GEM and DOX *in vitro* did not translate to *in vivo*. A possible explanation is the difference in cell behavior *in vivo* compared to *in vitro*.

4.9 Conclusions on drug synergy screening

By looking at cell viability after exposing MDA-MB-231 and BT-474 cells to different schedules of chemotherapy drugs *in vitro*, it is clear that drug schedule plays a critical role in the effectiveness of a drug pair compared to the single drugs. Sequentially exposing cells to one drug prior to another, can induce a cellular response which makes the cell much more susceptible to the toxic effects of the second drug. The drug pairs and schedules which were identified as synergistic here will not be synergistic for all patient tumors, stressing the importance of personalizing drug combinations for each individual patient. However, it is clear that both drug ratio and schedule can significantly impact how effective a given drug pair is at inhibiting tumor growth.

While *in vitro* studies provide a starting point for identifying effective drug combinations, many of the specific drug interactions may not be applicable to the *in vivo* environment. The drug combination of GEM and DOX was synergistic at inhibiting the growth of MDA-MB-231 cells *in vitro*. Furthermore, optimization of the drug pair showed that giving GEM prior to DOX enhanced this synergy *in vitro*. While the drug pair was significantly more effective at inhibiting MDA-MB-231 cell growth *in vivo* than the single drugs, the sequential administration schedules of giving GEM prior to DOX or DOX prior to GEM were equally effective *in vivo*. The optimization on drug schedule carried out with *in vitro* studies did not translate to the *in vivo* tumor model, motivating future drug combination optimization to be carried out in more realistic *in vitro* models and in *in vivo* studies.

Lastly, each chemotherapeutic agent distributes and circulates uniquely in the body, making it difficult to predict the exposure of each drug. This will not only impact the effectiveness of

the drug pair at inhibiting the growth of tumor cells, but also how the drug pair interacts with healthy tissue in the body. By incorporating a drug pair into a single delivery vehicle, drug ratio and release can be controlled throughout the body, taking advantage of optimal drug interactions.

Chapter 5

Engineering polymer drug conjugates to deliver GEM and DOX

GEM, an antimetabolite, and DOX, a topoisomerase II inhibitor, have been tested in various combinations in the clinic due to different mechanisms of dose limiting toxicity (neutropenia and cardiac toxicity, respectively) [176, 177, 178, 179, 180]. Similarly, the liposomal formulation of DOX (DOXIL) and GEM have been tested in combination [181]. However, in each of the clinical trials, moderate efficacy was reported over the individual agents, with more severe side effects reported in the majority of the trials, most notably neutropenia.

In attempt to improve the efficacy of combination treatment with GEM and DOX, various delivery vehicles have been designed to deliver DOX and GEM together, including HPMA polymer drug conjugates, silica nanoparticles, polymersomes, micellar nanoparticles, and hydrogel nanoparticles [116, 182, 183, 184, 166, 185]. The vehicles have been effective at treating various pancreatic, prostate, breast, and ovarian cancer lines *in vitro*, and the HPMA conjugate has shown efficacy *in vivo* in an AT1 prostate cancer model [116]. Although each of these studies demonstrate benefits by combining the drugs in a single carrier, further optimization of the interactions between DOX and GEM can enhance the efficacy of a combination delivery

vehicle carrying the two agents.

Here, we report on the development of a delivery vehicle to optimize the synergy between DOX and GEM. As discussed in Chapter 4, GEM and DOX synergy is schedule-dependent; therefore, polymer drug conjugates with hyaluronic acid (HA) are synthesized with different DOX and GEM release rates. The activity of the conjugates are evaluated on cancer cells *in vitro* and in an aggresive, orthotopic tumor model *in vivo*.

5.1 Hyaluronic Acid (HA) carriers

Hyaluronic acid (HA), a naturally occurring polysaccharide found in the extracellular matrix of various tissues, is a commonly used polymer in drug delivery [80, 186]. In the body, HA varies in molecular weight from a few kDa to 20 MDa and is directly involved in many biological processes including inflammation, wound repair, and morphogenesis. Due to the natural abundance of enzymes (hyaluronidases) which degrade HA, the polymer has an extremely short half life in the body making it biocompatible. In addition, HA is known to play a significant role in many cancers, as the natural receptor for HA (CD44) is often over-expressed by tumor cells.

Because HA is biocompatible, hydrophilic, and generally non-immunogenic, HA is commonly used in delivery systems for treating different cancers. Multiple studies have shown that coating a nanoparticle or liposome surface with HA can improve targeting of therapeutics to CD44 over-expressing tumors and increase drug circulation time [187, 188, 189, 190]. In addition, drugs can be conjugated directly to HA, forming HA-conjugates, to improve drug solubility and bioavailability [135, 191, 192, 134, 193]. Often times, HA-conjugates will self assemble into nanoparticles or micelles depending on the hydrophobicity of the conjugated drug.

There are multiple synthetic routes which drugs can be conjugated to HA, summarized in

a previous review [194]. Typically, drugs or pro-drugs are conjugated to the carboxylic acid or an alcohol on HA; however, other synthetic routes have also been utililized by manipulating another functional group on HA. In particular, many chemotherapeutic agents have been conjugated to the carboxylic acid of HA. PTX and GEM were conjugated with ester bonds [192, 195], GEM with an amide bond [193], and PTX with an ester bond using amino acids as chemical linkers [192]. DOX has been conjugated directly with an amide bond and with a hydrazone bond using adipic acid dihydrazide as a chemical linker [135, 134]. In addition, CIS has been been conjugated via Pt coordination with the carboxylic acid [191].

HA has been used to deliver chemotherapeutic agents through various administration routes. Due to the short half of HA in the plasma, many preliminary studies focused on localized therapy with HA-drug conjugates. HA-CIS and HA-DOX were effective at treating breast cancer xenografts with localized, subcutaneous injections [191, 134, 113]. After injection of the conjugates, no local inflammation was observed. In addition, HA-PTX, administered intravesically, was effective at treating bladder cancer that is resistant to the gold standard treatment (bacillus Calmette-Guerin) in a Phase I clinical study [95]. More recently, intravenous injections of HA-GEM were found to be effective at treating a subcutaneous, pancreatic cancer xenograft [193]. The conjugate, which protected GEM from degradation in the plasma, was effective at accumulating at the tumor site significantly higher than free GEM, giving motivation to continue exploring the intravenous administration of HA conjugates.

5.2 Synthesis of GEM prodrugs

To control the relative release rate of DOX and GEM, it was desirable to synthesize conjugates of GEM with different release kinetics. Previous reports have shown that amino acid (ester and amide) prodrugs of GEM hydrolyzed with different kinetics, depending on the size of the amino acid [196, 197]. Therefore, amino acid prodrugs of GEM were synthesized and

conjugated to HA to control GEM release, which is similar to previous work done with HA-PTX conjugates [192].

Based on the fast hydrolysis ($t_{1/2} = 11$ h) of a previously reported GEM prodrug, which was synthesized by conjugating the aromatic amine on GEM to a carboxylic acid [198], amino acids were conjugated to the amine on GEM to ensure fast releasing GEM prodrugs. To prevent the formation of GEM-amino acid esters, the alcohols on GEM were BOC protected as previously reported [133]. After protecting the alcohols on GEM, GEM was conjugated to the carboxylic acids on BOC protected glycine and valine to form prodrugs with different release kinetics (Fig. 5.1). After conjugation and purification, the BOC groups were deprotected with TFA. All chemical steps were monitored with NMR and chemical shifts are listed in Chapter 3.

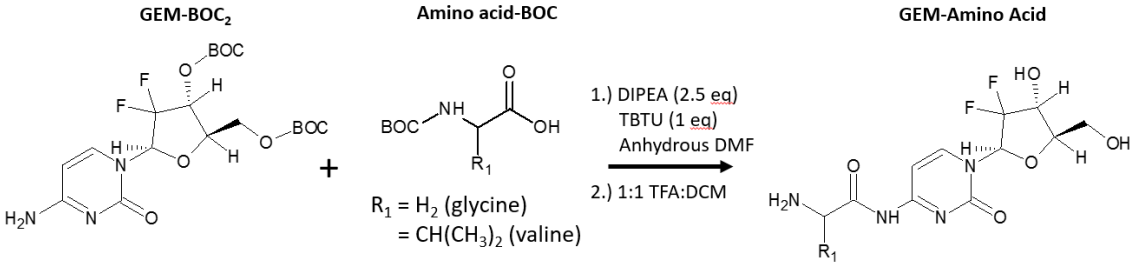

Figure 5.1: Synthesis scheme for GEM prodrugs: GEM-glycine and GEM-valine.

Interestingly, the UV-vis spectrum of the prodrug changes significantly after conjugating to the amine group (peak shifts from ∼270 to ∼250 nm), consistent with previous reports [197]. This provided a convenient way to distinguish between GEM and GEM-amino acids prodrugs, without doing HPLC.

5.3 Synthesis and characterization of HA conjugates

HA-GEM and HA-DOX conjugates were synthesized with different release rates to evaluate the effect of release rate on synergy. GEM prodrugs were conjugated directly to HA with

carbodiimide chemistry (Fig. 5.2), and the release rate of GEM was dependent upon the amino acid used to link GEM to HA. DOX was conjugated to HA directly with an amide bond and with a hydazone bond through an adipic acid dihydrazide linker (Fig. 5.2). HA-DOX-GEM was synthesized by first conjugating the adipic acid dihydrazide linker, then conjugating the GEM prodrug, and lastly conjugating DOX. Reaction time and reactant ratio could be adjusted to manipulate DOX and GEM loading.

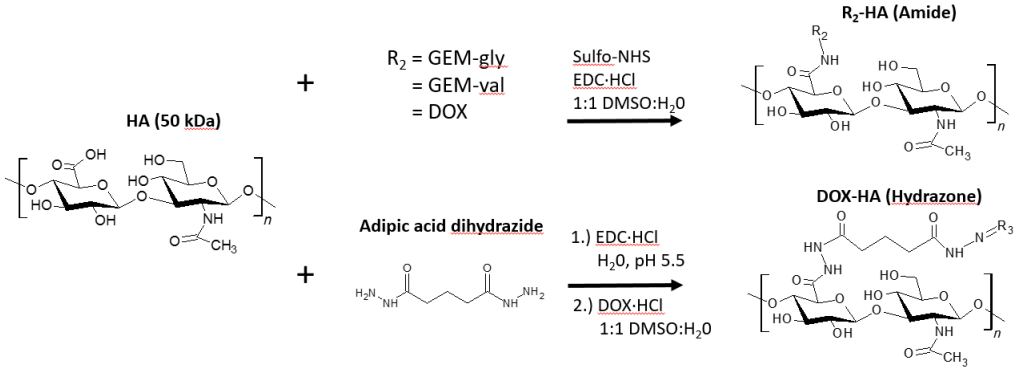

Figure 5.2: Synthesis scheme for conjugating drugs to HA with an amide bond making: GEM-gly-HA, GEM-val-HA, and DOX-HA and the synthesis scheme for conjugating DOX to HA with a hydrazone bond

Drug loading and vehicle size of each PDC is summarized in Table 5.1. Drug loading up to 8.9 and 11.9 wt % could be achieved with GEM and DOX, respectively, while maintaining solubility in PBS. While drug loading is measured with UV absorbance (example spectrum show in Fig. 5.3), GEM drug loading was also verified with ^{1}H NMR (Fig. 5.4), using the aromatic protons on GEM-gly (7.2 and 8.2 ppm) and the HA methyl protons (1.9 ppm). The degree of loading of ADH was quantified with ^{1}H NMR using the ethylene protons on ADH (1.6 and 2.3 ppm) (Fig. 5.4). Consistent with previous reports, DOX loading could not be quantified with ^{1}H NMR because no aromatic proton signals were observed, most likely due to DOX remaining in the core of self-assembled HA conjugates [135].

Regardless of GEM loading, HA-GEM conjugates were measured to be 10 nm in diameter

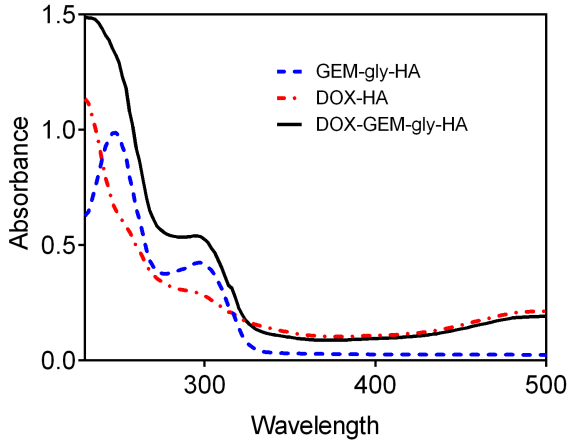

Figure 5.3: UV absorbance spectrum of DOX-HA hydrazone, GEM-gly-HA, and DOX-GEM-gly-HA

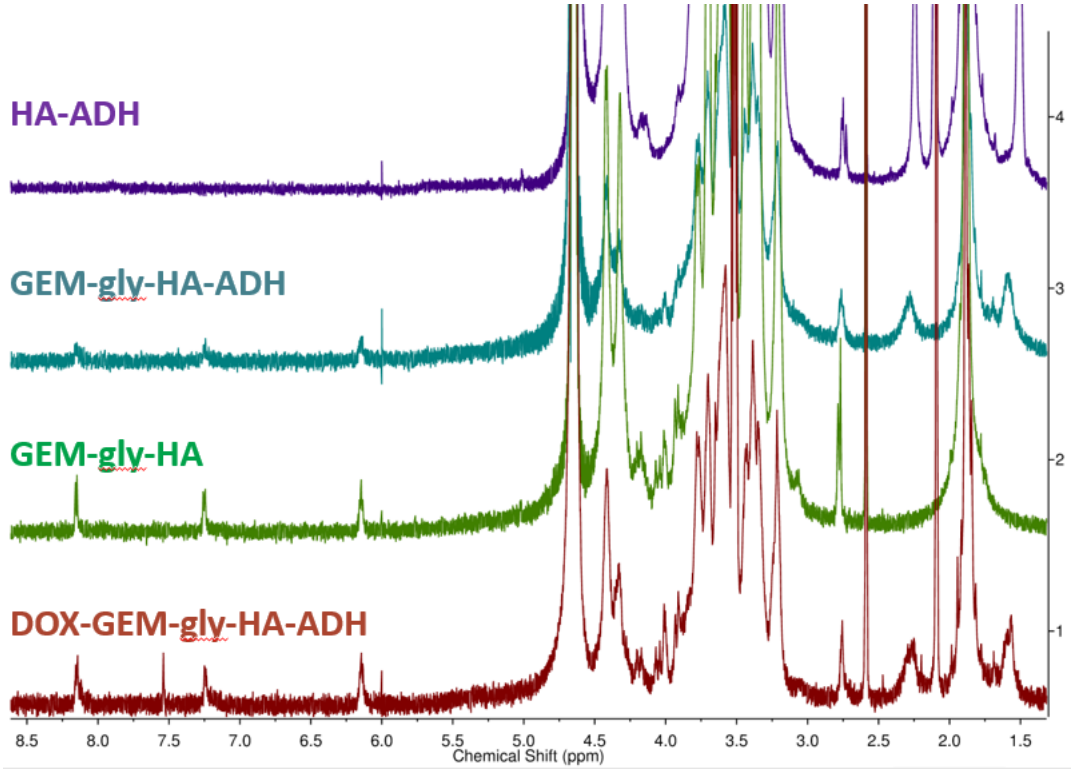

Figure 5.4: ^{1}H NMR of HA conjugates with DOX and GEM (D_2O, 600 MHz)

with DLS with no larger structures observed with cryo TEM (Fig. 5.5). This suggests, that GEM did not induce any assembly between separate HA-GEM polymers. On the contrary, all conjugates containing DOX, were measured to be approximately 20 to 100 nm in size with DLS, which was confirmed with cryo TEM images (Fig. 5.5). As DOX loading was increased, larger structures (100-200 nm) were evident, suggesting the self-assembly of the conjugates is due to the hydrophobic nature of DOX.

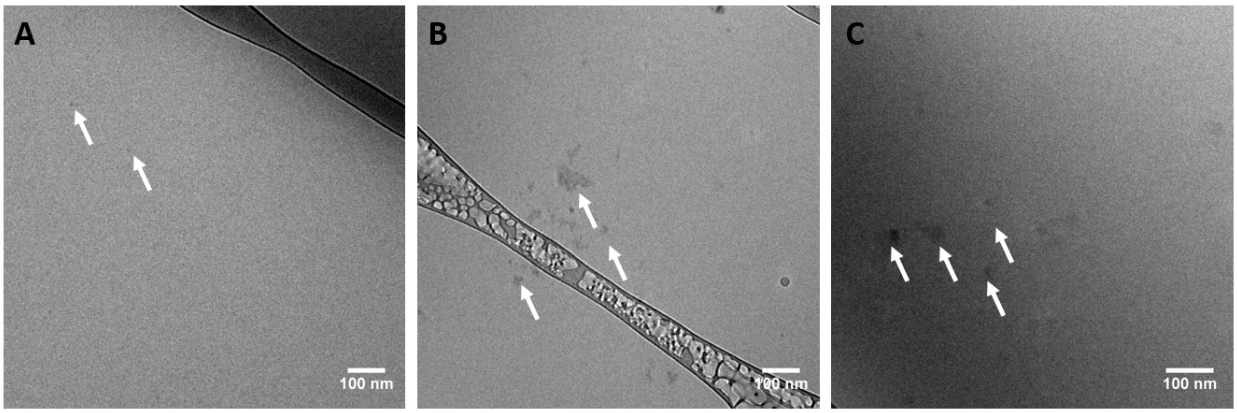

Figure 5.5: Cryo TEM of (a) GEM-gly-HA, (b) DOX-HA, and (c) DOX-GEM-gly-HA.

Table 5.1: Characterization of drug-HA conjugates

Conjugate	DOX loading (wt. %)	GEM loading (wt. %)	DLS number mean (nm)
DOX-HA amide	1.5	–	10.5 ± 3.0
DOX-HA hydrazone	i.) 4.3 ii.) 11.8	– –	i.) 65 ± 28 ii.) 106 ± 51
GEM-gly-HA	– –	i.) 3.9 ii.) 5.7	i.) 8.8 ± 2.5 ii.) 11.7 ± 2.2
GEM-val-HA	–	4.0	11.7 ± 2.2
DOX-GEM-gly-HA	i.) 2.5 ii.) 3.6	i.) 3.6 ii.) 5.0	i.) 24.8 ± 5.0 ii.) 22.3 ± 5.0

5.4 Cellular toxicity of HA conjugates

The toxicity of the drug-HA conjugates and the release kinetics of each drug was measured (Fig. 5.6). Less than 10 % of DOX is released from the DOX-HA amide conjugate after 100 h; however, approximately 50 % of DOX is hydrolyzed from the DOX-HA hydrazone conjugate. This release is quicker in acidic pH ($t_{1/2} = 107 \pm 11$ h (pH 5) vs $t_{1/2} = 141 \pm 18$ h (pH 7.4)). The toxicity of the conjugates on MDA-MB-231 cells (Fig. 5.6a) and 4T1 cells (Fig. 5.8) is reflective of the availability of released DOX, as free DOX is more toxic than DOX-HA hydrazone which is more toxic than DOX-HA amide. This is also evident by looking at DOX internalization. After 24 h incubation, the majority of free DOX is inside the nucleus, while most of the DOX after incubation with DOX-HA hydrazone is still outside of the nucleus, most likely in endosomes (Fig. 5.7).

While both GEM prodrugs were conjugated to HA with an amide bond, the release rate of GEM from the construct is different based on the amino acid used to conjugate GEM to HA. GEM is hydrolyzed quicker from GEM-gly-HA ($t_{1/2} = 88 \pm 5$ h (pH 5), 28 $\pm$ 2 h (pH 7.4)) than from GEM-val-HA ($t_{1/2} = 179 \pm 12$ h (pH 5), 124 $\pm$ 14 h (pH 7.4)) in both neutral and acidic conditions. Again, the toxicity of the constructs on MDA-MB 231 cells (Fig. 5.6) and 4T1 cells (Fig. 5.8) is correlated with the availability of free drug, as free GEM is more toxic than GEM-gly-HA which is more toxic than GEM-val-HA.

In order to test the hypothesis that a mixture of conjugates which exposes the cells to GEM prior to DOX is more synergistic than other sequences, the toxicities of different mixtures of GEM and DOX conjugates were evaluated on MDA-MB-231 cells. Because DOX is hydrolyzed extremely slow from DOX-HA amide, as reflected with the minimal toxicity, DOX-HA hydrazone is used for the remainder of the studies. The toxicities of DOX-HA alone and physical, equimolar mixtures of DOX-HA with GEM-val-HA, GEM-gly-HA, and free GEM were evaluated (Fig. 5.10). All equimolar, physical mixtures of DOX-HA with GEM are more

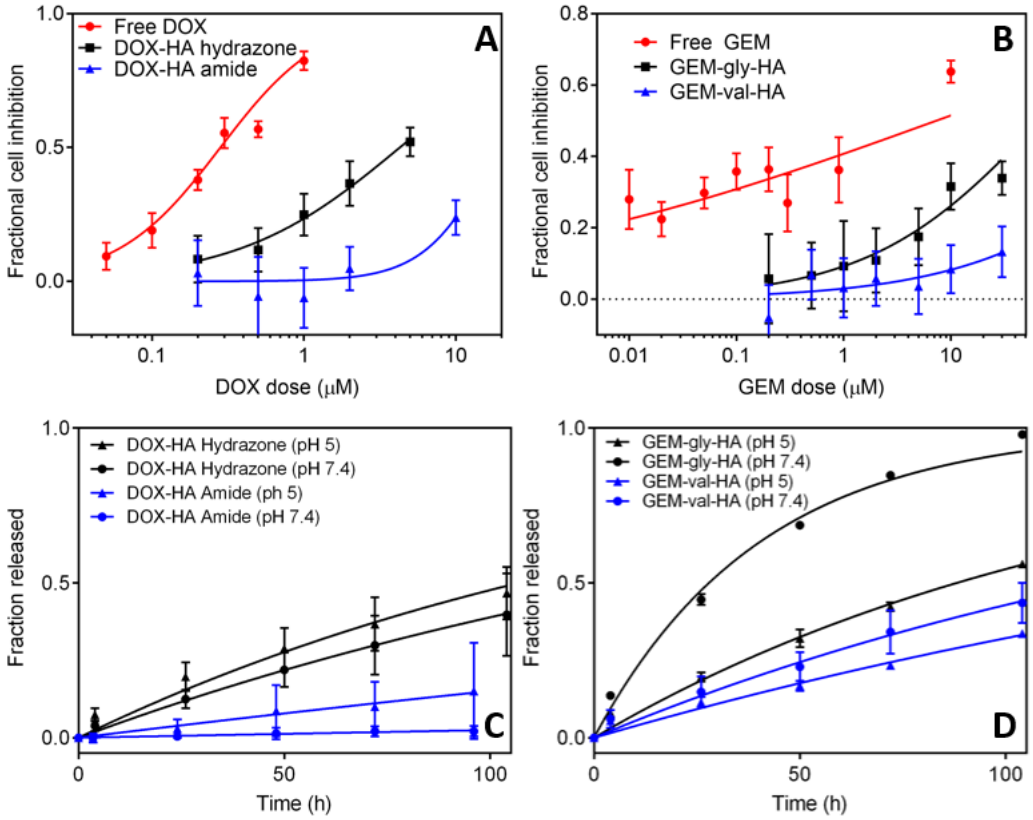

Figure 5.6: Cell inhibition of MDA-MB-231 cells comparing the toxicity of DOX to DOX-HA conjugates (a) and GEM to GEM-HA conjugates (b). Cells were incubated for 72 h with formulations and cell viability was measured with the MTT assay. Data represent mean $\pm$ SD (n $\geq$ 12 wells). Release kinetics of DOX-HA conjugates (c) and GEM-HA conjugates (d) measured with dialysis. Data represents mean $\pm$ SD (n $\geq$ 3).

toxic than DOX-HA alone due to synergy of the drugs, even though GEM conjugates are minimally toxic at this low concentration (Fig. 5.6). In addition, mixtures which contain a form of GEM that is available relatively faster than DOX (GEM-gly-HA and free GEM) than those that contain a form of GEM that is released slower than DOX (GEM-val-HA) are more toxic.

DOX-GEM-gly-HA was also synthesized and evaluated because GEM is released relatively faster than DOX with this combination (Fig. 5.6 and Fig. 5.9). The combination conjugate is more toxic than the physical mixture of DOX-HA and GEM-gly-HA, most likely due to more of the drug being internalized due to less overall polymer. The synergy of the combination

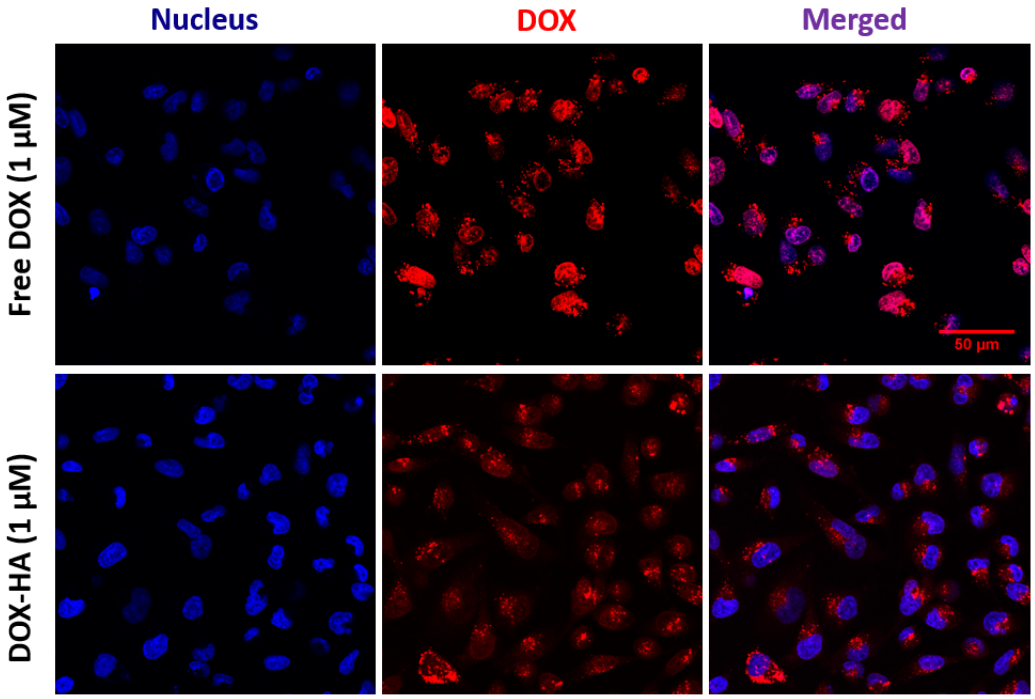

Figure 5.7: Confocal images of DOX and DOX-HA hydrazone internalization after 24 h incubation with MDA-MB-231 cells (1 μM DOX). Nuclei are stained with Hoechst 33342. Free DOX is localized into the nucleus while DOX-HA is located primarily outside of the nucleus.

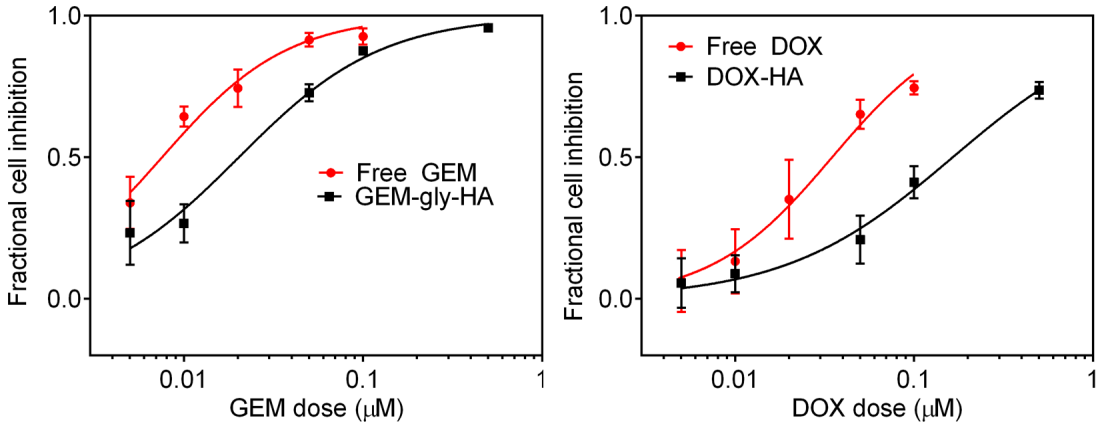

Figure 5.8: Cell inhibition of 4T1 cells comparing the toxicity of GEM to GEM-gly-HA (a) and DOX to DOX-HA hydrazone conjugate (b). Cells were incubated for 72 h with formulations and cell viability was measured with the MTT assay. Data represent mean $\pm$ SD (n $\geq$ 12 wells)

conjugate was also verified with a combination index less than 0.5 across a wide range of toxicities (Fig. 5.10b).

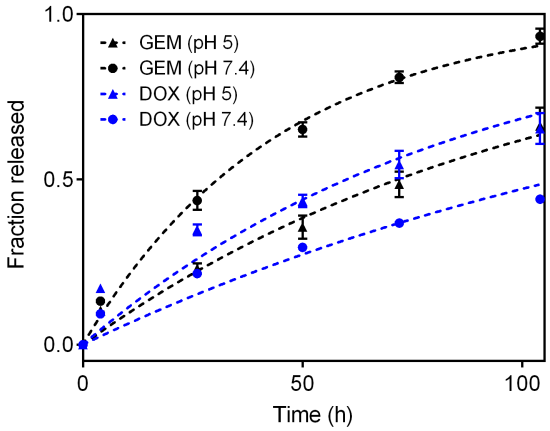

Figure 5.9: Release of DOX and GEM from DOX-GEM-gly-HA measured with dialysis in PBS at pH 5 and 7.4. Data represents mean ± SD. (n=3)

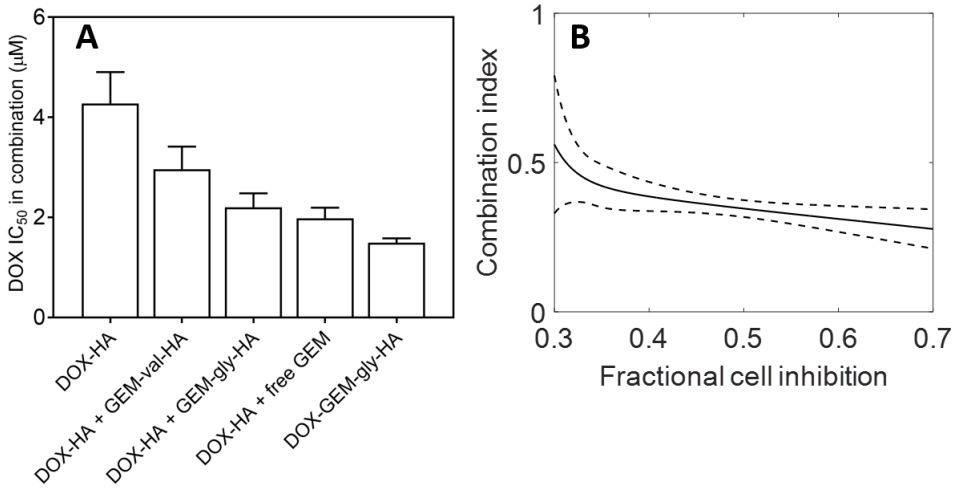

Figure 5.10: (a) Comparing the concentration of DOX in DOX-HA alone, a physical mixture of DOX-HA with GEM-val-HA, GEM-gly-HA, or free GEM, and DOX-GEM-gly-HA that inhibits 50 % MDA-MB-231 cell growth. Cell inhibition was measured with the MTT assay after incubating the cells with drug formulations for 72 h. (b) The degree of synergy of DOX-GEM-gly-HA compared to DOX-HA and GEM-gly-HA calculated with the combination index. Data represents mean ±95% confidence interval (n ≥ 12 wells).

The cell cycle distribution of MDA-MB-231 cells was also measured after exposure to HA-

drug conjugates (Fig. 5.11). The cell cycle distribution after exposure to DOX-HA and both GEM-HA conjugates mimicked the distribution after exposure to the free drugs, discussed in Chapter 4. After exposure to the physical combination of GEM-gly-HA and DOX-HA and the combination conjugate DOX-GEM-gly-HA, the cell cycle distribution of the cells mimicked that of free GEM as well. This is consistent with the cellular response after cells were exposed to GEM 1 d prior to DOX.

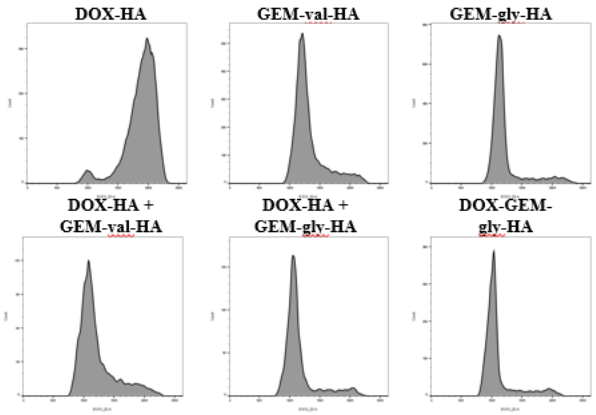

Figure 5.11: Cell cycle distribution (measured with P.I. nuclear staining) after 72 h exposure to HA-drug conjugates (1 μM).

5.5 *In vivo* efficacy of HA conjugates

To evaluate the efficacy of the polymer conjugates *in vivo*, a mouse model with an intact immune system (orthotopic, 4T1 tumor model) was selected to ensure realistic clearance rates of the HA carrier. The individual conjugates (DOX-HA and GEM-gly-HA), the free drug combination (DOX+GEM), and the optimal polymer drug conjugate (DOX-GEM-gly-HA) were all injected i/v every third day (starting 4 days post tumor transplantation) for a total of four injection cycles. Doses of DOX (2 mg/kg) and GEM (2.75 $\pm$ 0.3 mg/kg) were the same in each group.

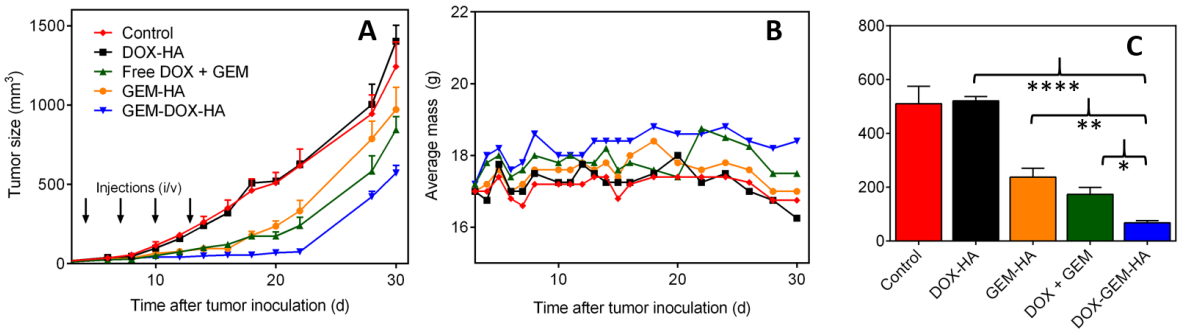

Figure 5.12: Tumor growth study in an orthotopic, 4T1 tumor model. (a) Tumor growth curve for DOX-HA, GEM-HA, DOX-GEM-HA, and the physical mixture of DOX and GEM. The dose for DOX and GEM in each group is 2 and 2.75 $\pm$ 0.3 mg/kg, respectively, and 4 total doses were given every 3rd day starting on day 4 post tumor inoculation. (b) Average body mass throughout the tumor study. (c) Comparison of average tumor size on day 20. Data represents mean $\pm$ SEM ($n = 4$ for DOX-HA, $n = 5$ for every other group). Statistical significance is calculated with students, unpaired t-test.

DOX-HA showed no tumor reduction compared to a control group with no treatment, while GEM-gly-HA showed significant reduction in tumor size. The free drug combination of DOX and GEM also reduced tumor size a significant amount; however, the combination drug conjugate (DOX-GEM-gly-HA) significantly inhibited more tumor growth (Fig. 5.12). The tumors in the mice treated with the combination conjugate eventually relapsed after treatment stopped. Using the low drug doses, no body weight loss was observed for any of the conjugate groups, but 2 mice treated with the free drug combination suffered greater than 15 % body weight loss.

5.6 Optimization of delivery site and dose

While the majority of polymer drug conjugates are administered intravenously, HA conjugates can be administered through various parenteral administration routes because HA is continuously recycled in many different tissues throughout the body. For example, HA conjugates were previously administered peritumorally (with a subcutaneous injection) to effectively treat mammary tumor xenografts with no observable local inflammation at the injection site

[134, 113]. By changing the injection site, distribution of the conjugate and tumor exposure to each drug can be manipulated, impacting tumor regression.

Using the same doses as previously used (2 mg/kg DOX and 2.75 mg/kg GEM), DOX-GEM-HA conjugates were injected intraveneously, and subcutaneously, in the inguinal mammary gland opposite the tumor and peritumorally. The exact locations of the subcutaneous injections are shown in Fig. 5.13c, and they were chosen to ensure that the conjugates could slowly drain into the inguinal and axillary lymph nodes. For each group, dosing frequency was extended to every 5 d (as opposed to every 3 d), in an attempt to extend mouse survival and to minimize potential local inflammation at the site of the s/c injections.

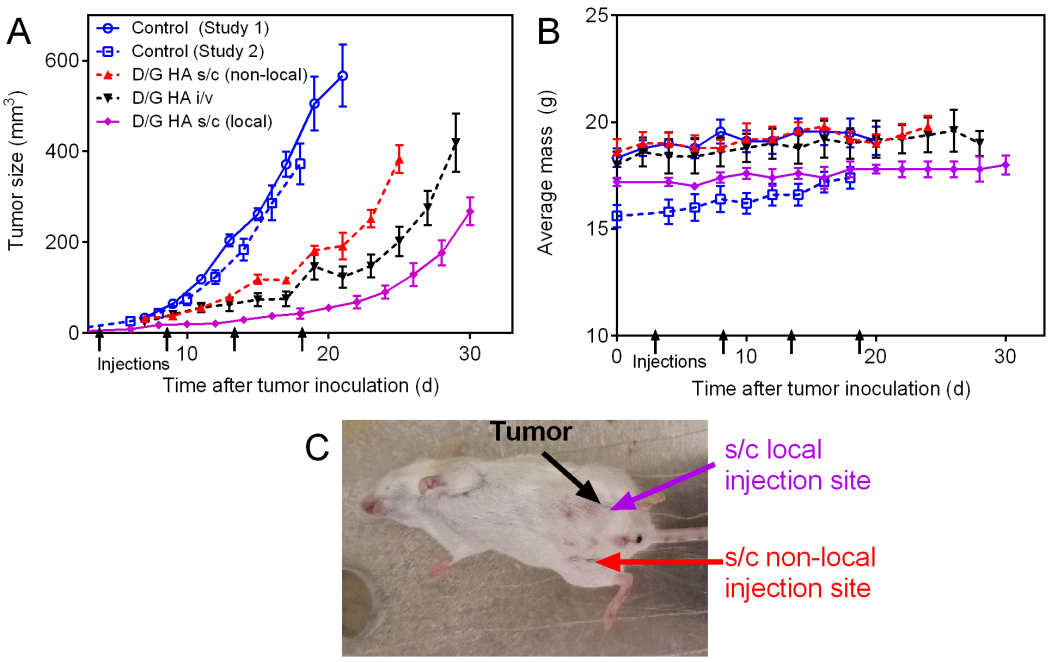

Figure 5.13: Tumor growth study in an orthotopic, 4T1 tumor model comparing administration route of DOX-GEM-HA. (a) Tumor growth curve for DOX-GEM-HA administered i/v and s/c in the inguinal mammary fat pads peritumorally (local) and bilaterally to the tumor (non-local). The dose for DOX and GEM in each group is 2 and 2.75 mg/kg, respectively, and 4 doses were given every 5th day starting on day 4 post tumor inoculation. (b) Average body mass for each treatment group. (c) Image of inguinal, s/c injection sites relative to tumor location. Data represents mean $\pm$ SEM ($n = 5$)

Tumor growth was significantly inhibited in each group, and no body weight loss was observed for any group (Fig. 5.13a-b). The mice which received local, s/c injections (peri-tumoral) had the slowest tumor growth, but tumors still relapsed after treatment was stopped. Interestingly, nonlocal, s/c injections were nearly as effective as i/v injections at inhibiting tumor growth, indicating that s/c injections can be used to treat cancer systemically. While no signs of toxicity were observed for the i/v injected mice, a few mice which received s/c injections showed hair loss near the injection site.

Because serious toxicity was not observed for the conjugate groups, a higher dose of DOX-GEM-HA was administered in an attempt to completely eradicate the tumors. Due to solubility limitations, conjugates could not be synthesized with twice as high drug loading without forming large aggregates. A higher s/c injection volume permitted administering DOX-GEM-HA at twice the dose as previously used (4 mg/kg DOX, 5.5 mg/kg GEM), while still using a conjugate with the same drug loading. The injection volume could not be increased for bolus i/v injections, so DOX-GEM-HA was administered with a higher GEM and lower DOX drug loading (1 mg/kg DOX, 5 mg/kg GEM).

For the non-local, s/c injections, the higher dose resulted in a significant reduction in tumor growth (Fig. 5.14). During the injection cycle, the tumors treated with the high dose did not grow at all, while those treated with the low dose grew at a slow rate. While no major toxicity was observed for either group, the higher dose injection resulted in more hair loss near the injection site than the low dose injection. For the i/v injection groups, the conjugates with a high GEM loading inhibited tumor growth more than the conjugates with a lower GEM but higher DOX loading (Fig. 5.14). Furthermore, tumors treated with DOX-GEM-HA intravenously (with a high GEM loading) did not relapse until approximately 10 d after the last injection, which resulted in tumors maintaining a volume below 100 mm^3 20 d longer than the tumors that received no treatment.

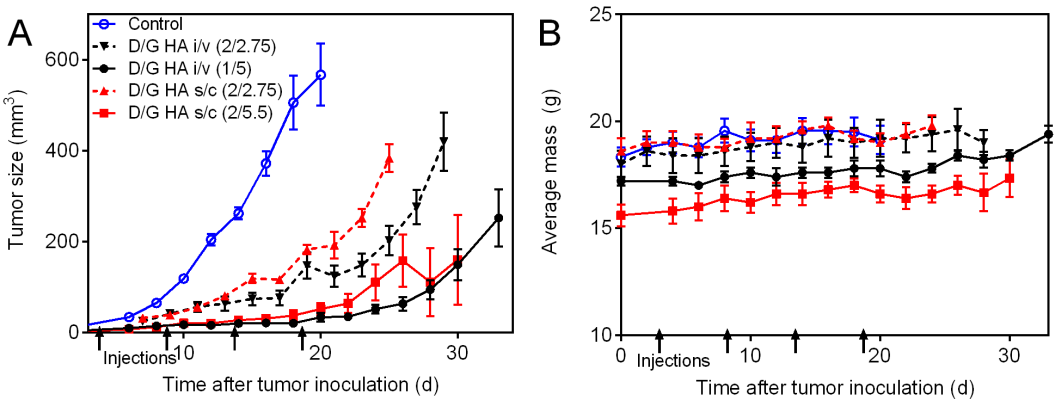

Figure 5.14: Tumor growth study in an orthotopic, 4T1 tumor model comparing dose of DOX-GEM-HA. (a) Tumor growth curve for DOX-GEM-HA administered i/v and s/c in the inguinal mammary fat pad bilaterally to the tumor (non-local) at different doses. Doses for each group are shown in the figure (DOX mg/kg / GEM mg/kg). (b) Average body mass for each treatment group. Data represents mean $\pm$ SEM ($n = 5$)

5.7 Discussion on HA conjugates

While drug schedule plays a significant role in cellular toxicity when giving GEM and DOX in bolus sequences in vitro, the impact of schedule upon differential release from a drug delivery carrier was unknown. To study this, DOX and GEM were conjugated to HA with varying release rates for proof of principle. Similar to previous reports, DOX was conjugated to HA with both an acid labile linker and a stable, amide bond [134, 135, 111]. To conjugate GEM to HA with varying release rates, prodrugs were formed with amino acids, and the bulkiness of the amino acid controlled the hydrolysis of GEM from HA, similar to previous synthetic strategies with PTX [199]. Contrary to the DOX conjugation strategies, the ability to control the release of GEM by performing chemistry on the drug prior to conjugation to the polymer makes it significantly easier to control the release rate of the drug.

The toxicity of the individual conjugates, relative to free drug, is reflective of the bioavailability of the drug (Fig. 5.6 and 5.8). When combining the conjugates at an equimolar ratio, the

toxicity significantly increases when GEM is available relatively faster than DOX, as evident by the decrease in the IC_{50} of the combination when combining DOX-HA with GEM-val-HA (3.0 $\pm$ 0.4 μM), GEM-gly-HA (2.2 $\pm$ 0.2 μM), and free GEM (1.9 $\pm$ 0.2 μM). These results are consistent with the free drug, bolus, scheduling data, showing the benefit of releasing GEM relatively faster than DOX when giving the two in combination. In addition, the cell cycle distribution of cells incubated with the optimal combination of conjugates is similar to that of physically giving GEM to DOX, providing evidence that the cells are being exposed to the effects of GEM prior to that of DOX (Fig. 5.11). Interestingly, the optimal combination conjugate DOX-GEM-gly-HA was much more active than the physical mixture of the two conjugates *in vitro*, likely due to a slight increase in the release rate of DOX from the combination conjugate compared to DOX-HA on its own (Fig. 5.9) or due to an increase in conjugate internalization with DOX-GEM-gly-HA compared to the combination of DOX-HA and GEM-gly-HA.

The efficacy of the conjugates were tested *in vivo* in an immune competent, orthotopic 4T1 tumor model. Injecting every 3 d intravenously, the combination conjugate (DOX-GEM-HA) was effective at stopping tumor growth up to 10 d post treatment, which was significantly more effective than the individual conjugate treatments (DOX-HA and GEM-HA) and the free drug combination (DOX+GEM). Although the free drug combination was moderately effective at inhibiting tumor growth, multiple mice had to be euthanized due to weight loss. No weight loss was observed for any of the conjugate groups, indicating minimal acute toxicity associated with the treatments.

Previous studies have shown the benefits of sequentially giving single drug PDCs *in vivo* with other chemotherapeutics [130, 129], but a similar therapeutic benefit can be obtained by conjugating both drugs to the same polymer backbone and controlling the release rate of the drugs. While it is more difficult to conjugate two drugs to the same polymer, you can control the exact ratio and schedule that the cells see *in vivo* by having a single delivery vehicle. This

can help ensure that cells are sensitized *in vivo* to a second drug similarly to preliminary *in vitro* studies. Controlling the relative release rate of drugs from combination delivery vehicles is something that should be thoroughly studied and controlled in the future to maximize therapeutic benefit of combination delivery vehicles.

In addition to intravenous injection, HA conjugates have been administered through other parenteral routes in pre-clinical and clinical studies to alter drug biodistribution. Here, we show that DOX-GEM-HA can effectively treat 4T1 tumors administered both locally and subcutaneously in inguinal mammary fat pads. While the i/v injections were the most effective administration route, the ability to still treat with s/c injections opens up a promising area for future research. It was not surprising that the local, s/c injection was effective at inhibiting tumor growth, but it was surprising that the non-local s/c injections were almost as effective as i/v injections at inhibiting tumor growth. This demonstrates that local, s/c injections of HA conjugates can still be used to effectively treat cancer metastases elsewhere in the body. The exact mechanism of whether the drug reaches systemic circulation already released from HA, as a reduced molecular weight HA conjugate, or as the original HA conjugate is currently under investigation. Previous studies suggest that the HA is being degraded into small HA oligomers in the lymphatic system prior to entering systemic circulation.

Furthermore, by delivering the conjugates subcutaneously in the mammary fat pads, the conjugates will drain into the same lymph nodes which are responsible for cancer metastasis. Previous studies have shown that accumulation of delivery vehicles into the lymph nodes can prevent future metastasis by killing the tumor cells before they enter systemic circulation. Future studies can study how effective DOX-GEM-HA is at preventing cancer metastasis with highly, metastatic cancer cells lines *in vivo*.

Chapter 6

Optimizing delivery of LAP and PTX with bi-phasic nanoparticles

Lapatinib (LAP) was originally approved for treating late stage, HER2+ breast cancer in combination with capecitabine. Since then, it has been tested in various clinical trials as a substitute for trastuzumab in combinations with other chemotherapeutic agents. In particular, LAP and paclitaxel (PTX) have been evaluated for treatment of various phenotypes of metastatic breast cancer [200, 201, 202, 203, 204]. The addition of LAP to PTX chemotherapy regimens has extended the survival of patients with metastatic, HER2+ cancer while being mostly ineffective for HER2- patients [200, 201, 203]. In addition, LAP and PTX have proven to be effective in treating HER2+ breast cancer patients in the neoadjuvant setting [204]. The use of high doses of LAP has also been used to increase the delivery of albumin bound PTX to various solid tumors by reducing the hyperpermeability of the tumor vasculature [205].

Given the early clinical success of PTX and LAP, it is important to ensure that the two drugs are being administered in an optimal manner. However, designing the optimal combination regimen for PTX and LAP is a challenge because LAP is given orally while PTX is administered intravenously with the solubilizing oil Cremaphor EL. To ensure the drugs reach

the tumor site simultaneously, various delivery systems have been synthesized to co-deliver the two hydrophobic agents. In particular, LAP and PTX have been loaded into the core of micelles [206, 207, 208, 209], liposomes [210], injectable hydrogels [211], and layer by layer nanoparticles [212]. In many of the studies, the combination vehicles were synergistic at inhibiting the growth of both HER2+ cancer cells and many multi-drug resistant cancer cell lines.

To engineer an optimal carrier and maximize synergy for LAP and PTX, it is advantageous to control both the molar ratio and drug release kinetics; however, current delivery systems do not allow for control over release kinetics of each drug. On the contrary, bi-phasic nanoparticles would allow for the drugs to be loaded into distinct compartments which degrade at different rates. Previously, biphasic nanoparticles have been synthesized with microfluidic and electrohydrodynamic (EHD) co-jetting processes [213]. In particular, EHD co-jetting has been used to synthesize particles containing compartments with different physical properties [214]. These particles have been engineered to carry small molecule therapeutics, siRNA, and imaging agents for various therapeutic applications [215, 216, 217]. In addition, the particles can be synthesized as less than 200 nm, allowing for extended circulation [218, 219].

While current delivery platforms are effective at deliverying LAP and PTX in combination, the release rate of each drug from the delivery platforms is governed by the physical structure of the vehicles. Further efficacy may be achieved by optimizing the sequence and ratio in which the drugs are administered. Previously, pretreatment with trastuzumab (which also inhibits the HER2 receptor) prior to PTX was more effective at initiating apoptosis in HER2+ cancer cells than the simultaneous exposure of the two agents. However, there is no way to manipulate the relative release rates of the drugs from the current delivery platforms. Therefore, we have designed a novel, bi-phasic polymeric nanoparticle delivery system to allow for the drugs to release at different rates. The particles are synthesized with EDH co-jetting, and the toxicities of different particle systems are compared.

6.1 Synergy of LAP and PTX in BT-474 cells

Using BT-474 cells as a representative cell line for HER2+ breast cancer, the toxicity of both LAP and PTX were determined for different drug exposure times (Fig. 6.1). The 72 h IC_{50} doses for PTX and LAP were determined to be 14 ± 1 nM and 85 ± 10 nM, respectively. Decreasing the exposure time of each drug from 72 h to 24 h increased the IC_{50} dose 6x and 3x for PTX and LAP, respectively. On the contrary, delaying the exposure of PTX and LAP for 24 h increased the IC_{50} dose approximately 3x for both drugs.

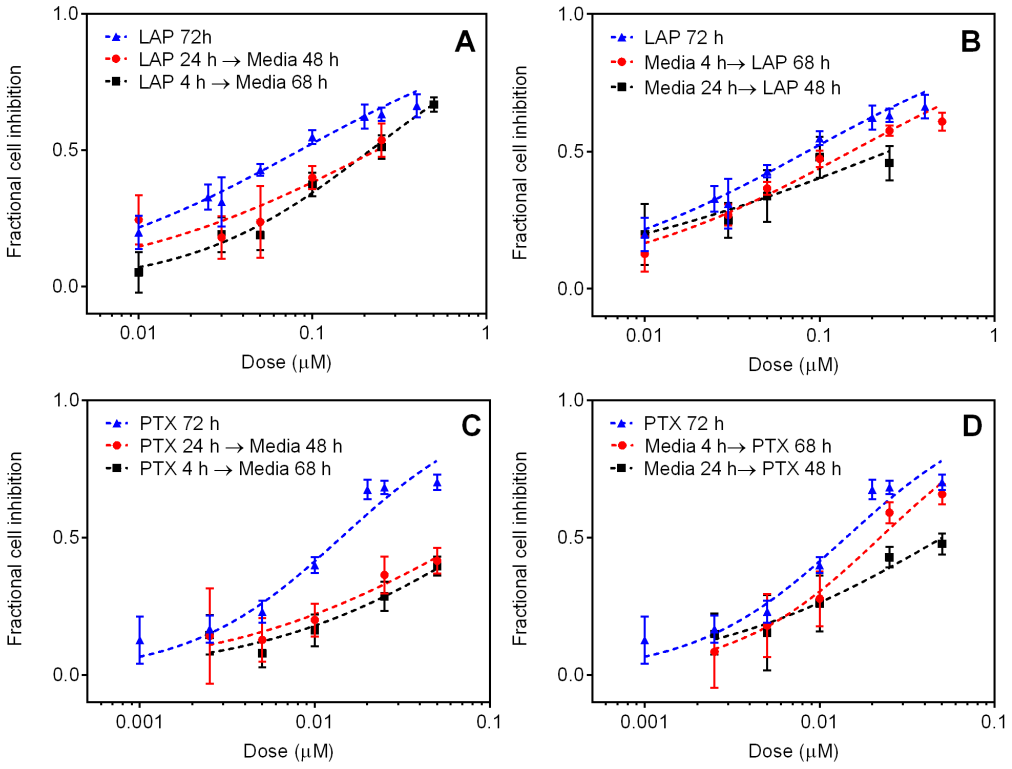

Figure 6.1: Fractional cell inhibition and relevant dose response curves for BT-474 cells after exposure to (a) LAP → media (b) media → LAP (c) PTX → media (d) media → PTX. Cell viability was assessed at 72 h for each schedule. Error bars represent 95 % CI ($n \geq 12$ wells).

After identifying the relative toxicity of each drug on its own, cellular proliferation was measured after exposure to combinations of LAP and PTX. Using a fixed molar ratio of 3:1

(LAP:PTX), near the IC_{50} of each drug, the cells were exposed to different schedules of drugs (Fig. 6.2a). Given the cell viability after exposure to the individual drugs compared to the combination treatments (Fig 6.2b), it was determined that giving LAP 4h prior to PTX is significantly more synergistic than giving the two drugs simultaneously (Fig 6.2c). This is true if you leave LAP present after PTX exposure or if you remove extracellular LAP after PTX exposure. In addition, it is also synergistic if you give PTX prior to LAP; however, the combination is not as toxic as exposing the cells to LAP first.

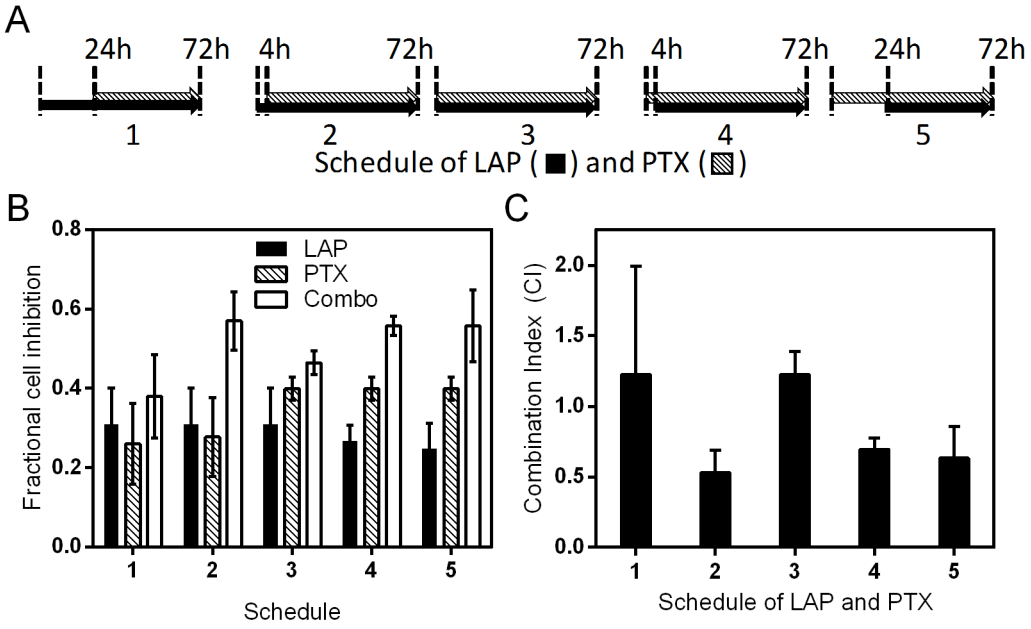

Figure 6.2: Toxicity as a function of different schedules of LAP (0.03 μM) and PTX (0.01 μM) on BT-474 cells (a) 72 h incubation schedule of LAP and PTX. (b) Fractional cell inhibition as a function of different LAP and PTX schedules evaluated with MTT assay. (c) Combination index as a function of schedule. (Error bars represent 95% confidence intervals (n $\pm$ 6 wells))

Using the optimal schedule of LAP (4 h) $\rightarrow$ PTX/LAP (68 h), the effect of molar ratio on synergy between LAP and PTX was studied. With a PTX dose below the IC_{50} (0.10 μM), molar ratios of LAP:PTX greater than 1 are synergistic (CI $<$ 1). However, as you increase

the dose of PTX significantly above the IC_{50} (0.30 μM), the synergy is less than at lower PTX doses. This is likely due to the fact that at this high concentration, PTX is already significantly toxic on its own.

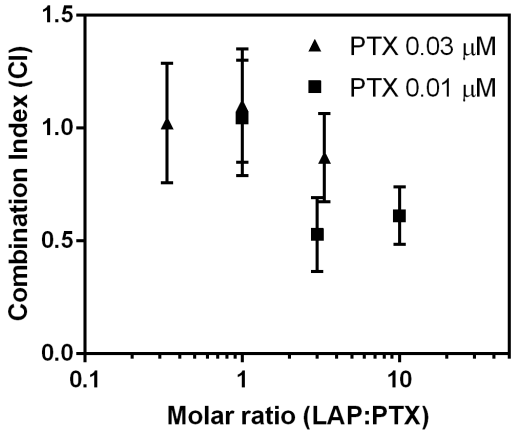

Figure 6.3: Synergy as a function of LAP:PTX molar ratio when exposing cells to LAP (4 h) $\rightarrow$ LAP/PTX (68 h) (Error bars represent 95% confidence intervals (n $\geq$ 12 wells))

6.2 Synthesis of bi-phasic nanoparticles with LAP and PTX

Bi-phasic spherical nanoparticles were synthesized with EHD co-jetting [214]. Briefly, two polymeric solutions flow through a needle under laminar flow conditions. An electric field is applied and the droplet at the tip of the needle breaks into a thin thread. The thread breaks into small droplets, and the solvent quickly evaporates, leaving behind polymeric nanoparticles. Becuase the fluid flow had two laminar streams, the resulting particle can contain multiple compartments. Fig. 6.4 shows a cartoon schematic of the process.

Both LAP and PTX were loaded into single bi-phasic nanoparticles by including the drugs in the polymeric solutions. By incorporating each drug into different compartments, particles with differential drug release kinetics could be obtained. Particles have an average size of 160

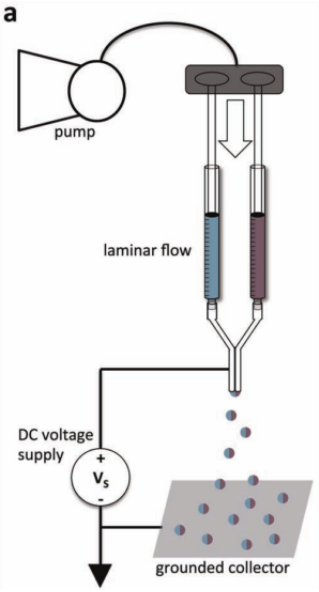

Figure 6.4: Cartoon schematic of EHD process used to fabricate bi-phasic nanoparticles. Reprinted from [216] with permission from Wiley.

nm with low polydispersity (Fig. 6.5). The bi-phasic structure of the particles was verified with SIMS by loading different fluorescent molecules into each of the polymer phases in the nanoparticles (PLGA and PLGA/AcDEX).

To demonstrate the difference in degradation of each of the polymer phases, Rhodamine B was incorporated into the AcDEX/PLGA compartment and Coumarin into the PLGA compartment. The release kinetics of each fluorescent molecule was measured with dialysis and fluorimetry. The stability of both polymer phases was evident by the slow release kinetics of the fluorescent molecules at pH 7.4 (Fig 6.6a). At pH 5, the release of Rhodamine B from the AcDEX/PLGA compartment phase of the nanoparticles is significantly faster than that of Coumarin from the PLGA compartment. (Fig 6.6c). This was also evident after changing the pH of the solution from pH 7.4 to pH 5 (Fig 6.6b). The quick release from the acetylated dextran phase in acidic pH compared to neutral pH is clearly shown in Fig 6.6d.

After establishing that the AcDEX/PLGA compartment releases fluorescent dyes faster than the PLGA compartment, biphasic nanoparticles were co-jetted with LAP and PTX. The

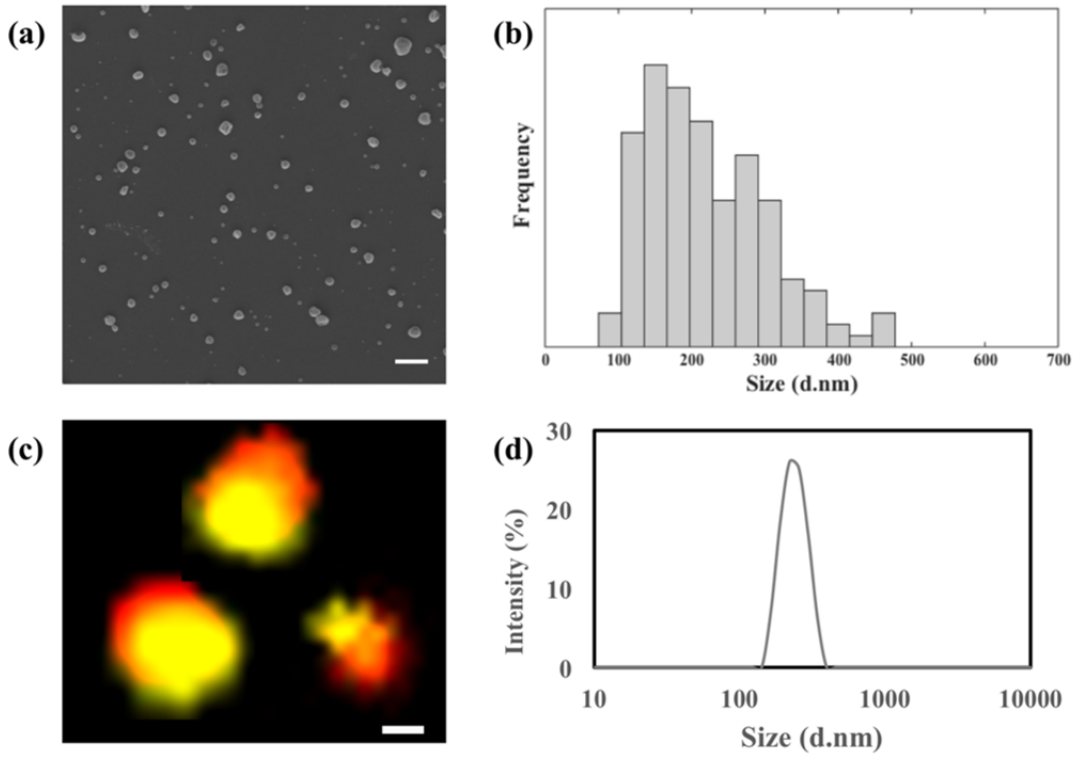

Figure 6.5: SEM image (a) and relevant particle size distribution (b) of co-jetted, pH responsive Janus nanoparticles (Mean diameter: 166 $\pm$ 61.2 nm, Scale bar, 1 μm). (c) Super-resolution images of dye-loaded Janus nanoparticles with Structured Illumination Microscopy (SIM) demonstrating their biphasic architecture (Scale bar, 200 nm). (d) Dynamic Light Scattering (DLS) measurement. Estimated mean hydrodynamic diameter is 240 $\pm$ 47 nm.

drugs were loaded into different compartments to change the releative relase rate of each drug (Table 6.1). Control particles were also made with just a single drug or no drug. While each particle system was jetted with LAP and PTX concentrations to give final drug loadings of 2.7 and 5.5 wt. %, respectively, approximately a 4-fold lower drug loading remained after washing each particle type, determined with HPLC (Table 6.1).

Prior to determining how effective the drug loaded particles were at inhibiting cancer cell growth, the toxicity of the blank particles were determined on MDA-MB-231 cells and BT-474 cells (Fig. 6.7). Up to a particle concentration of 3 μg/mL, no toxicity was observed for the blank particles. Higher concentrations of the particles were not evaluated because these particle

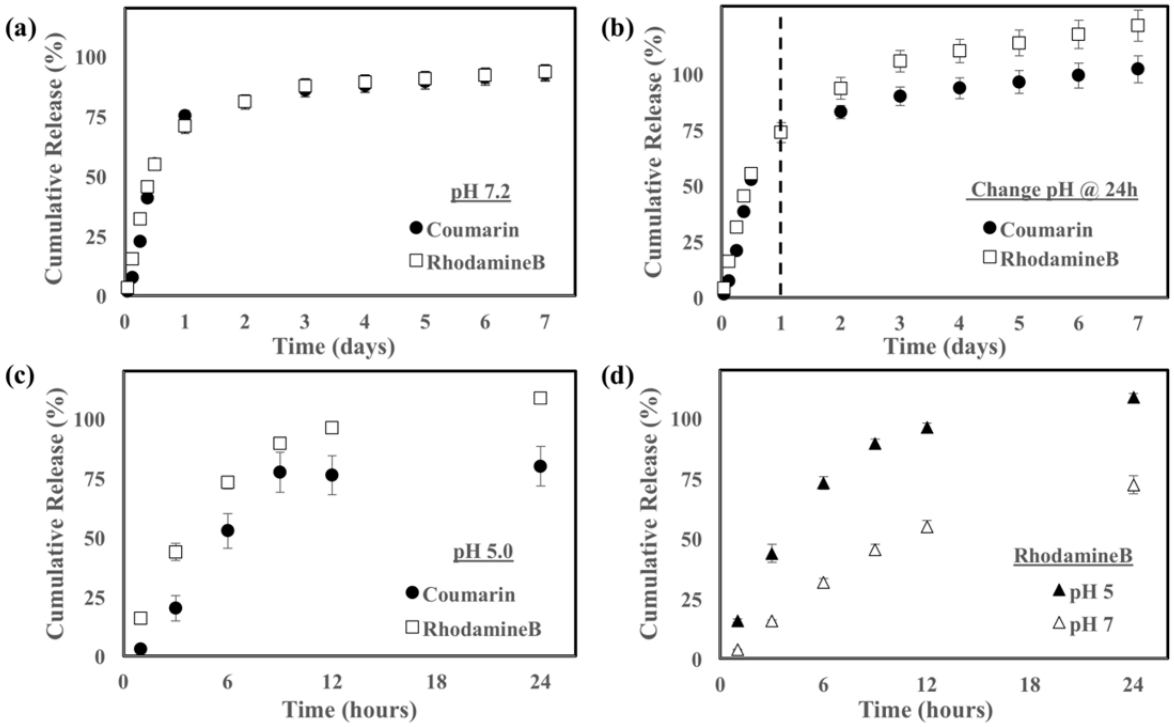

Figure 6.6: Release of Coumarin 314 and Rhodamine B dyes from PLGA and PLGA/AcDex compartments: (a) Extended cumulative release at physiological pH 7.4. (b) pH responsive release following pH change from 7.4 to 5.0 at 24 h time point. (c) Cumulative release during first 24 h at pH 5.0. (d) Release of Rhodamine B from pH responsive compartment at pH 7.4 and 5.0.

Table 6.1: Synthesis of biphasic nanoparticles with different loadings of PTX and LAP

Particle Name	AcDEX/PLGA comp.	PLGA comp.	PTX (wt. %)	LAP (wt. %)
P1	LAP	PTX	0.71	1.24
P2	LAP + PTX	–	0.65	1.29
P3	PTX	LAP	∼0.7	∼1.2
PTX control	–	PTX	0.76	–
LAP control	LAP	–	–	∼1.2
Blank	–	–	–	–

concentrations were sufficiently high for toxicity testing with the drug loaded particles.

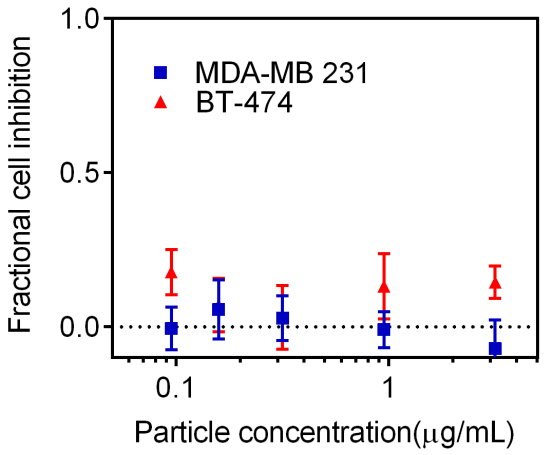

Figure 6.7: Fractional cell inhibition of MDA-MB-231 and BT-474 cells after 72 h exposure of blank bi-phasic nanoparticles. Error bars represent 95 % CI (n $\geq$ 6 wells).

6.3 Growth inhibition of HER2+ breast cancer cells

The toxicity of each combination biphasic nanoparticle was evaluated on BT-474 cells (Fig. 6.8). The biphasic particles which contained LAP in the AcDEX/PLGA compartment and PTX in the PLGA compartment induced the most cellular toxicity of the particles loaded with both drugs. Both particles which contained PTX and LAP in different compartments (P1 and P3), have a lower PTX IC_{50} (2.2 ± 0.4 nM and 7.8 ± 0.9 nM, respectively) than free PTX (14 ± 1 nM). Interestingly, the particle system which contained both drugs in the AcDEX/PLGA compartment (P2), is not as toxic as free PTX. All combination particle systems are significantly more toxic than free LAP at the concentrations tested.

The cellular toxicity of the most toxic combination vehicle (P1) was compared to single drug loaded particles with LAP and PTX in the AcDEX/PLGA and PLGA compartments, respectively. The dual loaded particle (P1) was considerably more toxic than both the PTX and LAP control particles (Fig. 6.9), which had similar drug loadings to the dual loaded particle (Table 6.1). In addition, the dual loaded particle (P1) is much more effective at inhibiting

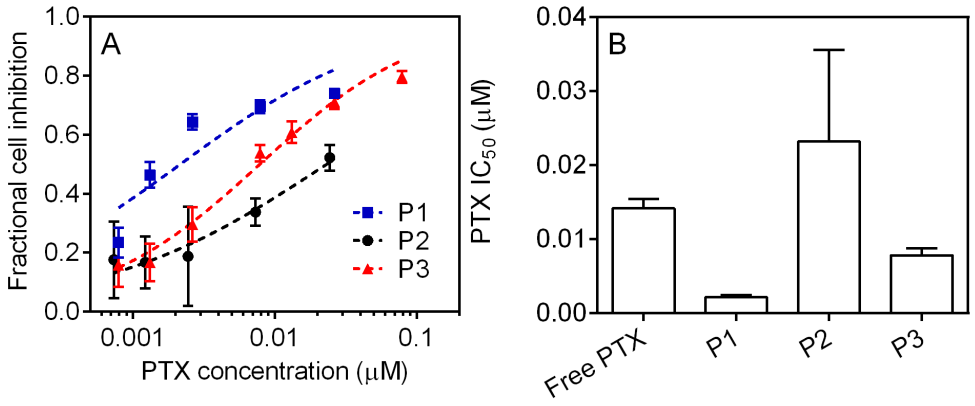

Figure 6.8: (a) Fractional cell inhibition of BT-474 cells after 72 h exposure to the following bi-phasic particles: P1 (AcDEX/PLGA: LAP, PLGA: PTX), P2 (AcDEX/PLGA: LAP + PTX, PLGA: blank), and P3 (AcDEX/PLGA: PTX, PLGA: LAP) Points are experimental data and lines are best fit median effect model. (b) PTX IC_{50} concentrations for each particle type. Error bars represent 95 % CI (n $\geq$ 12 wells)

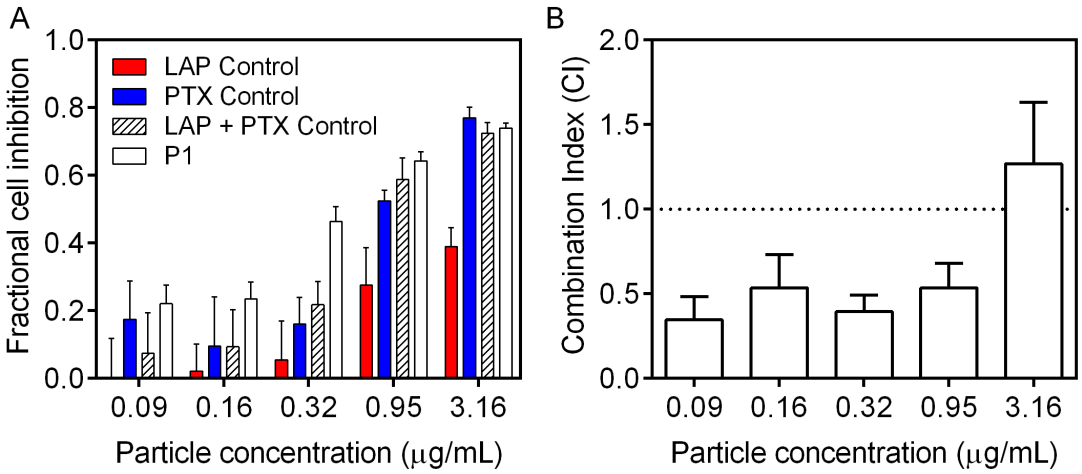

Figure 6.9: (a) Fractional cell inhibition of BT-474 cells after 72 h exposure to the following bi-phasic particles: LAP control (AcDEX/PLGA: LAP, PLGA: blank), PTX control (AcDEX/PLGA: blank, PLGA: PTX), LAP control + PTX control, and P1 (AcDEX/PLGA: LAP, PLGA: PTX) Points are experimental data and lines are best fit median effect model. (b) Combination index (CI) for particle P1. Error bars represent 95 % CI (n $\geq$ 6 wells).

BT-474 cell growth than a physical mixture of LAP and PTX control particles at similar drug concentration. Compared to the single drug loaded particles, the dual loaded particles are synergistic at inhibiting cell growth (CI < 0.5) for particle concentrations less than 1 μg/mL (Fig. 6.9b).

6.4 Extension to HER2- breast cancer cells

The toxicity of the bi-phasic nanoparticles was also evaluated on triple negative breast cancer cells (MDA-MB-231). Because triple negative cells are HER2-, LAP is ineffective at inhibiting MDA-MB-231 growth. Using LAP concentrations which are relevant to the particle systems (up to 100 nM), LAP does not inhibit any MDA-MB-231 growth. However, LAP has shown to enhance the toxicity of other cytotoxic drugs on HER2- cancer cells by inhibiting drug efflux pumps [220, 221].

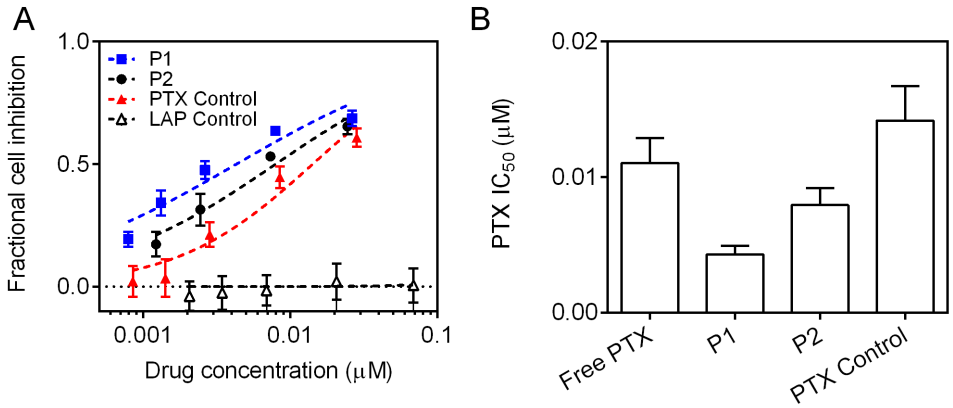

Figure 6.10: (a) Fractional cell inhibition of MDA-MB-231 cells after 72 h exposure to the following bi-phasic particles: LAP control, PTX control, P1, and P2. Points are experimental data and lines are best fit median effect model. (b) PTX IC_{50} concentrations for each particle type. Error bars represent 95 % CI (n $\geq$ 12 wells).

Interestingly, both dual loaded particle systems are more toxic than the single loaded PTX particles on MDA-MB-231 cells, even though the single loaded LAP particles show no signs

of toxicity (Fig. 6.10). The IC_{50} for the dual loaded particles P1 and P2 is 3x and 2x lower, respectively, than the single loaded PTX particles. In addition, the most toxic dual loaded particle (P1) has a significantly lower IC_{50} than free PTX (P1: 4.3 ± 0.6 nM, free PTX: 11 ± 2 nM).

6.5 Discussion on LAP/PTX bi-phasic nanoparticle system

LAP has been used in combination with many other chemotherapeutics in the clinic due to its ability to enhance tumor inhibition. In particular the combination of LAP and PTX has proven to be an effective drug combination for treating late stage, metastatic breast cancer. Here, we show that the drug pair is synergistic at inhibiting the growth of HER2+ breast cancer cells only if given in the correct sequence. We then demonstrate that we can synthesize bi-phasic nanoparticles which are capable of controlling both the molar ratio of LAP and PTX and the relative release rate of each drug.

The HER2+ cell line BT-474 is responsive to both LAP and PTX with single drug IC_{50} values in the nM range; however, the combination of LAP and PTX is not synergistic if the cells are exposed to both drugs simultaneously defeating the purpose of combining the two drugs. If the schedule of drug administration is tweaked, such that the one drug is exposed prior to the other drug, the combination becomes synergistic indicating a lower drug dose can be administered to achieve the same cellular growth inhibition. Synergy is the highest when LAP is given 4 h prior to PTX at a molar ratio of LAP:PTX of 3:1. For the optimal schedule, the combination index (CI) is approximately 0.5, indicating that a 2x fold lower dose of PTX can be given. It is evident that synergy between LAP and PTX is highly dependent upon both the schedule and molar ratio of LAP and PTX while treating BT-474 cells. This is consistent with a previous study which showed that trastuzumab can only enhance the toxicity of PTX on HER2+ cancer cells if the cells are exposed to trastuzumab first [222].

The strong dependence of drug ratio and schedule on drug synergy, makes it difficult to translate an effective combination dosing regime to the clinic due to the complicated pharmacokinetics of each drug. Various nano-sized delivery vehicles have been synthesized to carry both LAP and PTX to ensure that cancer cells are exposed to the drugs simultaneously; however, drug release from these vehicles cannot be changed without changing the physical structure of the vehicle and/or drug loading process [206, 207, 208, 209, 210, 211, 212]. Here, we used EHD co-jetting to synthesize biphasic nanoparticles which enable us to manipulate the release rate and molar ratio of drug-loaded particles without drastically changing the drug loading technique and/or overall particle structure.

Biphasic nanoparticles were synthesized with one compartment containing AcDEX/PLGA and one compartment containing PLGA. The particles are less than 200 nm, ideal for extended particle circulation and accumulation in tumors with leaky vasculature. The biphasic morphology of the nanoparticles was verified with SIMS, and each compartment degrades and releases fluorescent dye at a different rate. The AcDEX/PLGA compartment is pH responsive and degrades significantly faster in acidic pH than the PLGA compartment. It is expected that the drugs which are loaded into the AcDEX/PLGA compartment will be available to the cell faster than drugs loaded in the PLGA compartment, due to the acidic environment in endosomes and lysosomes. Furthermore, while not shown here, the composition of the AcDEX/PLGA compartment can also be manipulated to further tweak the relative release rate of each compartment.

Both LAP and PTX could be loaded into either particle compartment, so dual loaded particles were synthesized varying which compartment each drug was loaded in. Particles which contained LAP in the AcDEX/PLGA compartment and PTX in the PLGA compartment were considerably more toxic to BT-474 cells than the particles which contained both LAP and PTX in the AcDEX/PLGA compartment. This is consistent with the free drug data, which shows that exposing BT-474 cells to LAP prior to PTX is more synergistic than exposing the cells

to both drugs concurrently. Furthermore, the dual loaded particles were more toxic than the single drug loaded particles at the same drug dose, demonstrating that synergy is maintained between PTX and LAP. Surprisingly, the dual drug loaded particles were also more toxic to triple negative breast cancer cells (MDA-MB-231), even though the cells are unresponsive to LAP on its own. The enhanced toxicity is likely due to the inhibition of efflux drug pumps with LAP [220, 221]; however, further research is required to explore this effect in detail.

The main advantage of using dual drug loaded particles is that cells are exposed to the drug pair simultaneously *in vivo*, regardless of how the individual drugs distribute in the body. However, it is often advantageous to expose the cells to one drug prior to the other drug. Here, the therapeutic activity of dual loaded PTX/LAP particles could be manipulated *in vitro* by changing the relative release kinetics of the drug pair by changing which compartment the particles were incorporated into. The ability to manipulate individual drug release kinetics, provides another adjustable parameter while designing combination drug particles. Previous studies have synthesized core-shell particles to release one drug relatively faster than another drug; however many of these systems rely on differences in drug hydrophobicity to load into different regions of the particle [65, 66, 67, 68, 69]. On the contrary, by using EHD co-jetting, the relative release rate of PTX and LAP, and the resulting cellular toxicity, could easily be manipulated by changing jetting conditions.

While the dual loaded particles containing LAP in the AcDEX/PLGA compartment were most effective at inhibiting cancer cell growth *in vitro* on BT-474 cells and MDA-MB-231 cells, this will not be true for all cell lines. Furthermore, other pairs of chemotherapeutic agents will demonstrate schedule-dependence, motivating the development of new delivery platforms capable of controlling the release rate of multiple therapeutics. Moving forward, the effect of drug release needs to not only be evaluated with respect to cancer cell toxicity *in vitro*, but also with respect to healthy cell toxicity and *in vivo* efficacy. Regardless of the drug combination, the effect of drug schedule should be critically evaluated when designing a delivery vehicle to

carry multiple agents.

Chapter 7

Development of microfluidic technique to measure local solute concentrations

The focus of the work in this chapter was to develop a new microfluidic technique, capable of measuring solute concentration with high spatial and temporal resolution. Both the resolution and the precision of the technique are characterized with standard microfluidic experiments, to offer insight into the physical systems the technique can be used to probe in future studies. Furthermore, the utility of the technique is demonstrated by measuring solute transport.

7.1 Microfluidic techniques to measure solute concentration

The field of microfluidics continues to grow as novel microfluidic tools are developed, offering solutions to a broad range of scientific and technical problems and applications. Recent advances have enabled the rapid generation of complex chemical environments, such as well defined gradients (e.g. for fundamental chemotaxis studies and high throughput screens of chemical reaction conditions) [223, 224, 225, 226, 227, 228]. Unfortunately, few general methods exist to measure the dynamic chemical profiles *in situ* in microfluidic devices.

Many techniques have been developed to generate chemical gradients on the micro scale. One of the most common is to generate gradients with repeated T-junctions of miscible fluids [229, 230, 231]. Although the technique allows for the design of gradients with various shapes, drawbacks include the need to precisely control the pressure of each inlet stream and that the gradient is developed in laminar flow streams. Recently, new methods were developed to generate chemical gradients with diffusive transport, eliminating convection in the region of interest [232, 233, 234, 235, 236, 237, 238, 239]. The technique entails having a microchip with a closed dialysis chamber (CDC), isolated from a source and sink channel by gel membranes that allow for solute diffusion. CDCs allow both fast chemical switching and rapid generation of complex chemical gradients due to small length scales [239, 235, 234, 233].

With continued advancements in microfluidic gradient generation, the need to measure these concentration fields *in situ* increases. For example, the dynamics involved in developing a chemical gradient in a CDC requires knowledge of the transport processes involved in the dialysis membranes and in the CDC, which will be species specific. A general method to measure concentration fields *in situ* would facilitate the quantification of transport processes in the exact experimental system. Moreover, many systems of scientific, industrial, and technological relevance involve time-dependent processes in which materials precipitate, crystallize, dissolve, react, or equilibrate. Such processes, in turn, involve spatio-temporally evolving concentration fields of solute and solvent. Unfortunately, there is a lack of reliable and general methods to measure spatial concentration profiles *in situ*.

In microfluidic systems, fluorescence microscopy is commonly used to measure the spatial concentration profile of chemicals. Although the technique is quick and easy to set up, chemicals must be tagged with a fluorophore, potentially affecting their function and transport properties; moreover, photo bleaching can lead to erroneous measurements. Other techniques have been adapted to microsystems, including Raman spectroscopy [240, 241, 242], Fourier transform infrared (FT-IR) spectroscopy [243], and Coherent Anti-Stokes Raman scattering

(CARS) microscopy [244], allowing for the spatial visualization of chemical species without fluorescent labeling. In particular, *Schafer et al* have resolved 3D concentration profiles with sub-μm resolution using CARS microscopy; however, minutes are required to resolve concentration gradients over $\sim 100\,\mu m$ [244]. On the contrary, *Chan et al* resolved multiple chemical concentration profiles over multiple millimeters in seconds with FT-IR spectroscopy; however, the technique only has a lateral resolution of 40 μm [243].

Refractive index measurements provide another strategy to measure concentration profiles. Various interferometric techniques have been adapted to microfluidic systems to precisely measure the average refractive index of a single (as low as $\sim \mu m^3$) point in space, down to 10^{-4} to 10^{-7} RIU, including a mach-zender interferometer [245], a back scattering interferometer [246], a Young interferometer [247], and Fabry-Perot interferometers [248, 249, 250]. To our knowledge, only one refractometry method, consisting of a Fabry-Perot interferometer with a monochromator, is able to resolve spatial refractive index profiles in a fluidic system [251]. This technique is optimized for measurements in nanofluidic channels and not immediately applicable to measuring evolving concentration profiles in microfluidic channels.

Here we demonstrate a Fabry-Perot interferometric system designed to measure the local concentration of chemical species in microchannels with or without flow. Fabrication of the Fabry-Perot chip is relatively simple, and the *Fringes of Equal Chromatic Order* (FECO) are generated directly on an inverted microscope and imaged with a spectrometer and CCD camera, enabling the technique to be easily utilized to study various transport processes in microfluidic devices. By following the displacement of the FECO fringes, we resolve changes in refractive index down to 2×10^{-5} RIU. A spatially resolved spectrometer enables the local refractive index to be measured with 1 μm resolution. The temporal resolution on each measurement is ~ 0.05s and is only limited by the sensitivity of the camera.

We first describe the fabrication of the interferometer and the experimental methods used to track the FECO fringes. We then discuss the spatial and temporal resolution and precision of

the refractrometry method by looking at the concentration of chemicals in rectangular channels with homogenous concentrations. Lastly, we use the technique to measure the diffusive evolution of chemical gradients in microfluidic channels to measure binary diffusion coefficients and concentration dependence and to track the evolution of chemical gradients in CDCs.

7.2 Fabry-Perot microfluidic interferometer development

Here we describe the fabrication of the microfluidic interferometer chip, the acquisition of FECO fringes, and the image analysis used to determine refractive index as a function of space and time.

7.2.1 Microfluidic chip fabrication

A microfluidic device consisting of a single, 90 μm layer between semi-reflective glass surfaces was fabricated (Fig. 7.1). After drilling inlet holes into one of the glass slides, electron-beam evaporation (SEC600, CHA, Industries) was used to deposit a 5 nm adhesion layer of Ti and 50 nm layer of Ag onto the glass slides to make them semi reflective. Oxidation of the silver layer (which can reduce the performance of the device due to a decrease in finesse) was observed over a few days; however, this can be delayed if a longer lifetime is desired by storing devices under vacuum when not in use or by depositing a protective SiO_2 layer [251]. Even with oxidation, devices still performed effectively weeks after fabrication.

A laser cutter (Trotec Speedy 100) was used to cut channels into the double sided tape (Permanent Double Sided Tape, Scotch), which was then sandwiched between the two glass slides by applying pressure. While the laser cutter allows for any tape design with feature sizes down to 100 μm, smaller features are possible with standard lithography techniques, if necessary. PDMS inlets were then ozone bonded to the top glass slide to hold inlet and outlet tubing. The device was then baked at 80 °C for at least 4 hours to strengthen bonding.

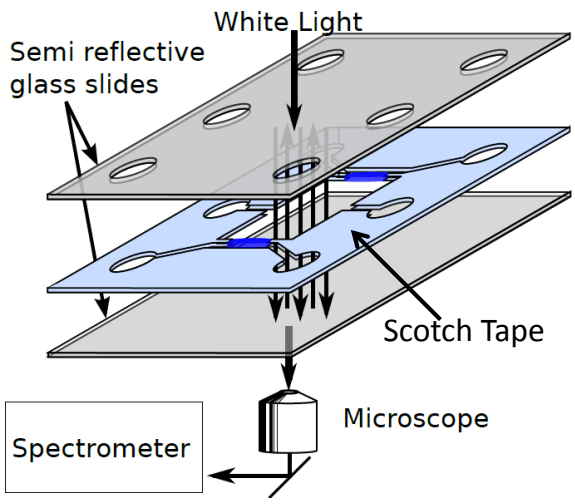

Figure 7.1: Diagram of light path in microfluidic, Fabry-Perot interferometer.

7.2.2 Multiple beam FECO interferometry

FECO interferometry, which is used to simultaneously measure film thickness and refractive index in the surface forces apparatus (SFA), was used to measure spatial refractive index profiles [252]. An inverted microscope was used to focus white light on the device from above. The semi-reflective surfaces allow for constructive and deconstructive interference within the device, and the transmitted light was focused onto a spectrometer slit with a microscope objective (Fig. 7.1). The spectrometer (Shamrock series 300, 600 lines/mm grating) was connected to the outlet of the microscope and a CCD camera (Andor Luca-R) was used to gather images from the spectrometer (Fig. 7.2a). The horizontal axis in each image corresponds to the physical dimension in which light is obtained in the slit, while the vertical axis corresponds to the wavelength of diffracted light.

Due to the superposition of light waves which are reflecting between the two semi-reflective surfaces, the intensity of transmitted light though the interferometer is dependent on wavelength and the optical path. The intensity of transmitted light (I_t) through a one-layer multiple beam interferometer can be related to the intensity of normal incident light (I_0) via the Airy

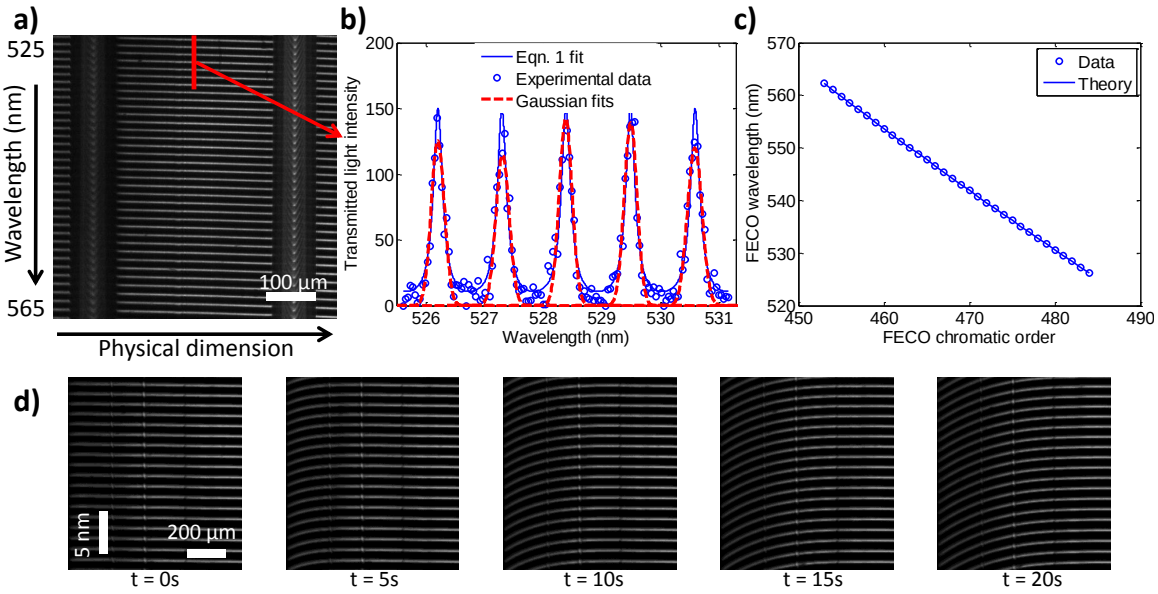

Figure 7.2: (a) Image of FECO fringes generated with microfluidic chip (see Fig. 7.5 for image of microfluidic chip). (b) Light intensity profile (taken at position shown in (a)) as a function of wavelength demonstrating Gaussian fitting to FECO fringe locations. (c) Wavelength of FECO fringes from (a) as a function of chromatic order fit to Eqn 7.2. (d) Shift in FECO fringe location due to diffusion of ethanol from the left (See Fig. 7.4 for image of microfluidic chip).

Function [253]:

$$I_t = I_0\left[\frac{1}{1+(\frac{2r}{1-r^2})^2\sin^2(\frac{2\pi nd}{\lambda})}\right] \tag{7.1}$$

where n is the refractive index of the layer, r the reflection coefficient of the mirrors, d the distance between the two reflective surfaces, and λ the wavelength of the incident light.

Fringes are observed at wavelengths of light which produce a maximum in transmitted light:

$$\lambda_m^F = \frac{2nd}{m} \tag{7.2}$$

where m represents the chromatic order of the fringe. The refractive index can be determined from Eqn. 7.2 with the distance between the reflective surfaces and the wavelengths of

two *Fringes of Equal Chromatic Order* (FECO) with unknown successive chromatic orders m and $m+1$:

$$n = \left(\frac{1}{2d}\right)\frac{\lambda_m^F \lambda_{m+1}^F}{\lambda_m^F - \lambda_{m+1}^F}. \tag{7.3}$$

Although the thickness of the microfluidic channel is not known with high precision, the absolute refractive index can still be determined with Eqn. 7.3. The thickness of the channel can be calculated by calibrating with a liquid of known refractive index. Using this method, the error in a refractive index measurement (δn) scales with the error in the measurement of FECO fringe wavelength ($\delta\lambda$) with $\frac{\delta n}{n} \sim (\frac{d}{\lambda})(\frac{\delta\lambda}{\lambda})$. Here, the error in measuring the wavelength of a fringe is approximately limited by the resolution of the spectrometer and camera ($\delta\lambda \sim 0.05\,nm$), giving a refractive index precision of approximately $10^{-2}\,RIU$.

In order to measure small changes in concentration, a much greater precision in refractive index is required. Relative shifts in refractive index over time (t_0 to t) can be determined with higher precision than the absolute refractive index, by using Eqn. 7.2 to track the relative shift of individual fringes:

$$n(t) = n(t_0)\frac{\lambda_m^F(t)}{\lambda_m^F(t_0)}. \tag{7.4}$$

Here, knowledge of the initial refractive index is required, but no calibration is needed. With this method, the error in the measurement of refractive index scales with $\frac{\delta n}{n} \sim (\frac{\delta\lambda}{\lambda})$. Therefore, the refractive index can be determined with a precision of approximately $10^{-4}RIU$ (a subpixel method improves the precision to $2\times10^{-5}RIU$). It is interesting to note that the thickness of the channel does not affect the precision; however, there are limitations on channel thickness. A channel taller than $\sim 1mm$ makes it difficult to resolve individual fringes, while a channel shorter than ∼wavelength of light will not produce any fringes.

7.2.3 FECO fringe acquisition

Refractive index profiles were determined using Eqn. 7.4. The initial refractive index of the system was known for each experiment; therefore, only the peak wavelength of a FECO fringe is required to determine dynamic refractive index profiles. Images of the interferometric patterns were acquired at each time step, and the wavelengths of FECO fringes were tracked over time with image analysis.

The wavelength-dependent, transmitted light intensity profile was measured for each horizontal pixel, which corresponds to a specific point in space. A custom-written MATLAB code located the initial location of FECO fringes by finding the location of local light maxima. Improved resolution for the FECO fringe locations was then obtained by approximating the Airy Function (Eqn. 7.1) as a series of Gaussian peaks (Fig. 7.2b). To verify that FECO fringes are being observed, the wavelengths of the fringes from Fig. 7.2b are plotted against successive chromatic orders (Fig. 7.2c), and found to agree with Eqn 7.2.

After identifying the initial location of the FECO fringes, the fringes were tracked at each point in space and time. Averaging the relative shift in wavelength of at least 5 fringes, a spatio-temporal refractive index profile was calculated by applying Eqn. 7.4. Refractive index profiles were then converted to concentration profiles using previously measured refractive index data in the *CRC Handbook* [254]. Fig. 7.2d shows example FECO fringes shifting due to diffusion of ethanol.

7.3 Characterization of technique

We now discuss the precision, accuracy, and resolution of measuring changes in refractive index. Fundamentally, the interferometry method is limited by the ability to precisely detect the position of the FECO fringes. Here, the accuracy and precision of the technique is independent

of the distance between the two reflective surfaces as long as the refractive index is homogenous in the optical path. Although no calibration is required, the initial refractive index must be known to determine the refractive index at a later time.

The noise associated with a refractive index measurement is proportional to the relative noise associated in identifying a fringe wavelength. When imaging with the camera and spectrometer grating previously described, each pixel corresponds to a wavelength of $0.04\,nm$. A FECO fringe shift of $0.04\,nm$ corresponds to a shift of $\sim 10^{-4}$ RIU in water. By fitting each fringe with a Gaussian function and averaging relative shifts in wavelength over multiple fringes, we obtain sub-pixel resolution.

To estimate the precision of fringe detection, static images of pure water were taken. The error in fringe position was determined by finding the standard deviation of the average difference between each fringe position and the respective mean fringe position, averaged over 5 fringes. For long exposure times ($> 1s$), the refractive index shift precision plateaus at 1.8×10^{-5} RIU (Fig. 7.3a). When the exposure time is reduced, the signal to noise ratio decreases, decreasing the precision of the technique (Fig. 7.3a). However, even with an exposure time as short as 50 ms, the precision in refractive index remained less than 10^{-4} RIU, indicating that transient processes with time scales of 50 ms can be tracked.

Small measurement drifts are observed during long experiments (> 10 min). To quantify the drift, the refractive index of flowing water and stagnant air was measured over a day, at multiple positions in a microfluidic channel. The measurement can homogeneously increase or decrease up to $\sim 10^{-4}$ RIU/h during the day and night, respectively, throughout the microfluidic channel (Fig. 7.3a, inset). These observations suggest that the drift is due to temperature fluctuations leading to expansion/compression of the whole tape layer. For this paper, all measurements were taken within 10 min and the drift was negligible; however, the small drift can be corrected for by measuring the refractive index of a static solution during the course of the experiment.

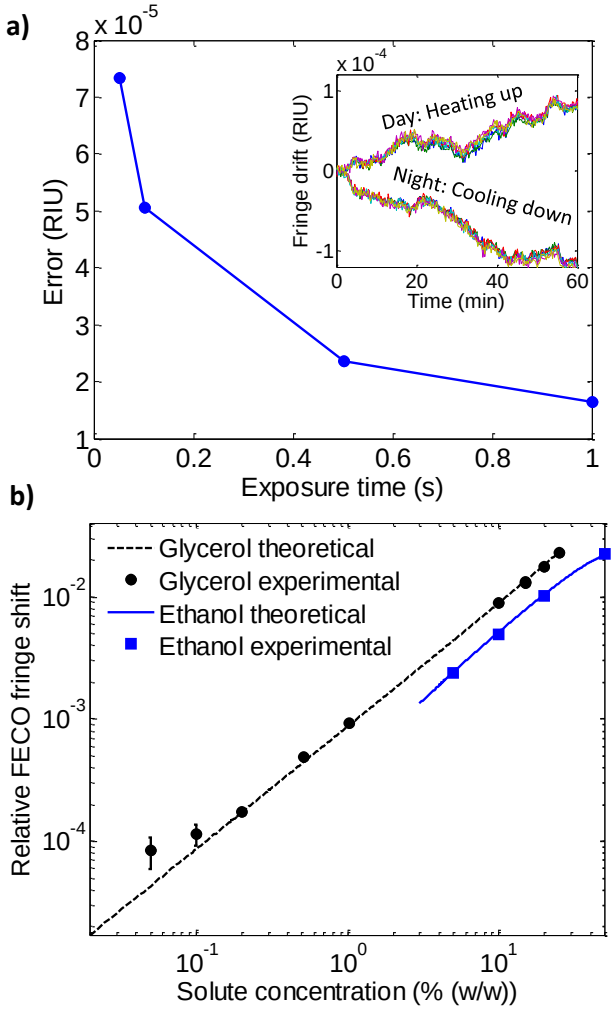

Figure 7.3: (a) Error in refractive index measurement over 30 frames in a rectangular channel with water. Data is expressed as the standard deviation of the average relative fringe shift (averaged over 5 fringes). (Inset) Example drifts in the refractive index measurements of water due to temperature fluctuations. Colors represent 5 different positions across the channel. (b) Experimental fringe shifts when switching from water to solute with a defined concentration compared to theoretical switch predicted with Eqn 4 and refractive index data [254]. Data is expressed as mean $\pm$ SD (n = 20 fringes).

The spatial resolution of the technique depends on the objective. With a 4x objective, the pixel size gives a spatial resolution of 1.91μm. As with all light microscopy applications, the spatial resolution is limited by diffraction, placing a limit of $\sim 1\mu$m on the spatial resolution.

To confirm the accuracy of the technique, fringe positions were tracked while changing the refractive index of a solution in a rectangular channel by switching from pure water to a

homogenous mixture of glycerol or ethanol (Fig. 7.3b). The measured refractive index shift agrees with literature for refractive index shifts greater than that of $0.05\%(w/w)$ glycerol [254]. This is consistent with the previously measured precision (Fig. 7.3a). Furthermore, we studied the reproducibility of the method by measuring the refractive index shift from water to glycerol with three repeat trials per microchip on multiple chips. The error of the measured refractive index shifts between trials on one device and between different devices (2×10^{-5} RIU) is the same as the precision of the technique, indicating excellent reproducibility.

Measurement improvements are possible for both refractive index and temporal resolution. The location of each FECO fringe can be found with higher precision by increasing the resolution of the spectrometer grating or the camera, allowing for a smaller shift in the fringe to be measured. The combination of a faster camera and a brighter light source can improve the temporal resolution of the technique by lowering the required exposure time to detect FECO fringes.

7.4 Measurement of binary diffusion coefficients

We now use the interferometer to monitor the diffusive evolution of chemical gradients. Experimental techniques used to generate and measure the chemical gradients are discussed. A numerical model is then compared to the experimental data to extract binary diffusivities in both free solution and PEG-DA hydrogels.

7.4.1 Experimental design

A microfluidic chip, allowing for the semi-infinite propagation of a diffusive front was fabricated as shown in Fig. 7.4a. PEG-DA hydrogels are used to isolate channels with flow from stagnant channels [234]. The hydrogels allow for the generation of diffusive chemical gradients, by being permeable to diffusive transport but impermeable to convection.

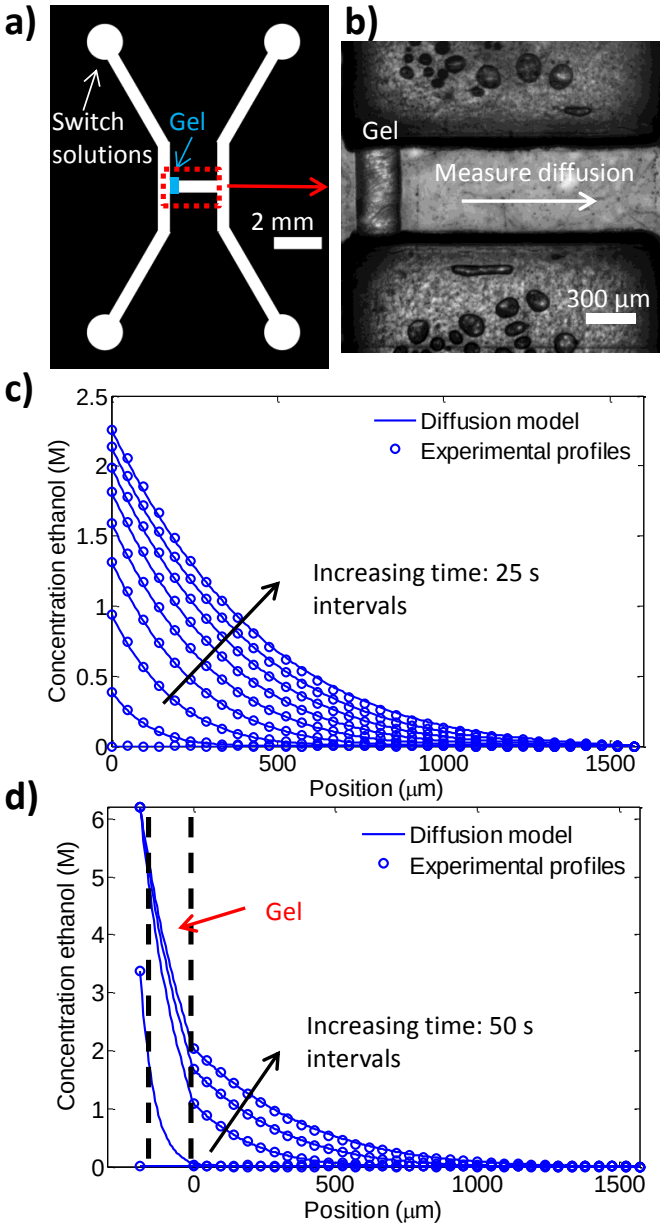

Figure 7.4: (a) Microfluidic channel geometry for diffusivity measurements. (b) Microscopic image of photopolymerized PEG-DA gel and region for diffusivity measurements. (c) Experimentally measured evolution of glycerol diffusive front compared to numerical diffusion model. (d) Extraction of effective diffusivity in PEG-DA hydrogels with numerical model.

The PEG-DA hydrogels were polymerized *in situ* using microscope projection lithography [234]. The aqueous precursor solution consisted of 40% (v/v) PEG-DA-DA 600 (n=400, Polysciences Inc.) and 5% (v/v) photoinitiator (2-hydroxy-2methylpropiophenone, Sigma Aldrich),

and was exposed with 40 mW ultraviolent light through a 500 μm slit with a 10x objective for 500 ms. Here, the width of the PEG-DA hydrogels are much wider than those made by *Paustian et al.*; however, thinner gels could have been fabricated to allow for faster diffusive switching [234].

7.4.2 Diffusivity measurements in water

To measure binary diffusivities in water, the device was initially filled completely with water, and flow to the measurement region was stopped with tubing clamps. By changing inlet tubing, flow to the side channel was switched from water to various solutes at 30% (w/w). After performing the chemical switch, interferometry was used to track the evolution of the chemical gradient (Fig. 7.4b). Images of the interferometry pattern were acquired with 1s exposure time, and FECO fringe displacements were tracked over time to determine the relative shift in refractive index as a function of position. The refractive index shifts were then converted to concentrations using Eqn. 7.4, the known initial concentration, and concentration versus refractive index data [254].

Least squares regression and a numerical diffusion model (Eqn. 7.5) were used to extract diffusivities and their concentration dependence. A linear relationship between concentration and diffusivity was assumed based on the solutes and concentration ranges used in the study (Eqn 7.6) [255, 256, 257, 258, 259, 260].

$$\frac{\partial C(x,t)}{\partial t} = \frac{\partial}{\partial x}\left(D(C(x,t))\frac{\partial C(x,t)}{\partial x}\right) \tag{7.5}$$

$$D(C) = D_0(1 - bC) \tag{7.6}$$

One boundary condition was provided by the measured concentration just outside the hy-

Table 7.1: Literature and experimentally measured binary diffusivity in water D_0, concentration dependent factor b (Eqn. 7.6), and effective diffusivity parameter k in PEG-DA hydrogels (Eqn. 7.7).

	Literature values		Measured values		Measured values
Species	$D_0 \times 10^5$ / (cm^2/s)	b / $(1/M)$	$D_0 \times 10^5$ / (cm^2/s)	b / $(1/M)$	k
Glycerol	0.99 [255]	0.08 [255]	0.90 ± 0.05	0.26 ± 0.07	0.22 ± 0.03
Ethanol	1.24 [256]	0.10 [256]	1.21 ± 0.05	0.12 ± 0.02	0.34 ± 0.02
2-propanol	1.01[257]	0.17[257]	1.04 ± 0.02	0.23 ± 0.02	0.15 ± 0.01
Sucrose	0.52 [258, 259]	0.40 [258, 259]	0.52 ± 0.31	2.4 ± 0.5	0.29 ± 0.02
Glucose	0.67 [260]	0.36 [260]	0.59 ± 0.03	0.8 ± 0.3	0.19 ± 0.02
	w = 0-30% (w/w) T = 298 K		w = 0-10% (w/w) T=296 $\pm$ 1 K		w = 0-30% (w/w) T=296 $\pm$ 1 K

drogel, while the concentration at the far end remained zero during each experiment. Dilute diffusivities (D_0) were extracted at early times of the chemical switch at low concentrations, while the concentration dependence on diffusivity (b) was extracted from the entire time course of the experiment.

The numerical model, with best fit diffusivity values, shows strong agreement with the experimentally measured concentration profiles, as seen for ethanol in Fig. 7.4c. This measurement was repeated at least 5 times, on 2 different microchips, for various solutes, and the best fit values are shown in Table 7.1. The measured values of the dilute diffusivity agree with previously published literature values for all solutes [255, 256, 257, 258, 259, 260]. Measurements of b agree well with literature values for ethanol and 2-propanol [256, 257]; however, they are higher than literature values for glucose, glycerol, and sucrose [258, 260, 255, 259]. In the literature, the diffusion coefficients are measured with very small chemical gradients centered at different concentrations, while we extract the concentration dependence from a single steep chemical gradient. We believe the discrepancy for glucose, glycerol, and sucrose is due to the difference in measurement technique; however, this is still under investigation.

Compared to current diffusivity measurement techniques, our method has many benefits. Small diffusive length scales enable diffusivities to be measured with less than 5% variability in minutes. In addition, because concentration profiles are spatially resolved, subtle effects,

such as diffusivity changes with concentration, can be measured with the technique.

7.4.3 Transport through the PEG-DA hydrogels

Although the FECO fringes are difficult to resolve within the hydrogel, the numerical model can be extended to include transport through the hydrogels. The effective diffusion coefficient in the hydrogel was assumed to be proportional to the free solution diffusion coefficient (with parameter k), independent of concentration:

$$D_{gel}(C) = k \times D_{sol}(C). \tag{7.7}$$

Boundary conditions were measured experimentally and the effective diffusivity in the hydrogel was found with least squares regression. The free solution diffusivity was taken from literature reports (Table 7.1), because concentrations in the gel were much higher than the concentration range in which free solution diffusivities were determined in this study. The numerical model shows strong agreement with the experimental data, as shown for ethanol in Fig. 7.4d. Effective diffusivities within PEG-DA range from 0.15 to 0.35 times the free solution diffusivity for the solutes tested (Table 7.1).

7.5 Evolution of a chemical gradient in a CDC

Multiple transport processes contribute to the development of concentration fields in CDCs. The chemical species must diffuse through both the hydrogels and the CDC to fully develop a steady state concentration profile. Within the gel, the diffusive resistance can vary significantly from free solution due to physical effects, such as size exclusion, or chemical effects, such as partitioning [261]. In addition, the constant diffusion coefficient assumption may fail when working with concentrated solute mixtures. We now use the technique to measure the

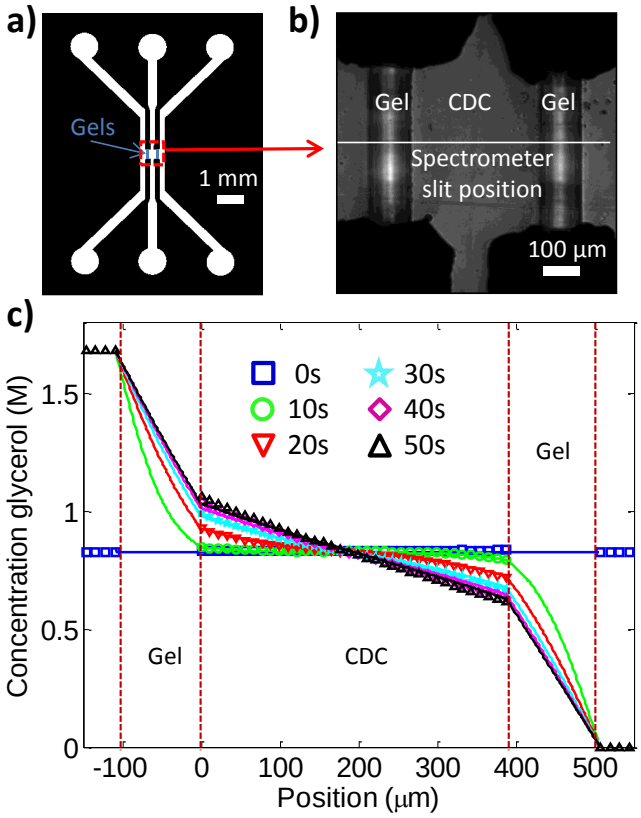

Figure 7.5: (a) Dimensions of microfluidic chip containing CDC and PEG-DA hydrogels. (b) Microscopic image of CDC showing spectrometer slit position. (c) Best fit numerical model using Eqns. 7.5-7.7 (lines) agrees with experimental data (shapes).

generation of a chemical gradient in a CDC directly.

The CDC interferometer consists of three channels, which are connected within a central region, where the CDC is located (Fig. 7.5a). Photopolymerized hydrogels form the CDC (Fig. 7.5b) [234]. For all experiments, all three channels were initially filled with a homogenous solute mixture, with a known concentration. After establishing homogenous conditions throughout the device, flow was stopped to the center CDC channel with external valves. New solute mixtures were flowed through the exterior channels to generate a chemical gradient across the CDC. The chemical switches were performed by manually changing external, inlet tubing.

For the diffusion studies presented here, all three channels were initially filled with an

average solute mixture, and fluids in the two reservoir channels were replaced with pure water and a solution with twice the average concentration, respectively. By initially filling the device with an average solute mixture, the amount of transverse diffusion into the center channel is significantly reduced. In addition, the length scale required for diffusion is halved, reducing the time required to reach steady state by 75%.

FECO interferometry was used to track concentration profiles within the CDC and in the side control channels. The spectrometer slit was positioned perpendicular to the PEG-DA hydrogels in the center of the CDC (Fig. 7.5b), generating fringe patterns similar to those shown in Fig. 7.2a. An example experiment displaying the measurement of gradient generation is shown in Fig. 7.5c. Concentration profiles were not measured within the PEG-DA hydrogels because FECO fringes are not easily resolved.

The 1D diffusion model (Eqns. 7.5-7.7) and diffusivity measurements (Table **??**) were compared to the measured concentration fields in the CDC. The model accurately predicts the evolution of the chemical concentration profile, as demonstrated for glycerol in Fig. 7.5c. Excellent agreement is also observed between the numerical model and experimental data within the CDC for other glycerol concentrations and for the other solutes tested (ethanol, isopropanol, glucose, and sucrose). Based on the diffusivity measurements shown in Table **??**, many features of the steady state profile observed in the CDC (Fig. 7.5c) could have been predicted. First, the concentration drop across the hydrogels is three times greater than the water equivalent due to the lower diffusivity. In addition, the steady state concentration profile is not completely linear due to the concentration dependent diffusivity. Notably, the concentration in the center of the CDC differs slightly from the average concentration of the two side channels.

7.6 Conclusions on technique utility

We have developed a novel interferometry method to measure concentration fields *in situ* in microfluidic devices, without any fluorescent labeling. The technique requires very simple fabrication steps, and it easy to set up using equipment that is standard in many research laboratories. The refractometry method has good spatial and temporal resolutions (1 μm and 50 ms, respectively) with a refractive index sensitivity of 10^{-5} RIU. Here, we have used the technique to quickly measure binary diffusivities with high precision (less than 5 % error), and extract both the concentration dependence on diffusivity and effective diffusivity in PEG-DA hydrogels. The technique was also applied to directly measure the generation of a chemical gradient in a CDC.

Although the ability to resolve changes in refractive index down to 10^{-5} RIU is not new, as other microfluidic interferometry geometries have resolved changes down to 10^{-7} RIU [247], the ability to resolve these changes in both space and time makes the technique a useful and novel tool. We anticipate our technique will prove useful for directly measuring and visualizing spatio-temporal concentration profiles, opening new possibilities for the direct interrogation of materials and systems as they equilibrate, react, dissolve, or crystallize.

Chapter 8

The role of adsorption on transport in PEG-Da hydrogels

Hydrogels are commonly used in drug delivery as particles, drug depots, and tissue scaffolds due to their unique material properties [262, 263]. The high water content of the gels allow for molecules to passively diffuse through the gel while the polymer network provides a solid substrate which can provide structural support. Due to their wide-spread use, there has been considerable research in engineering new hydrogel systems to precisely control the resulting gel structure. To fully take advantage of hydrogel utility, there are also significant efforts on understanding how gel structure and synthesis conditions correlate to functional properties, such as drug release kinetics and gel elasticity.

A common requirement for hydrogels, regardless of the application, is that material must transport through the gel. For example, drugs need to be released from hydrogel particles for therapeutic purposes and nutrients need to be delivered to cells in gel tissue scaffolds. Furthermore, being able to precisely control and predict these transport processes is critical to engineering effective hydrogel systems.

Many previous studies have demonstrated that the diffusion of a species can be predicted

based on the physical properties of the hydrogel, such as polymer molecular weight, cross linking density, and polymer volume fraction [264, 265]. Based on these models, hydrogels can be synthesized with different conditions to change the hydrogel structure and resulting transport properties. However, significantly changing diffusion rates often requires drastic changes in gel structure which can also influence other critical, material properties in a negative manner making it challenging to engineer hydrogels with extended release profiles.

On the contrary, diffusion rates can be significantly slower than predicted given the gel structure, due to interactions between the polymer network and solute. Electrostatic and hydrophobic interactions have shown to increase or decrease the partitioning of solutes in hydrogels and resulting transport rates [266]. For example, diffusion can be significantly hindered for proteins [267, 268, 269, 270, 271] and small molecule therapeutics [272, 273, 274, 270, 271, 275, 276] in neutral and ionizable gels . Futhermore, the chemical structure of a gel can be engineered to interact differently with a solute to control solute partitioning and transport rates [276].

Polyethylene glycol (PEG) is a commonly used polymer in the field of drug delivery due to its ability to resist non-specific protein adsorption resulting in PEG's anti-fouling property [277]. Surprisingly, the transport of solutes in PEG hydrogels can still be influenced due to minor PEG-solute interactions [270, 274]. These interactions can lead to unexpected diffusion rates, impacting the utility of a PEG hydrogel in various drug delivery and/or tissue engineering applications. Here, we demonstrate experimentally that solute adsorption in PEG-Da hydrogels significantly impacts solute transport in both transient and steady state conditions. Sodium dodecyl sulfate (SDS) is used as a model interacting solute because it has shown to interact significantly with PEG in previous studies [278, 279, 280], while butanol is used as a model non-interacting solute.

8.1 Transport in polymeric gels

Various theoretical models have been proposed to describe transport in polymeric gels and solutions [264, 265]. Diffusion depends greatly on the rigidity and density of the polymer chains and the ability for solvent to penetrate the polymeric network. In rubbery polymer systems, the diffusion of species obeys Fickian diffusion. However, in rigid polymer networks, typically below the glass transition temperature (T_g), diffusion of molecules will also depend upon the relaxation of the polymer network. The different regimes for diffusion in polymer networks are often referred to the following based on the relative polymer relaxation time scale (τ_{relax}) and diffusion time scale (τ_{diff}) [265]:

1. Case I: $\tau_{diff} >> \tau_{relax}$, Fickian
2. Case II: $\tau_{diff} << \tau_{relax}$, Non-Fickian
3. Anomalous: $\tau_{diff} \sim \tau_{relax}$, Non-Fickian

Diffusion of aqueous species in hydrogels is typically Fickian because the gels are already hydrated with water. Many models have been proposed which accurately predict the diffusion of species based on the physical properties of the gel and diffusant (gel pore size, water volume fraction, diffusant size, etc.). These models assume that the diffusant only diffuses in water through the gel pores and that the polymer network retards diffusion through various physical mechanisms. The physical models typically estimate the diffusivity based on the free aqueous volume in the gels, increase in hydrodynamic resistance due to the polymer network, obstruction effects due to the polymer network, or a combination of these effects [264]. The majority of these models accurately describe transport in gels with large, water volume fractions and with minimal interactions between diffusant and gel. However, in many material systems, the diffusing species interacts strongly with the gel, significantly impacting transport processes.

A simple, theoretical model is used to describe the transport through a polymeric gel with reversible adsorption. The derivation is similar to the derivation done previously by Liu *et al* [276]. The average, local concentration (C_{total}) is assumed to be a summation of the concentration of species in the gel pores ($C_{free}(1-\phi)$) and the concentration of species adsorbed on the polymer backbone ($C_{ads}\phi$), where ϕ is the volume fraction of the polymer in the gel. The diffusing species is assumed to interact with the polymeric gel with linear adsorption kinetics. The reaction coefficients, k_{on} and k_{off}, are effective bulk rate constants for pore surface adsorption. If the polymer backbone becomes crowded with adsorbing species, a non-linear adsorption model, such as a Langmuir or Freundlich isotherm, may be required to accurately model the adsorption. Surface diffusion along the polymer backbone is neglected, which is valid if the pore diffusive time scale is faster than that of surface diffusion. An effective diffusion coefficient in the gel (D_{gel}) is used, representing the diffusion coefficient of a species which does not adsorb onto the gel. There are many theoretical models which can be used to accurately predict this diffusivity value, typically based on the free volume in the gel or based on hydrodynamic drag from the polymer strands [264].

Mass balances are shown for the free, adsorbed, and total species (Eqns. 8.1 to 8.3):

$$\frac{\partial C_{free}}{\partial t} = D_{gel}\frac{\partial^2 C_{free}}{\partial x^2} - \frac{\phi}{1-\phi}(k_{on}C_{free} - k_{off}C_{ads}) \tag{8.1}$$

$$\frac{\partial C_{ads}}{\partial t} = k_{on}C_{free} - k_{off}C_{ads} \tag{8.2}$$

$$\frac{\partial C_{total}}{\partial t} = (1-\phi)D_{gel}\frac{\partial^2 C_{free}}{\partial x^2} \tag{8.3}$$

Eqns. 8.1 and 8.2 can be non-dimensionalized using the diffusive time scale, leading to Eqns. 8.4 and 8.5, resulting in two dimensionless variables. The equilibrium coefficient (K)

relates the adsorption rate constant to the desorption rate constant, while the Dahmkohler number (Da) relates the time scale for diffusion to that of adsorption (Eqn. 8.6). For a species which significantly adsorbs onto the polymer backbone ($K \geq 1$), three general regimes exist for transport in the hydrogel, depending upon the relative time scales for diffusion and adsorption. This will be discussed in detail in the next section.

$$\frac{\partial \tilde{C_{free}}}{\partial \tilde{t}} = \frac{\partial^2 \tilde{C_{free}}}{\partial \tilde{x}^2} - Da\frac{\phi}{1-\phi}(\tilde{C_{free}} - \tilde{C_{ads}}) \tag{8.4}$$

$$\frac{\partial \tilde{C_{ads}}}{\partial \tilde{t}} = \frac{Da}{K}(\tilde{C_{free}} - \tilde{C_{ads}}) \tag{8.5}$$

$$K = \frac{k_{on}}{k_{off}} \qquad Da = \frac{L^2 k_{on}}{D_{gel}} \tag{8.6}$$

8.2 Experimental and computational methods

Experimental methods

Microfluidic interferometry was used to measure the transport of solutes in PEG-Da hydrogels (Fig. 8.1). A Fabry-Perot microfluidic device was fabricated with modification from a previous study [2]. Glass slides were coated with a semi-reflective coating of Ag/Ti (50/5 nm) with electron-beam deposition, and holes were drilled into the glass slides with a drill. A microfluidic channel design was cut into photoresist film (KOLON KS-8730, $\sim 30\mu m$ thick) using a laser cutter, and the film was then bonded to one glass slide at 120 ^{o}C for 1 min. The film was sandwiched between another glass slide and baked at 120 ^{o}C for 8 min. PDMS inlet cubes and the top glass slide were treated with UV ozone for at least 5 min., and then the cubes were bonded to the glass slide in the oven at 120 ^{o}C for at least 10 min. After bonding, the photoresist film was further cured in a UV microwave for 4.5 min.

PEG-Da hydrogels were synthesized *in situ* between two channels as previously reported [234]. Briefly, an aqueous precursor solution containing PEG-Da 400 (33, 40, 50, or 60 vol. %) and 2-Hydroxy-2-methylpropiophenone (3 vol. %) was flowed into the microfluidic device. After stopping flow, the precursor was polymerized with an inverted microscope by exposing a region in the channel to UV light (30 mW, 1 s) through a slit positioned in the shutter (400 or 800 μm wide) with a 4x objective. A representative gel is shown in Fig. 8.1b. After polymerizing the gel, both channels were flushed with DI water for at least 15 min to remove the precursor, and the gel was soaked in water for at least 1 d after polymerization to remove any leftover reactant.

FECO interferferometry was used to measure the refractive index along a line in the microfluidic device [2]. For each experiment, the device was positioned so the spectrometer slit was centered on the hydrogel (Fig. 8.1b). FECO fringes were observed both in the aqueous solution and within the PEG-Da hydrogel (Fig. 8.1c). Fringes were not resolved at the edges of the hydrogel because of the abrupt change in refractive index; therefore, this region of the gel was not used in any analysis.

To measure the diffusivity of a solute, the device was initially filled with DI water. The inlet and outlet of the large channel on the top and the outlet of the thin channel (Fig. 8.1b) were submerged in a reservoir to ensure no flow in the large channel. The solution in the thin channel was switched from DI water to solute using a pressure source to provide flow, and images of the FECO fringes were taken every 1 s. Refractive index profiles ($n(x,t)$) were then extracted by tracking the relative shift in the FECO fringes at each position over time using a MATLAB algorithm described previously [2].

Theory of diffusion measurement

Using the microfluidic device setup described previously, there are two general ways in which an effective gel diffusivity can be measured. A chemical can be allowed to propagate

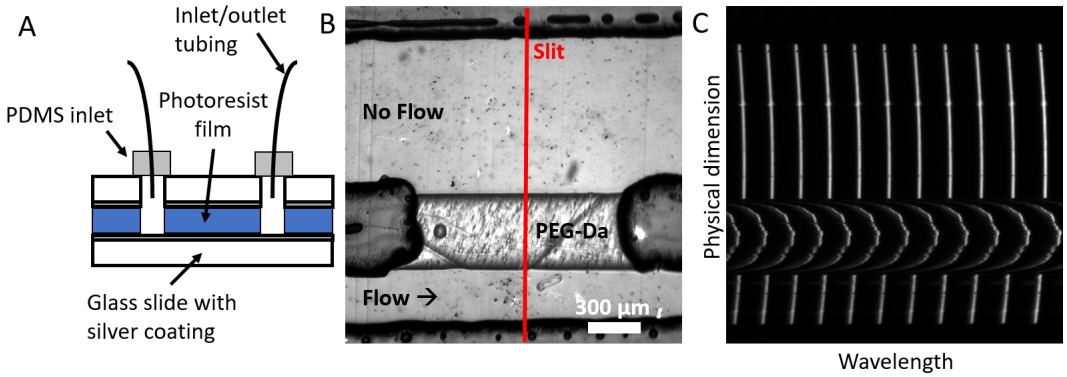

Figure 8.1: (a) Cartoon schematic of Fabry-Perot, microfluidic device (side view) (b) Representative image of microfluidic channel with PEG-Da hydrogel polymerized *in situ* (c) FECO fringes used to track the diffusion of solute into the PEG hydrogel corresponding to the device shown in (b)

through a gel, and the transient concentration profiles inside the gel can be fit to a numerical diffusion model (Fig. 8.2a). The best fit diffusivity, D_{eff}, will be used to describe the transient diffusivity for a propagating species. On the contrary, a quasi steady state gradient can be established across a thin hydrogel slab, and the flux through the gel can be measured to determine an effective steady state diffusivity, commonly referred to as the permeability (P) (Fig. 8.2b) [281]. Here, the flux through the membrane is determined by measuring the concentration profile in the solution at the edge of the hydrogel. The permeability (P) is then calculated by relating the flux to the concentration drop across the membrane and the membrane thickness.

Depending upon the relative time scale for diffusion and adsorption, the measured transient diffusivity and permeability (D_{eff} and P) will mean qualitatively different things (Table 8.1). If diffusion is significantly slower than adsorption ($Da >> K$), then quasi equilibrium can be assumed throughout the gel and Eqn. 8.3 simplifies to:

$$\frac{\partial C_{total}}{\partial t} = \frac{1-\phi}{1-\phi+K\phi} D_{gel} \frac{\partial^2 C_{free}}{\partial x^2} \tag{8.7}$$

In this case, the transient diffusion coefficient will be less than the permeability. On the

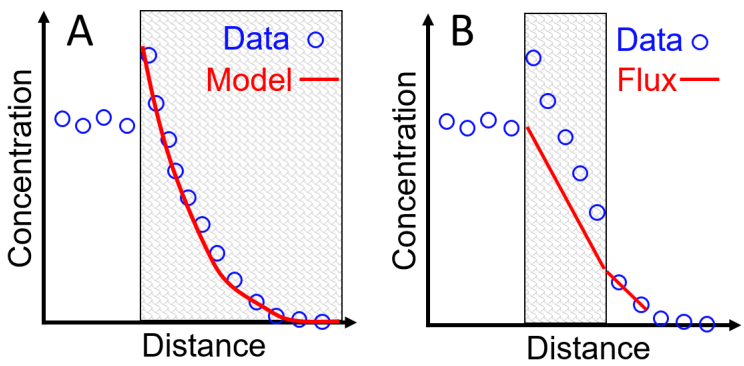

Figure 8.2: Differences in diffusion technique.

contrary, if adsorption is slow compared to diffusion ($Da << 1$), then the species will diffuse through the gel without adsorbing at short time scales and both the transient and permeability values will be measured with similar values. If diffusion and adsorption have similar time scales, the concentration profiles inside the gel will not look strictly diffusive, and a best fit diffusion value will lie between the two extremes just discussed.

Table 8.1: Measured diffusivity values in hydrogels with adsorption (Assuming $K > 1$)

$Da >> K$	$1 < Da < K$	$Da << 1$
$D_{eff} \approx \frac{1-\phi}{1-\phi+K\phi} D_{gel}$	$\frac{1-\phi}{1-\phi+K\phi} D_{gel} < D_{eff} < (1-\phi) D_{gel}$	$D_{eff} \approx (1-\phi) D_{gel}$
$P = (1-\phi) D_{gel}$	$P = (1-\phi) D_{gel}$	$P = (1-\phi) D_{gel}$

8.3 Transient diffusivity measurements in PEG-Da hydrogels

To measure the transient diffusivity, a PEG-Da hydrogel was polymerized as shown in Fig 8.3a. The solution flowing in the left channel was switched from DI water to a solution with the solute of interest (7 mM SDS, 5 wt. % butanol, or 7 mM DTAB). The refractive index of the gel was assumed to change linearly with the concentration of diffusing solute, which is valid for dilute solutes [254]. A 1D numerical diffusion model was then fit to the refractive index profiles inside the gel after switching solutions, and least squared regression was used to calculate the best fit diffusivity for each experiment (Fig. 8.3b-c). The outer 10 % of the gel was not used during the fitting process due to the heterogeneity of the gel on the edges. The numerical diffusion models fit the refractive index profile qualitatively well for both butanol and SDS.

PEG-Da hydrogels were then polymerized with different volume fractions of PEG-Da in the precursor solution (33, 44, 50, and 60 vol %). The final volume fraction of the polymer in the hydrogel was assumed to be identical to the initial volume fraction of polymer in the precursor. This approximation should hold becuase the equilbrium water content is similar to the water content in the precursor solution for hydrogels made with low molecular weight PEG-Da oligomers (< 600 Da) at these polymer compositions[282]. In addition, no gel swelling was observed in the microscope after synthesizing the hydrogels; however, it is expected that higher molecular weight PEG-Da gels would swell and bulge at the sides.

The effective gel diffusivities of SDS and butanol decreases with increasing PEG-Da compositions. Based on free volume theory [281], the diffusivity of a solute should scale exponentially with the negative, inverse of the hydration (H) of a polymeric gel. The hydration (H) is

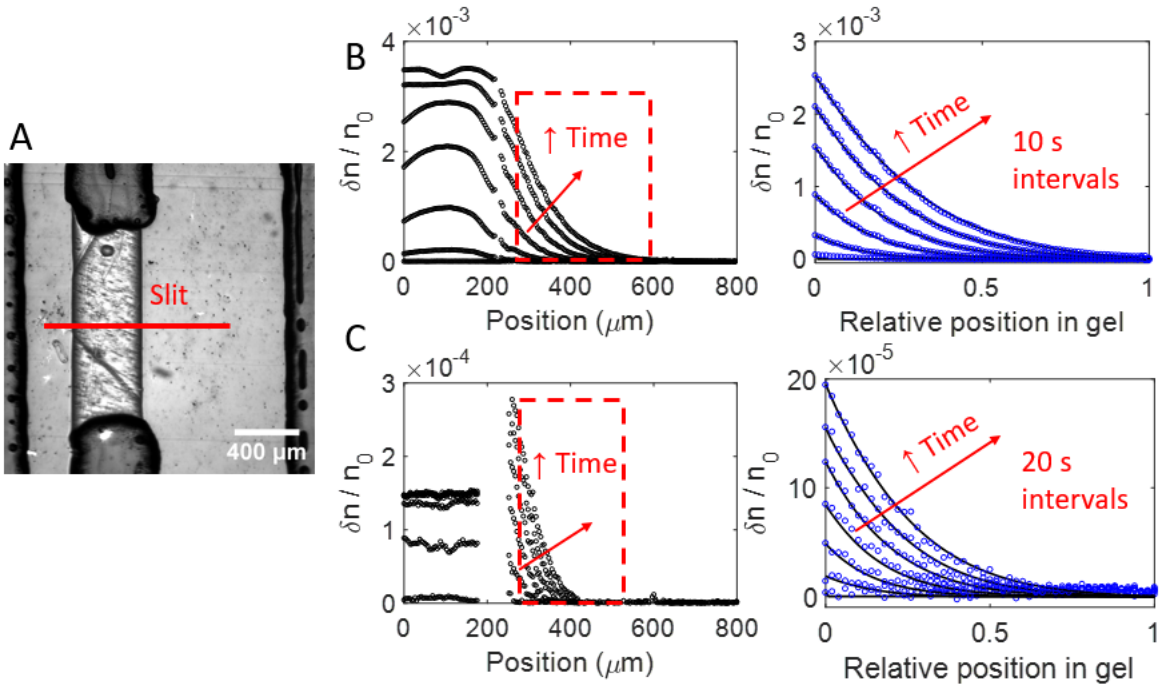

Figure 8.3: Example refractive index profiles to determine transient diffusivity. (a) Image of PEG-Da (33 %) hydrogel with spectrometer slit position. (b) Refractive index profile after switching solution from DI water to 5 wt. % butanol. Experimental data is compared to 1D numerical diffusion model within the hydrogel. (c) Refractive index profile after switching solution from DI water to 7 mM SDS. Experimental data is compared to 1D numerical diffusion model within the hydrogel.

defined as the final volume fraction of water in the gel.

$$D_{eff} \quad \alpha \quad \exp(-1/H) \qquad \text{where} \quad H = 1 - \phi \tag{8.8}$$

The effective diffusivities for butanol and SDS in hydrogels made with 33, 40, and 50 vol. % PEG-Da obey the simple free volume theory (Fig. 8.4). The diffusivity for both butanol and SDS are higher at 60 vol. % than predicted by the theory. For butanol, the free volume theory is able to accurately predict the diffusivity of butanol in pure water (H = 1); however, the theory under predicts the diffusivity of SDS in pure water by 1 order of magnitude. This discrepency is believed to be due to interactions between the PEG and SDS, which is further measured in

permeability measurements.

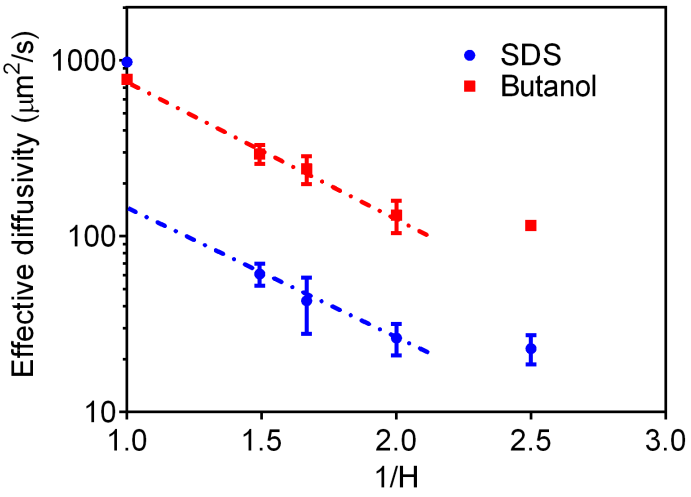

Figure 8.4: Transient diffusivity of butanol and SDS as a function of inverse hydration (1/H)

8.4 Permeability measurements in PEG-Da hydrogels

The quasi steady flux through a PEG-Da membrane was measured to determine hydrogel permeability (P). To ensure a large flux which can be accurately detected with interferometry and a short time required to reach quasi steady state, the hydrogels were crosslinked to be half as thick as the gels used to measure the transient diffusivity (Fig. 8.5a). The concentration drop across the PEG-Da membrane was measured with the difference in refractive index across the gel, and the flux through the gel was measured using the slope in refractive index on the side of the gel with no flow (Fig. 8.5b-c). While the refractive index could be measured in the hydrogel, a direct correlation between the refractive index and concentration is unknown, making it more convenient to measure the flux through the hydrogel membrane with the external

concentrations in solutions. Summarizing, the permeability was calculated with:

$$P = \frac{Flux}{\Delta C_{gel}/\Delta x_{gel}} = \frac{(\frac{\Delta n}{\Delta x})_{sol}}{(\frac{\Delta n}{\Delta x})_{ext}} D_{sol} \tag{8.9}$$

where $(\frac{\Delta n}{\Delta x})_{ext}$ is the slope in refractive index drop across the gel and $(\frac{\Delta n}{\Delta x})_{sol}$ is the slope in refractive index in solution at the edge of the hydrogel.

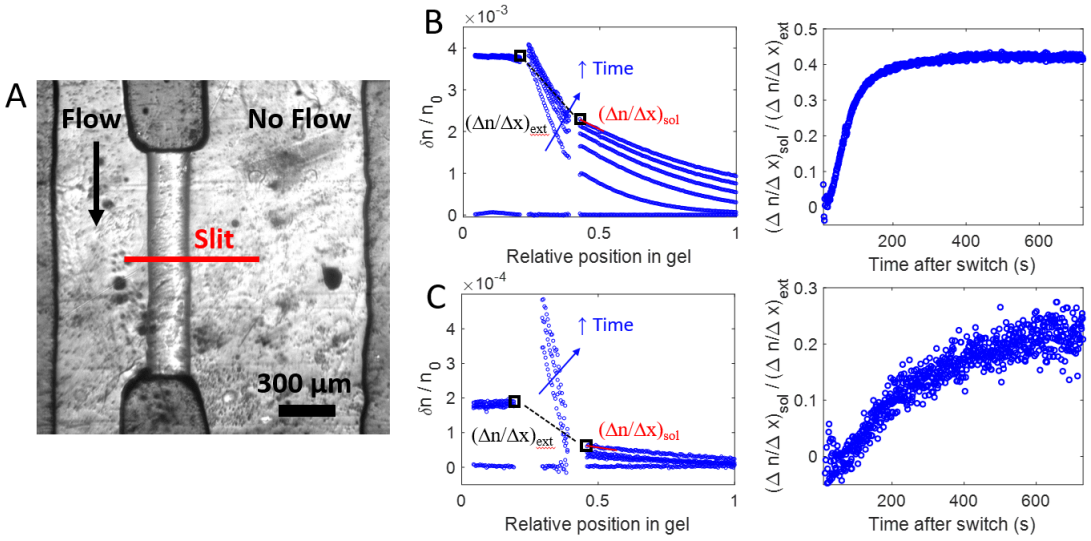

Figure 8.5: (a) Microscope image of device used to measure PEG-Da permeability. (b) Representative refractive index profiles in device after flowing 5 wt. % butanol (100 s between each curve). (c) Representative refractive index profiles in device after flowing 7 mM SDS (200 s between each curve)

The permeability was then calculated by averaging the ratio of refractive index slopes between 650 to 700 s after switching solutions. A quasi steady state concentration gradient is required to accurately calculate the permeability using the flux through the hydrogel membrane, and the effective gel diffusivities suggest this should be achieved within $\sim$ 75 s and $\sim$ 350 s for butanol and SDS, respectively. Consistent with these time scales, the ratio of refractive index slope across the hydrogel compared to in solution is approximately constant after flowing butanol and SDS for 100 s and 400 s, respectively (Fig 8.5b-c). In addition, the refractive index profile inside of the hydrogels is linear after these time points, further validating the quasi state

assumption.

Permeability and transient diffusivity values are compared for butanol, SDS, and DTAB in Table 8.2. While the transient diffusivity and permeability are approximately the same for butanol, the permeability is approximately 4x and 2x higher than the effective transient diffusivity for SDS and DTAB, respectively. The large discrepancy between the permeability and diffusivity for SDS is expected given that SDS interacts strongly with PEG. It is likely that DTAB also interacts with PEG in a similar manner.

Using the simple adsorption model summarized in Table 8.1, the gel partition coefficient ($P_{g,w}$) and an effective equilibrium constant (K) can be calculated for each species assuming quasi equilibrium adsorption-desorption in the gel ($Da >> K$):

$$P_{gw} = P/D_{eff} \quad \text{and} \quad K = (P_{gw} + \phi - 1)/\phi \tag{8.10}$$

Given the differences in permeability and diffusivity for SDS and DTAB, both SDS and DTAB have relatively high, effective equilibrium constants ($K = 10$ and $K = 3.5$, respectively). On the contrary, the permeability and diffusivity measurements seem to indicate that butanol does not interact as strongly with the PEG-Da gels ($K = 0.83$).

Table 8.2: Measured diffusivity values in PEG-Da hydrogels ($\phi = 0.33$)

	Diffusivity values ($\mu m^2/s$)			Extracted values	
Species	Solution ($D_{solution}$)	Transient (D_{eff})	Permeability (P)	Equilibrium constant (K)	Partition coeff ($P_{g,w}$)
Butanol	780	293 ± 47	277 ± 39	0.83	0.95
SDS	980	61 ± 11	250 ± 61	10.4	4.09
DTAB	880	137	250 ± 29	3.5	1.8

Permeabilities were measured for SDS and butanol at different PEG-Da volume fractions, and compared to the transient diffusivity values measured previously (Fig. 8.6). At each gel composition, the permeability is 3.5 to 5 times faster than the transient diffusivity for SDS. The

estimated effective equilibrium constants are 10.4, 8.0, 9.2, and 6.4 for the 33, 40, 50, and 60 vol. % gels, respectively. On the contrary, the transient diffusivity is approximately the same as the permeability for butanol within all of the hydrogels.

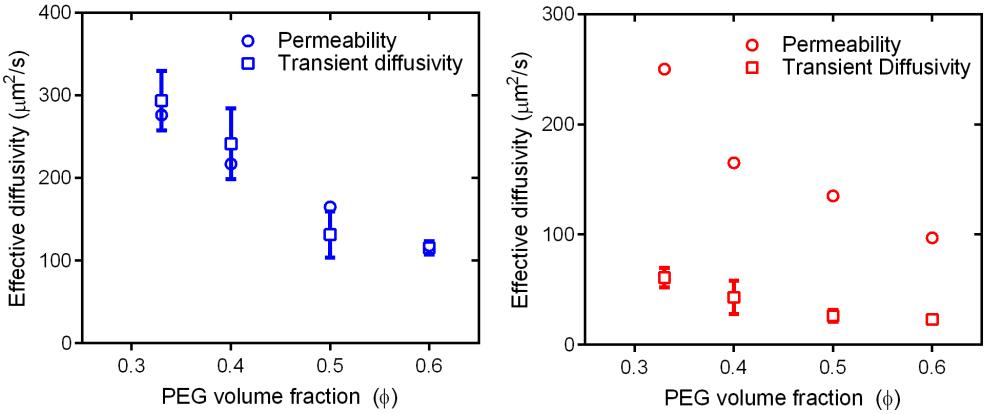

Figure 8.6: Transient diffusivity and permeability values for (a) 5 wt. % butanol and (b) 7 mM SDS in PEG-Da gels as a function of PEG-Da volume fractions. Data represents mean ±95% confidence intervals.

To further validate that SDS partitions into PEG-Da hydrogels, macroscopic PEG-Da gels ($\phi = 0.33$) were synthesized in a UV microwave using a PDMS template to control the size of the disks. The PEG-Da disks were soaked in 3.5 and 7 mM SDS solutions for 2 days. After soaking, the concentration of SDS in the solution outside of the gels was measured using a spectrophotometric technique described previously [283]. By performing a mass balance, the partition coefficient of SDS in the hydrogel could be calculated. Relatively consistent with the transport studies, the partition coefficients (P_{gw}) for 3.5 and 7 mM SDS were determined to be 3.1 ± 0.5 and 3.2 ± 0.2, respectively.

8.5 Loading and unloading PEG-Da posts

To this point, quasi-equilibrium has been assumed in the hydrogels for butanol, SDS, and DTAB to estimate an effective, gel equilibrium constant. The refractive index profiles fit the diffusion equation well when extracting transient diffusivities, giving evidence that quasi-equilibrium is a valid assumption. The quasi-equilbrium assumption can be further validated by looking at the loading and unloading of solute from a hydrogel post. This experiment is done under flow, to ensure minimal external mass transport resistance.

For solutes which partition heavily into the hydrogel ($K >> 1$), the time required to fill a hydrogel post with solute can be significantly less than the time required to unload the same hydrogel post, if equilibrium is never established. If the adsorption time scale is significantly slower than that of diffusion ($Da << K$), it can take a factor of K longer to unload a hydrogel post which was loaded with solute but not in equilibrium with the external solution.

For demonstration, PEG-Da hydrogel posts ($\phi = 0.33$) were loaded with solute by flowing solutions with SDS (7 mM) and butanol (5 wt. %) past the post for 700 s (Fig. 8.7a). After flowing the solutions, water was flowed past the posts to unload the posts. For both butanol and SDS, the time required to load and unload the hydrogel posts is approximately the same (Fig. 8.7b-c), giving further evidence that the gels were at equilibrium with their external solutions.

8.6 Discussion on transport in PEG-Da hydrogels

Understanding solute transport in hydrogels is critical for designing effective gels for various applications. Many theoretical models can accurately describe transport in gels based on the physical structure of the gel and diffusant; however, the majority of these models fail to accurately predict transport in gels with significant solute-gel interactions. Furthermore, while simple physical models can be used to understand how these interactions impact transport

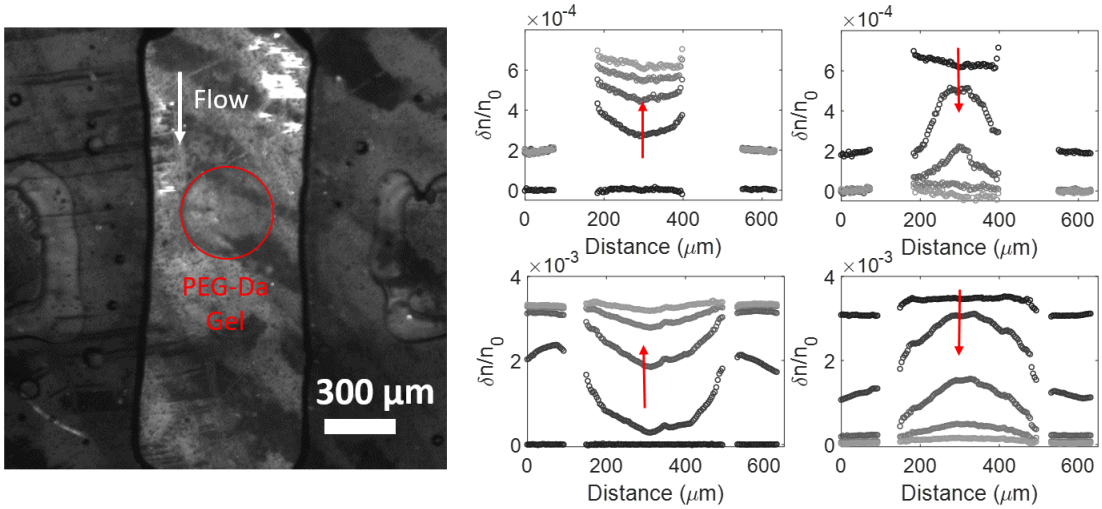

Figure 8.7: (a) Microscope image of device used to load up cylindrical PEG-Da post. (b) Experimental refractive index profile of 7 mM SDS loading (left) and unloading (right) a PEG hydrogel post (175 s in between each profile). (c) Experimental refractive index profile of 5 wt. % butanol loading (left) and unloading (right) a PEG hydrogel post (30 s in between each profile).

properties, few experimental techniques exist to measure these properties directly. For example, current experimental techniques rely on measuring the transport of fluorescent solutes, with techniques such as fluorescence recovery after photobleaching (FRAP) or fluorescence correlation spectroscopy (FCS), or by measuring self diffusivity values with NMR techniques. In addition, many studies have extracted effective gel diffusivity and permeability values by measuring the external concentration of solute in reservoirs which are exposed to hydrogels, but these techniques are time consuming and do not directly track solute transport in the gels.

Here, a microfluidic, interferometric technique was used to directly measure non-fluorescent solute transport in hydrogels. The technique is capable of measuring effective gel diffusivity, gel permeability, and gel loading/unloading time scales simply by changing the geometry of the hydrogel in the microfluidic channel. A simple adsorption-diffusion model predicts how solute-gel interactions impact these transport properties. Specifically, the relative rate of diffusion to adsorption/desorption determines the impact of these interactions on solute transport.

Due to their wide-spread use, PEG hydrogels are used as a model system to demonstrate the impact of gel-solute interactions on transport.

PEG hydrogels are commonly used in the field of drug delivery due to their ability to resist protein adsorption, and they are generally believed to be relatively inert to solutes. By measuring the transient and steady state transport of solute in PEG hydrogels, we demonstrate that certain solutes do interact with PEG and, as a result, transport is significantly impacted. The effective diffusivity of butanol in PEG-Da hydrogels obeyed simple free volume theory, consistent with previous reports for NaCl in PEG-Da gels[282]. On the contrary, SDS diffusivity values in PEG-Da gels were an order of magnitude lower than expected given free volume theory.

There is a large difference between the permeability and diffusivity for SDS and DTAB; however, the values are approximately the same for butanol. The large difference in the permeability and transient diffusivity measurements for SDS and DTAB, suggest that surfactant interactions with PEG are responsible for the slow diffusion rate. Gel equilbrium constants (and partition coefficients) are estimated based on the permeability and transient diffusivity measurements. Both SDS and DTAB interact strongly with the PEG gel (K = 10 and 3.5, respectively), while butanol did not interact strongly (K = 0.85). The partitioning of SDS into the hydrogels was verified by also measuring the external concentration of SDS solutions which were soaked in macroscopic PEG-Da gels.

Previous diffusion measurements in charged HEMA/MAA hydrogels, show that drug transport is significantly impacted by specific drug-gel interactions [276]. Here, we show that a similar phenomena occurs in neutral PEG-Da hydrogels with the surfactants SDS and DTAB. While the transport of these surfactants in PEG gels are likely not of interest for the majority of PEG gel applications, specific interaction between PEG-solute interactions are going to present in other physical systems impacting transport.

The large difference in permeability and transient diffusivity for solutes which interact

strongly with gels, significantly impacts the performance of a gel. For example, the time required for a nutrient to reach a cell encapsulated in a hydrogel can take a factor of $K\phi$ longer than expected without any solute-gel interactions; however once the nutrient reaches the cell, the flux of the nutrient to the cell will remain constant regardless of the gel-solute interactions. Furthermore, as a delivery vehicle, both the quantity of drug loading and time scale for release are impacted by solute-gel interactions. Favorable gel-solute interactions can increase drug loading and release time scale by a factor of $K\phi$. In the specific case where diffusion is much faster than adsorption/desorption ($Da << 1$) for strongly associating solutes, it can take a factor of K longer to release drug loaded hydrogel particles than it does to load the particles, impacting particle design.

Overall, hydrogels are a useful tool in drug delivery and in other material systems due to their ability to allow for fast solute transport. Solute-specific interactions with gels impact transport rates, and, therefore, hydrogel function as demonstrated with PEG gels here. It is critical that the effect of gel-solute interactions are measured experimentally and accurately accounted for in physical models to ensure gels are engineered to function properly in a given application.

Chapter 9

Conclusions and future directions

Advancements in drug delivery have the potential to significantly improve the treatment of many diseases; however, designing an effective delivery system requires overcoming many biologic, material, and engineering challenges which has resulted in few approved clinical products. For the field to continue to progress, a focus needs to be placed on developing clinically feasible delivery platforms. Furthermore, more fundamental studies need to address how to optimize the physio-chemical properties of these delivery vehicles to most effectively release their drug payloads and interact with their intended biological systems.

This thesis has focused primarily on developing delivery systems for the treatment of breast cancer. Specifically, clinically relevant delivery vehicles were designed to carry synergistic combinations of FDA approved chemotherapeutic agents. Release kinetics of drugs were optimized to increase the efficiency of delivery vehicles by improving drug-drug interactions. In addition, a new microfluidic tool was developed to study drug release in hydrogel-based delivery systems, for future delivery vehicle development.

9.1 Identification of synergistic drug pairs with *in vitro* assays

Using a combination of therapeutics is commonly employed in the clinic for various diseases based on the methodology that targeting multiple pathways can more efficiently target the disease state. In oncology, doctors are constantly trying new chemotherapeutic combinations to treat late stage cancers which are unresponsive to standard treatment regimes. Because mono-chemotherapy is limited by toxicity at higher doses, combination chemotherapy is only an effective treatment option if a lower combination drug dose can be administered to achieve a greater reduction in tumor burden. The identification of synergistic drug pairs with non-overlapping mechanisms of toxicity can help solve this problem.

Many *in vitro* studies have shown that drug synergy is extremely sensitive to specific parameters, such as drug dose and drug ratio; however, an often overlooked parameter impacting drug synergy is the schedule in which the cells are exposed to the drugs. In my dissertation, I have shown that synergy between many of the commonly used chemotherapeutic agents is significantly impacted by drug scheduling on various breast cancer cell lines. Using the Chou-Talalay synergy method, I have identified synergistic drug schedules for different breast cancer cell lines. I have studied in detail synergy between GEM and DOX on triple negative breast cancer cells (MDA-MB-231) and between LAP and PTX on HER2+ breast cancer cells (BT-474). For both drug pairs, I have shown that bolus scheduling of the drugs impacts how effective the pair is at inhibiting tumor growth *in vitro*.

Using the Chou-Talalay method, giving GEM prior to DOX was found to be more effective than other administration schedules *in vitro*. Furthermore, the cells were found to undergo significantly more apoptosis when exposed to these drugs in the optimal sequence. The cell cycle distribution of the cells gave insight into why the cells seemed to be more prone to DOX-induced toxicity after exposure to GEM. From the *in vitro* studies alone, it was clear that drug

schedule significantly impacts how effective the GEM/DOX combination is at inhibiting tumor growth.

The combination of GEM and DOX was also effective at inhibiting tumor growth *in vivo*; however, surprisingly, the administration sequence of the drugs did not play a significant role in efficacy. While the discrepancy between the impact of administration schedule on *in vitro* and *in vivo* tumor reduction requires further evaluation, there are multiple observations that may explain these discrepancies. First, cells are known to behave differently *in vitro* compared to an *in vivo* environment. For example, while GEM had a significantly higher IC_{50} than DOX *in vitro*, GEM was more effective at inhibiting tumor growth *in vivo*. In addition, due to fast clearance of small molecules, the cells *in vivo* are exposed to different concentrations of drug which may not produce the same synergistic effects. For example, GEM has an extremely short half life in mouse plasma due to rapid deamination, resulting in lower cumulative drug exposure than tested in *in vitro* studies.

In spite of the discrepancy in schedule dependency of GEM and DOX between *in vitro* and *in vivo* assays, the drug pair was much more effective than the single drugs *in vivo*. Furthermore, the drug pair was effective at inhibiting tumor growth at low drug doses, which did not cause any observable signs of toxicity. The *in vitro* identification of synergy between GEM and DOX led to a drug pair which performed favorably *in vivo*; however, it is clear that the optimization done *in vitro* did not translate to *in vivo*.

Moving forward, it is believed that identification of drug synergy is a critical tool in picking effective drug combinations. It is also evident that the sequence in which cancer cells are exposed to chemotherapeutic agents *in vitro* significantly impacts how effective the drugs are at inhibiting cell growth. However, more sophisticated *in vitro* models are required to accurately predict *in vivo* activity. For example, spheroid cultures which more accurately represent the tumor microenvironment and realistic drug exposure profiles will assist in creating more predictive *in vitro* models. Furthermore, synergy needs to be evaluated on patient derived tumor

cells, due to the large degree of heterogeneity from patient to patient. Synergy should also not be viewed as static and be reevaluated throughout the course of treatment, due to the rapid development of drug resistance.

Unfortunately, many drug pairs which were identified as synergistic *in vitro* still fail to result in any improvement in clinical efficacy. Because drug pairs are often administered based on optimized mono-chemotherapy dosing regimes, it is not surprising that it is difficult to translate synergistic drug pairs from the bench top to the patient. Adjusting chemotherapeutic dosing schedules and ranges based on drug-drug interactions should improve combination chemotherapy in many cases. Furthermore, the development of new delivery vehicles carrying precise combinations of therapeutic agents, should improve the ability to translate drug pairs from the lab to the clinic.

9.2 Design of synergistic delivery vehicles

The development of drug delivery systems carrying multiple chemotherapeutics has grown significantly in the past decade, in hopes of combining the potential therapeutic benefits of combination chemotherapy and nanoparticulate delivery systems. It is a synthetic and engineering challenge to synthesize a delivery vehicle capable of carrying multiple drugs due to the large differences in physiochemical properties of various drugs. Furthermore, there are many design parameters which impact therapeutic efficacy, including delivery vehicle physical properties, drug ratio, and drug release rates. While many studies have shown the ability to incorporate multiple drugs into a single delivery vehicle, few have studied how design parameters impact the efficacy of the vehicle and drug-drug interactions.

Combining multiple chemotherapy drugs into a single delivery vehicle is only advantageous, if the drugs work favorably together. As just discussed, administration schedule significantly impacts the synergy between the two drugs. In my dissertation, I have engineered

delivery vehicles which can be optimized by changing the release rate of drugs from the delivery vehicle. Drug pairs, which demonstrate a strong dependence between synergy and drug schedule, were loaded into polymer drug conjugates and bi-phasic nanoparticles. The synthetic techniques of the delivery vehicles allows for the relative release rate of each vehicle to be changed without significantly changing the delivery system.

HA based conjugates were synthesized with DOX and GEM. Based on which chemical linker the drugs were conjugated to HA with, the relative release kinetics could be changed without changing the physical structure of the vehicle. HA conjugates which released GEM faster than DOX were synergistic at inhibiting cancer cell growth *in vitro*, as predicted with free drug scheduling studies. Furthermore, the dual drug HA conjugates were much more effective at inhibiting tumor growth *in vivo* than the single drug conjugates.

Similarly, bi-phasic nanoparticles, consisting of PLGA and acDEX, were synthesized with EHD co-jetting and loaded with LAP and PTX. The compartments degrade and release their therapeutic payloads at different rates, depending on the composition of the polymer, and LAP and PTX could be loaded into different compartments simply by changing the jetting conditions. The toxicity of the bi-phasic particles on cancer cells *in vitro* was highly dependent upon which compartment the drugs were loaded into the particles, demonstrating the importance of drug release kinetics.

While both delivery platforms were optimized to deliver a defined drug pair to treat a specific breast cancer cell line, the same platforms can be applied to treat additional cancers with other synergistic drug pairs. The ability to maintain the physical structure of the vehicle, while manipulating which drugs are incorporated, the ratio in which these drugs are combined, and the relative drug release kinetics, provide a framework to optimize drug interactions for any given disease. Furthermore, these studies motivate the future development of delivery systems capable of controlling the temporal release of multiple therapeutics with higher precision. Both passive and externally stimulated release mechanisms are anticipated to play a role in future

development.

It is evident that nanomedicine will play a critical role in the future of combination chemotherapy; however, the future success is highly dependent upon the collaboration of material scientists, chemists, biologists, and clinicians. Future research needs to focus both on gaining a better fundamental understanding how these complicated material systems interact with biological systems and how to develop clinically feasible delivery platforms. Both gaining a better understanding of how the material properties of the carrier impact vehicle internalization and biodistribution *in vivo* and how drug incorporation impacts the efficacy of the vehicle are necessary to develop effective vehicles. Furthermore, developing simple delivery systems, utilizing materials which are already approved for clinical use and scalable synthetic techniques, will help streamline the process of future clinical translation.

9.3 Clinical translation of hyaluronic acid drug conjugates

Given the high failure rate of single drug loaded vehicles in the clinic, it is not surprising that few dual loaded drug nanomedicines have been evaluated in clinical trials. However, the recent success of the dual drug loaded liposome Vyxeos in treating acute myeloid leukemia (AML) in phase III clinical trials, provides evidence that multi-drug incorporation has the potential to transform future therapies. Unfortunately, incorporating multiple drugs into a single delivery vehicle is challenging and results in complicated synthetic routes, making it difficult to overcome the stringent regulatory approval process required for such multi-functional and multi-drug incorporated systems. In spite of these challenges, it is believed that the HA-DOX-GEM conjugates developed in this dissertation warrant further investigation as a potential clinical product due to the simple synthetic steps, effectiveness in an aggressive pre-clinical cancer model, and the potential to treat other cancers.

The synthesis of HA based drug conjugates require basic chemical steps which can easily

be scaled up by pharmaceutical companies. Compared to liposomes and polymeric nanoparticles, polymer drug conjugates require more traditional synthetic steps. In addition, after the final vehicle is synthesized, the polymer drug conjugates can be stored as a lyophilized powder, increasing the shelf life compared to liposomes which must remain hydrated. However, prior to translation, more research is required to gain better control of the final physical structure of the vehicle. For example, while conjugation of GEM to HA does not seem to have any impact on vehicle structure, conjugation of hydrophobic drugs, such as DOX, can lead to both vehicle self assembly and aggregation, which needs to be better understood and controlled for future translation.

Regardless of the ability to synthesize a reproducible product, clinical activity ultimately determines the success of a given therapeutic. HA based drug conjugates have previously shown efficacy in preclinical models, and, here, we show that HA-DOX-GEM is effective at treating an aggressive, orthotopic, 4T1 tumor model. Due to synergy between DOX and GEM, low drug doses can be administered leading to tumor growth inhibition with no observable signs of toxicity. Interestingly, HA-DOX-GEM is able to treat the cancer systemically both though intravenous and subcutaneous drug administration. Current research is underway to understand the distribution of drug and HA carrier through each administration route. Contrary to HPMA-based drug conjugates, HA drug conjugates can be degraded in various tissues throughout the body due to the high abundance of hyaluronidases, allowing for the exploration of different drug administration routes. Future research will need to identify the most optimal way to deliver HA-conjugates based on target disease pathology in more sophisticated *in vivo* cancer models.

HA-based drug conjugates are a broad delivery platform that has the potential to treat cancers with very different pathologies. The overexpression of CD-44, the receptor for HA, in many cancers, warrants the exploration of HA as a drug carrier in different cancers. Furthermore, because HA can be administered through various parenteral administration routes, it can

be used to treat cancers locally and metastastes that have spread throughout the body. The future application of HA-based drug conjugates requires collaboration with oncologists, which can help identity the best application for the technology.

9.4 Development of tools to measure release kinetics

In addition to developing more effective dual-drug loaded systems for treating advanced cancers, this thesis has developed a broad experimental technique capable of studying how delivery vehicle release therapeutic payloads. By understanding the mechanisms in which drugs are released from polymeric systems, drug release rates can be optimized in any given material system. As discussed in Chapters 5 and 6, drug release kinetics can significantly impact the therapeutic activity of a drug delivery system. Therefore, to engineer therapeutically effective delivery vehicles, drug release mechanisms need to be well characterized.

Many simple, physical models can accurately describe the passive release of therapeutics from polymeric systems. These models rely on predicting polymer degradation rates, drug linker hydrolysis rates, drug transport rates in polymeric systems, or a combination of these mechanisms. However, due to specific polymer-drug interactions, drug release cannot be predicted accurately *a priori* in many polymer systems and must be measured experimentally. Typically, drug release is measured macroscopically with dialysis experiments. While these experiments often give an accurate measurement of the time scale for drug release, they fail to measure drug release rates with high temporal resolution, making it difficult to understand the physical mechanisms responsible for drug release rates.

Here, I have developed and characterized a microfluidic technique capable of measuring solute concentration fields with high temporal and spatial resolution. The technique measures solution refractive index, and is therefore not limited to measuring fluorescent or UV-active species, making it broadly applicable to almost all drugs. The utility of the technique

was demonstrated by the ability to detect subtle changes in solute diffusivity with concentration, which required accurately measuring solute concentration in a channel with high spatio-temporal resolution. While this experiment did not measure drug release from a polymeric carrier, manipulation of microfludic channel geometry can allow for experiments to be designed to study drug release or polymer degradation rates.

The technique was then used to study the transport of solute in PEG hydrogels, which are are commonly used in drug delivery as drug carriers, cell scaffolds, and drug depots. Interestingly, the diffusion of a few ionic surfactants in PEG gels is slower than predicted with traditional gel transport models. By measuring solute transport rate in and out of the gels, gel-solute interactions are hypothesized to be responsible for differences in transport rates. These specific interactions significantly impact the time scale for drug release and drug loading capacity, which both were effectively measured using the new, microfluidic technique.

While the exact physical system studied here is not applicable to most drug delivery applications, drug-polymer interactions will be present in many drug delivery systems. These interactions will significantly impact drug release rates and resulting therapeutic activity, and, thus, need to be well characterized for the successful engineering of polymeric carriers. The ability to measure transport and drug release rates with high temporal resolution was demonstrated here, and it enabled a better fundamental understanding of the mechanisms responsible for solute release.

The future success of drug delivery is not only dependent up on the development of novel delivery systems, but also gaining a more fundamental understanding how current delivery systems interact with their biological targets and therapeutics. Currently, there are few experimental techniques capable of probing how drugs interact with and release from polymeric systems. The development of more novel, experimental techniques, capable of measuring drug release with high temporal resolution, will allow for delivery systems to be engineered to be more effective. These techniques will lead to both new delivery systems and to new theoretical

models capable of accurately predicting drug release in specific systems.

Bibliography

[1] BIO, *Clinical development success rates 2006-2015*, Tech. Rep. June, 2016.

[2] D. R. Vogus, V. Mansard, M. V. Rapp, and T. M. Squires, *Measuring concentration fields in microfluidic channels in situ with a FabryPerot interferometer*, *Lab Chip* **15** (2015), no. 7 1689–1696.

[3] R. Siegel, D. Naishadham, and A. Jemal, *Cancer statistics, 2013.*, *CA: a cancer journal for clinicians* **63** (jan, 2013) 11–30.

[4] R. L. Siegel, K. D. Miller, and A. Jemal, *Cancer statistics*, *CA Cancer J Clin* **66** (2016), no. 1 7–30.

[5] D. Hanahan and R. A. Weinberg, *The Hallmarks of Cancer*, *Cell* **100** (jan, 2000) 57–70.

[6] G. I. Evan and K. H. Vousden, *Proliferation, cell cycle and apoptosis in cancer.*, *Nature* **411** (may, 2001) 342–8.

[7] C. Holohan, S. Van Schaeybroeck, D. B. Longley, and P. G. Johnston, *Cancer drug resistance: an evolving paradigm.*, *Nature Reviews Cancer* **13** (oct, 2013) 714–26.

[8] M. M. Gottesman, T. Fojo, and S. E. Bates, *Multidrug resistance in cancer: role of ATP-dependent transporters.*, *Nature Reviews Cancer* **2** (2002), no. 1 48–58.

[9] R. W. Johnstone, A. A. Ruefli, and S. W. Lowe, *Apoptosis: A link between cancer genetics and chemotherapy*, *Cell* **108** (2002), no. 2 153–164.

[10] G. Bianchini, J. M. Balko, I. A. Mayer, M. E. Sanders, and L. Gianni, *Triple-negative breast cancer: challenges and opportunities of a heterogeneous disease.*, *Nature reviews. Clinical oncology* **13** (2016), no. 11 674–690.

[11] D. P. Ryan, T. S. Hong, and N. Bardeesy, *Pancreatic Adenocarcinoma*, *New England Journal of Medicine* **371** (sep, 2014) 1039–1049.

[12] R. Iacovelli, F. Pietrantonio, C. Maggi, F. de Braud, and M. Di Bartolomeo, *Combination or single-agent chemotherapy as adjuvant treatment of gastric cancer. A systematic review and meta-analysis of published trials.*, *Critical Reviews in Oncology/Hematology* **98** (2016) 24–28.

[13] J. Saultz and R. Garzon, *Acute Myeloid Leukemia: A Concise Review*, *Journal of Clinical Medicine* **5** (2016), no. 33.

[14] R. Thota, J. M. Pauff, and J. D. Berlin, *Treatment of metastatic pancreatic adenocarcinoma: a review.*, *Oncology (Williston Park, N.Y.)* **28** (2014), no. 1 70–4.

[15] S. Carrick, S. Parker, C. E. Thornton, D. Ghersi, J. Simes, and N. Wilcken, *Single agent versus combination chemotherapy for metastatic breast cancer.*, *Cochrane database of systematic reviews* (jan, 2009).

[16] B. Al-Lazikani, U. Banerji, and P. Workman, *Combinatorial drug therapy for cancer in the post-genomic era.*, *Nature biotechnology* **30** (jul, 2012) 679–92.

[17] V. T. Devita, R. C. Young, and G. P. Canellos, *Combination versus single agent chemotherapy: A review of the basis for selection of drug treatment of cancer*, *Cancer* **35** (jan, 1975) 98–110.

[18] R. J. Tallarida, *Drug Synergism: Its Detection and Applications*, *Journal of Pharmacology and Experimental Therapeutics* **298** (sep, 2001) 865–872.

[19] M. C. Berenbaum, *What is synergy?*, *Pharmacological reviews* **41** (jun, 1989) 93–141.

[20] W. Greco, G. Bravo, and J. Parsons, *The search for synergy: a critical review from a response surface perspective*, *Pharmacological reviews* **47** (jun, 1995) 331–385.

[21] T. Chou, *Theoretical basis, experimental design, and computerized simulation of synergism and antagonism in drug combination studies*, *Pharmacological reviews* (2006).

[22] M. C. Berenbaum, *Synergy, additivism and antagonism in immunosuppression. A critical review.*, *Clinical and experimental immunology* **28** (apr, 1977) 1–18.

[23] T. C. Chou, *Drug combination studies and their synergy quantification using the Chou-Talalay method.*, *Cancer research* **70** (jan, 2010) 440–6.

[24] H. Gurney, *How to calculate the dose of chemotherapy.*, *British journal of cancer* **86** (apr, 2002) 1297–302.

[25] A. Felici, J. Verweij, and A. Sparreboom, *Dosing strategies for anticancer drugs: the good, the bad and body-surface area*, *European Journal of Cancer* **38** (sep, 2002) 1677–1684.

[26] K. Vermeulen, D. R. Van Bockstaele, and Z. N. Berneman, *The cell cycle: a review of regulation, deregulation and therapeutic targets in cancer*, *Cell Proliferation* **36** (jun, 2003) 131–149.

[27] G. H. Williams and K. Stoeber, *The cell cycle and cancer.*, *The Journal of pathology* **226** (jan, 2012) 352–64.

[28] L. Galluzzi, I. Vitale, J. M. Abrams, E. S. Alnemri, E. H. Baehrecke, M. V. Blagosklonny, T. M. Dawson, V. L. Dawson, W. S. El-Deiry, S. Fulda, E. Gottlieb, D. R. Green, M. O. Hengartner, O. Kepp, R. A. Knight, S. Kumar, S. A. Lipton, X. Lu, F. Madeo, W. Malorni, P. Mehlen, G. Nuñez, M. E. Peter, M. Piacentini, D. C. Rubinsztein, Y. Shi, H.-U. Simon, P. Vandenabeele, E. White, J. Yuan, B. Zhivotovsky, G. Melino, and G. Kroemer, *Molecular definitions of cell death subroutines: recommendations of the Nomenclature Committee on Cell Death 2012.*, *Cell death and differentiation* **19** (jan, 2012) 107–20.

[29] M. V. Jain, A. M. Paczulla, T. Klonisch, F. N. Dimgba, S. B. Rao, K. Roberg, F. Schweizer, C. Lengerke, P. Davoodpour, V. R. Palicharla, S. Maddika, and M. Łos, *Interconnections between apoptotic, autophagic and necrotic pathways: implications for cancer therapy development.*, *Journal of cellular and molecular medicine* **17** (jan, 2013) 12–29.

[30] J. M. Gump and A. Thorburn, *Autophagy and apoptosis: what is the connection?*, *Trends in cell biology* **21** (jul, 2011) 387–92.

[31] S. N. Gardner, *A mechanistic, predictive model of dose-response curves for cell cycle phase-specific and -nonspecific drugs.*, *Cancer research* **60** (mar, 2000) 1417–25.

[32] M. J. Lee, A. S. Ye, A. K. Gardino, A. M. Heijink, P. K. Sorger, G. MacBeath, and M. B. Yaffe, *Sequential application of anticancer drugs enhances cell death by rewiring apoptotic signaling networks.*, *Cell* **149** (may, 2012) 780–94.

[33] S. T. Yu, T. M. Chen, S. Y. Tseng, and Y. H. Chen, *Tryptanthrin inhibits MDR1 and reverses doxorubicin resistance in breast cancer cells*, *Biochemical and Biophysical Research Communications* **358** (2007), no. 1 79–84.

[34] O. Fardel, V. Lecureur, S. Daval, A. Corlu, and A. Guillouzo, *Up-regulation of P-glycoprotein expression in rat liver cells by acute doxorubicin treatment.*, *The FEBS journal* **246** (1997), no. 1 186–192.

[35] A. Abolhoda, A. E. Wilson, H. Ross, P. V. Danenberg, M. Burt, and K. W. Scotto, *Rapid activation of MDR1 gene expression in human metastatic sarcoma after in vivo exposure to doxorubicin.*, *Clinical cancer research : an official journal of the American Association for Cancer Research* **5** (1999), no. 11 3352–3356.

[36] P. M. Chaudhary and I. B. Roninson, *Induction of multidrug resistance in human cells by transient exposure to different chemotherapeutic drugs.*, *Journal of the National Cancer Institute* **85** (1993), no. 8 632–639.

[37] G. M. Lai, Y. N. Chen, L. A. Mickley, A. T. Fojo, and S. E. Bates, *P-glycoprotein expression and schedule dependence of adriamycin cytotoxicity in human colon carcinoma cell lines.*, *International journal of cancer* **49** (1991), no. 5 696–703.

[38] A. A. Cohen, N. Geva-Zatorsky, E. Eden, M. Frenkel-Morgenstern, I. Issaeva, A. Sigal, R. Milo, C. Cohen-Saidon, Y. Liron, Z. Kam, L. Cohen, T. Danon, N. Perzov, and U. Alon, *Dynamic proteomics of individual cancer cells in response to a drug.*, *Science* **322** (dec, 2008) 1511–6.

[39] D. Amadori, G. L. Frassineti, W. Zoli, C. Milandri, A. Tienghi, A. Ravaioli, A. Gentile, and E. Salzano, *A phase I/II study of sequential doxorubicin and paclitaxel in the treatment of advanced breast cancer.*, *Seminars in oncology* **23** (oct, 1996) 16–22.

[40] T. C. Chou, G. M. Otter, and F. M. Sirotnak, *Schedule-dependent synergism of taxol or taxotere with edatrexate against human breast cancer cells in vitro.*, *Cancer chemotherapy and pharmacology* **37** (jan, 1996) 222–8.

[41] E. A. Perez, F. M. Hack, L. M. Webber, and T. C. Chou, *Schedule-dependent synergism of edatrexate and cisplatin in combination in the A549 lung-cancer cell line as assessed by median-effect analysis.*, *Cancer chemotherapy and pharmacology* **33** (jan, 1993) 245–50.

[42] C. Oliveras-Ferraros, A. Vazquez-Martin, R. Colomer, R. De Llorens, J. Brunet, and J. A. Menendez, *Sequence-dependent synergism and antagonism between paclitaxel and gemcitabine in breast cancer cells: the importance of scheduling.*, *International journal of oncology* **32** (2008) 113–120.

[43] R. Tanaka, H. Ariyama, B. Qin, Y. Takii, E. Baba, K. Mitsugi, M. Harada, and S. Nakano, *In vitro schedule-dependent interaction between paclitaxel and oxaliplatin in human cancer cell lines.*, *Cancer chemotherapy and pharmacology* **55** (jun, 2005) 595–601.

[44] H. Cheng, S. An, X. Zhang, and S. Dong, *In vitro sequence-dependent synergism between paclitaxel and gefitinib in human lung cancer cell lines*, *Cancer chemotherapy and pharmacology* **67** (2011) 637–646.

[45] N. Takahashi, W. Li, D. Banerjee, Y. Guan, Y. Wada-Takahashi, M. F. Brennan, T.-C. Chou, K. W. Scotto, and J. R. Bertino, *Sequence-dependent synergistic cytotoxicity of ecteinascidin-743 and paclitaxel in human breast cancer cell lines in vitro and in vivo.*, *Cancer research* **62** (dec, 2002) 6909–15.

[46] D. R. Budman, A. Calabro, L. G. Wang, X. M. Liu, L. Stiel, L. M. Adams, and W. Kreis, *Synergism of cytotoxic effects of vinorelbine and paclitaxel in vitro.*, *Cancer investigation* **18** (jan, 2000) 695–701.

[47] Y. Kano, M. Akutsu, S. Tsunoda, M. Furuta, Y. Yazawa, and J. Ando, *Schedule-dependent synergism and antagonism between paclitaxel and methotrexate in human carcinoma cell lines.*, *Oncology research* **10** (jan, 1998) 347–54.

[48] L. A. McHugh, M. Kriajevska, J. K. Mellon, and T. R. Griffiths, *Combined treatment of bladder cancer cell lines with lapatinib and varying chemotherapy regimens–evidence of schedule-dependent synergy.*, *Urology* **69** (feb, 2007) 390–4.

[49] Y. Barenholz, *Doxil®–the first FDA-approved nano-drug: lessons learned.*, *Journal of Controlled Release* **160** (jun, 2012) 117–34.

[50] A. Wicki, D. Witzigmann, V. Balasubramanian, and J. Huwyler, *Nanomedicine in Cancer Therapy: Challenges, Opportunities, and Clinical Applications*, *Journal of Controlled Release* **200** (dec, 2014) 138–157.

[51] Z. Amoozgar and Y. Yeo, *Recent advances in stealth coating of nanoparticle drug delivery systems*, *Wiley Interdisciplinary Reviews: Nanomedicine and Nanobiotechnology* **4** (2012), no. 2 219–233.

[52] P. Decuzzi, B. Godin, T. Tanaka, S. Y. Lee, C. Chiappini, X. Liu, and M. Ferrari, *Size and shape effects in the biodistribution of intravascularly injected particles*, *Journal of Controlled Release* **141** (2010), no. 3 320–327.

[53] A. C. Anselmo, M. Zhang, S. Kumar, D. R. Vogus, S. Menegatti, M. E. Helgeson, and S. Mitragotri, *Elasticity of nanoparticles influences their blood circulation, phagocytosis, endocytosis, and targeting*, *ACS Nano* **9** (2015), no. 3 3169–3177.

[54] H. Maeda, J. Wu, T. Sawa, Y. Matsumura, and K. Hori, *Tumor vascular permeability and the EPR effect in macromolecular therapeutics: A review*, *Journal of Controlled Release* **65** (2000), no. 1 271–284.

[55] H. Maeda, H. Nakamura, and J. Fang, *The EPR effect for macromolecular drug delivery to solid tumors: Improvement of tumor uptake, lowering of systemic toxicity, and distinct tumor imaging in vivo*, *Advanced Drug Delivery Reviews* **65** (2013), no. 1 71–79.

[56] Y. Matsumura and H. Maeda, *A new concept for macromolecular therapeutics in cnacer chemotherapy: mechanism of tumoritropic accumulation of proteins and the antitumor agents Smancs*, *Cancer research* **46** (1986) 6387– 6392.

[57] S. Wilhelm, A. J. Tavares, Q. Dai, S. Ohta, J. Audet, H. F. Dvorak, and W. C. W. Chan, *Analysis of nanoparticle delivery to tumours*, *Nature Reviews Materials* **1** (2016), no. 5 16014.

[58] F. Danhier, *To exploit the tumor microenvironment: Since the EPR effect fails in the clinic, what is the future of nanomedicine?*, *Journal of Controlled Release* **244** (2016) 108–121.

[59] P. Polakis, *Antibody Drug Conjugates for Cancer Therapy.*, *Pharmacological reviews* **68** (2016) 3–19.

[60] J.-W. Yoo, N. Doshi, and S. Mitragotri, *Adaptive micro and nanoparticles: temporal control over carrier properties to facilitate drug delivery.*, *Advanced drug delivery reviews* **63** (nov, 2011) 1247–56.

[61] R. van der Meel, T. Lammers, and W. E. Hennink, *Cancer nanomedicines: oversold or underappreciated?*, *Expert Opinion on Drug Delivery* **14** (2017), no. 1 1–5.

[62] R. X. Zhang, H. L. Wong, H. Y. Xue, J. Y. Eoh, and X. Y. Wu, *Nanomedicine of synergistic drug combinations for cancer therapy-strategies and perspectives*, *Journal of Controlled Release* **240** (2016) 489–503.

[63] Q. Hu, W. Sun, C. Wang, and Z. Gu, *Recent advances of cocktail chemotherapy by combination drug delivery systems*, *Advanced Drug Delivery Reviews* **98** (2016) 19–34.

[64] C.-M. J. Hu and L. Zhang, *Nanoparticle-based combination therapy toward overcoming drug resistance in cancer.*, *Biochemical pharmacology* **83** (apr, 2012) 1104–11.

[65] S. Sengupta, D. Eavarone, I. Capila, G. Zhao, N. Watson, T. Kiziltepe, and R. Sasisekharan, *Temporal targeting of tumour cells and neovasculature with a nanoscale delivery system.*, *Nature* **436** (jul, 2005) 568–72.

[66] Z. J. Deng, S. W. Morton, E. Ben-Akiva, E. C. Dreaden, K. E. Shopsowitz, and P. T. Hammond, *Layer-by-layer nanoparticles for systemic codelivery of an anticancer drug and siRNA for potential triple-negative breast cancer treatment.*, *ACS nano* **7** (dec, 2013) 9571–84.

[67] Z. Wang and P. C. Ho, *A nanocapsular combinatorial sequential drug delivery system for antiangiogenesis and anticancer activities.*, *Biomaterials* **31** (sep, 2010) 7115–23.

[68] S. W. Morton, M. J. Lee, Z. J. Deng, E. C. Dreaden, E. Siouve, K. E. Shopsowitz, N. J. Shah, M. B. Yaffe, P. T. Hammond, M. L. Mcmaster, S. Y. Kristinsson, I. Turesson, M. Bjorkholm, O. Landgren, S. W. Morton, M. J. Lee, Z. J. Deng, E. C. Dreaden, E. Siouve, K. E. Shopsowitz, N. J. Shah, M. B. Yaffe, and P. T. Hammond, *A Nanoparticle-Based Combination Chemotherapy Delivery System for Enhanced Tumor Killing by Dynamic Rewiring of Signaling Pathways*, *Science signaling* **7** (may, 2014) ra44.

[69] Y. He, Z. Su, L. Xue, H. Xu, and C. Zhang, *Co-delivery of erlotinib and doxorubicin by pH-sensitive charge conversion nanocarrier for synergistic therapy*, *Journal of Controlled Release* **229** (2016) 80–=92.

[70] R. H. Wilson, R. Plummer, J. Adam, M. M. Eatock, A. V. Boddy, M. Griffin, R. Miller, Y. Matsumura, T. Shimizu, and H. Calvert, *Phase I and pharmacokinetic study of NC-6004, a new platinum entity of cisplatin-conjugated polymer forming micelles*, *Journal of Clinical Oncology* **26** (may, 2008) 2573.

[71] D. J. Whellan, S. J. Ellis, W. E. Kraus, K. Hawthorne, I. L. Piña, S. J. Keteyian, D. W. Kitzman, L. Cooper, K. Lee, and C. M. O'Connor, *Phase II studies of polymer-doxorubicin (PK1, FCE28068) in the treatment of breast, lung and colorectal cancer*, *Annals of Internal Medicine* **151** (2009), no. 6 414–420.

[72] G. J. Weiss, J. Chao, J. D. Neidhart, R. K. Ramanathan, D. Bassett, J. A. Neidhart, C. H. J. Choi, W. Chow, V. Chung, S. J. Forman, E. Garmey, J. Hwang, D. L. Kalinoski, M. Koczywas, J. Longmate, R. J. Melton, R. Morgan, J. Oliver, J. J. Peterkin, J. L. Ryan, T. Schluep, T. W. Synold, P. Twardowski, M. E. Davis, and Y. Yen, *First-in-human phase 1/2a trial of CRLX101, a cyclodextrin-containing polymer-camptothecin nanopharmaceutical in patients with advanced solid tumor malignancies*, *Investigational New Drugs* **31** (2013), no. 4 986–1000.

[73] P. A. Vasey, S. B. Kaye, R. Morrison, C. Twelves, P. Wilson, R. Duncan, A. H. Thomson, L. S. Murray, T. E. Hilditch, T. Murray, S. Burtles, D. Fraier, and E. Frigerio, *Phase I Clinical and Pharmacokinetic Study of PK1 [N-(2-Hydroxypropyl) methacrylamide Copolymer Doxorubicin]: First Member of a New Class of Chemotherapeutic*, *Clinical Cancer Research* **5** (1999), no. January 83–94.

[74] M. E. O'Brien, M. A. Socinski, A. Y. Popovich, I. N. Bondarenko, A. Tomova, B. T. Bilynsky, Y. S. Hotko, V. L. Ganul, I. Y. Kostinsky, A. J. Eisenfeld, L. Sandalic, F. B. Oldham, B. Bandstra, A. B. Sandler, and J. W. Singer, *Randomized Phase III Trial Comparing Single-Agent Paclitaxel Poliglumex (CT-2103, PPX) with Single-Agent Gemcitabine or Vinorelbine for the Treatment of PS 2 Patients with Chemotherapy-Naïve Advanced Non-small Cell Lung Cancer*, *Journal of Thoracic Oncology* **3** (2008), no. 7 728–734.

[75] D. P. Nowotnik and E. Cvitkovic, *ProLindac (AP5346): A review of the development of an HPMA DACH platinum Polymer Therapeutic*, *Advanced Drug Delivery Reviews* **61** (2009), no. 13 1214–1219.

[76] H. Ringsdorf, *Structure and properties of pharmacologically active polymers*, *Journal of Polymer Science: Polymer Symposia* **51** (1975), no. 1 135–153.

[77] R. Duncan, *Polymer conjugates as anticancer nanomedicines.*, *Nature reviews. Cancer* **6** (sep, 2006) 688–701.

[78] J. Kopeček, *Polymer-drug conjugates: Origins, progress to date and future directions*, *Advanced Drug Delivery Reviews* **65** (2013), no. 1 49–59.

[79] Q. Feng and R. Tong, *Anticancer nanoparticulate polymer-drug conjugate*, *Bioengineering & Translational Medicine* (2016), no. June 1–20.

[80] F. Dosio, S. Arpicco, B. Stella, and E. Fattal, *Hyaluronic acid for anticancer drug and nucleic acid delivery*, *Advanced Drug Delivery Reviews* **97** (2015) 204–236.

[81] D. Dheer, D. Arora, S. Jaglan, R. K. Rawal, and R. Shankar, *Polysaccharides Based Nanomaterials for Targeted Anti-cancer Drug Delivery.*, *Journal of drug targeting* **25** (2017), no. 1 1–16.

[82] A. Basu, K. R. Kunduru, E. Abtew, and A. J. Domb, *Polysaccharide based conjugates for biomedical applications*, *Bioconjugate Chemistry* **26** (2015), no. 8 1396–1412.

[83] J.-G. Shiah, M. Dvoák, P. Kopečková, Y. Sun, C. M. Peterson, and J. Kopeček, *Biodistribution and antitumour efficacy of long-circulating N-(2-hydroxypropyl)methacrylamide copolymer-doxorubicin conjugates in nude mice*, *European Journal of Cancer* **37** (mar, 2001) 131–139.

[84] L. W. Seymour, Y. Miyamoto, H. Maeda, M. Brereton, J. Strohalm, K. Ulbrich, and R. Duncan, *Influence of molecular weight on passive tumour accumulation of a soluble macromolecular drug carrier*, *European Journal of Cancer* **31** (1995), no. 5 766–770.

[85] K. Ulbrich and V. Šubr, *Structural and chemical aspects of HPMA copolymers as drug carriers*, *Advanced Drug Delivery Reviews* **62** (2010), no. 2 150–166.

[86] J. Kopeček and P. Kopečková, *HPMA copolymers: Origins, early developments, present, and future*, *Advanced Drug Delivery Reviews* **62** (2010), no. 2 122–149.

[87] M. Pechar, K. Ulbrich, V. Šubr, L. W. Seymour, and E. H. Schacht, *Poly(ethylene glycol) multiblock copolymer as a carrier of anti-cancer drug doxorubicin*, *Bioconjugate Chemistry* **11** (2000), no. 2 131–139.

[88] J. M. Meerum Terwogt, W. W. ten Bokkel Huinink, J. H. Schellens, M. Schot, I. A. Mandjes, M. G. Zurlo, M. Rocchetti, H. Rosing, F. J. Koopman, and J. H. Beijnen, *Phase I clinical and pharmacokinetic study of PNU166945, a novel water-soluble polymer-conjugated prodrug of paclitaxel.*, *Anti-cancer drugs* **12** (apr, 2001) 315–323.

[89] D. Bissett, J. Cassidy, J. S. de Bono, F. Muirhead, M. Main, L. Robson, D. Fraier, M. L. Magne, C. Pellizzoni, M. G. Porro, R. Spinelli, W. Speed, and C. Twelves, *Phase I and pharmacokinetic (PK) study of MAG-CPT (PNU 166148): a polymeric derivative of camptothecin (CPT)*, *British Journal of Cancer* **91** (2004), no. 1 50–55.

[90] J. W. Hopewel, R. Duncan, D. Wilding, and K. Chakrabarti, *Preclinical evaluation of the cardiotoxicity of PK2: a novel HPMA copolymer-doxorubicin-galactosamine conjugate antitumour agent.*, *Human & experimental toxicology* **20** (2001), no. 9 461–70.

[91] D. P. Nowotnik, *AP5346 (ProLindac), a dach platinum polymer conjugate in Phase II trials against ovarian cancer*, *Current Bioactive Compounds* **7** (2011), no. 1 21–26.

[92] S. Danhauser-Riedl, E. Hausmann, H. D. Schick, R. Bender, H. Dietzfelbinger, J. Rastetter, and A. R. Hanauske, *Phase I clinical and pharmacokinetic trial of dextran conjugated doxorubicin (AD-70, DOX-OXD).*, *Investigational new drugs* **11** (1993), no. 2-3 187–195.

[93] O. Soepenberg, M. J. A. de Jonge, A. Sparreboom, P. de Bruin, F. A. L. M. Eskens, G. de Heus, J. Wanders, P. Cheverton, M. P. Ducharme, and J. Verweij, *Phase I and pharmacokinetic study of DE-310 in patients with advanced solid tumors.*, *Clinical cancer research : an official journal of the American Association for Cancer Research* **11** (2005), no. 2 703–711.

[94] S. A. Veltkamp, E. O. Witteveen, A. Capriati, A. Crea, F. Animati, M. Voogel-Fuchs, I. J. G. M. Van Den Heuvel, J. H. Beijnen, E. E. Voest, and J. H. M. Schellens, *Clinical and pharmacologic study of the novel prodrug delimotecan (MEN 4901/T-0128) in patients with solid tumors*, *Clinical Cancer Research* **14** (2008), no. 22 7535–7544.

[95] P. F. Bassi, A. Volpe, D. D'Agostino, G. Palermo, D. Renier, S. Franchini, A. Rosato, and M. Racioppi, *Paclitaxel-hyaluronic acid for intravesical therapy of bacillus calmette-gurin refractory carcinoma in situ of the bladder: Results of a phase i study*, *Journal of Urology* **185** (2011), no. 2 445–449.

[96] K. Knop, R. Hoogenboom, D. Fischer, and U. S. Schubert, *Poly(ethylene glycol) in drug delivery: Pros and cons as well as potential alternatives*, *Angewandte Chemie - International Edition* **49** (2010), no. 36 6288–6308.

[97] E. K. Rowinsky, J. Rizzo, L. Ochoa, C. H. Takimoto, B. Forouzesh, G. Schwartz, L. A. Hammond, A. Patnaik, J. Kwiatek, A. Goetz, L. Denis, J. McGuire, and A. W. Tolcher, *A phase I and pharmacokinetic study of pegylated camptothecin as a 1-hour infusion every 3 weeks in patients with advanced solid malignancies.*, *Journal of clinical oncology : official journal of the American Society of Clinical Oncology* **21** (2003), no. 1 148–157.

[98] A. Patnaik, K. P. Papadopoulos, A. W. Tolcher, M. Beeram, S. Urien, L. J. Schaaf, S. Tahiri, T. Bekaii-Saab, F. M. Lokiec, K. Rezaï, and A. Buchbinder, *Phase i dose-escalation study of EZN-2208 (PEG-SN38), a novel conjugate of poly(ethylene) glycol and SN38, administered weekly in patients with advanced cancer*, *Cancer Chemotherapy and Pharmacology* **71** (2013), no. 6 1499–1506.

[99] I. B. Vergote, J. P. Micha, C. H. Pippitt, G. G. Rao, D. L. Spitz, N. Reed, G. G. Dark, A. Garcia, D. J. Maslyar, and G. J. Rustin, *Phase II study of NKTR-102 in women with platinum-resistant/refractory ovarian cancer.*, *Journal of Clinical Oncology* **28** (may, 2010) 5013.

[100] Y. Matsumura, T. Hamaguchi, T. Ura, K. Muro, Y. Yamada, Y. Shimada, K. Shirao, T. Okusaka, H. Ueno, M. Ikeda, and N. Watanabe, *Phase I clinical trial and pharmacokinetic evaluation of NK911, a micelle-encapsulated doxorubicin.*, *British journal of cancer* **91** (2004), no. 6 1775–1781.

[101] A. Takahashi, Y. Yamamoto, M. Yasunaga, Y. Koga, J. I. Kuroda, M. Takigahira, M. Harada, H. Saito, T. Hayashi, Y. Kato, T. Kinoshita, N. Ohkohchi, I. Hyodo, and Y. Matsumura, *NC-6300, an epirubicin-incorporating micelle, extends the antitumor effect and reduces the cardiotoxicity of epirubicin*, *Cancer Science* **104** (2013), no. 7 920–925.

[102] F. Koizumi, M. Kitagawa, T. Negishi, T. Onda, S. I. Matsumoto, T. Hamaguchi, and Y. Matsumura, *Novel SN-38-incorporating polymeric micelles, NK012, eradicate vascular endothelial growth factor-secreting bulky tumors*, *Cancer Research* **66** (2006), no. 20 10048–10056.

[103] H. Cabral, N. Nishiyama, S. Okazaki, H. Koyama, and K. Kataoka, *Preparation and biological properties of dichloro(1,2-diaminocyclohexane)platinum(II) (DACHPt)-loaded polymeric micelles.*, *Journal of Controlled Release* **101** (2005), no. 1 223–232.

[104] A. V. Boddy, E. R. Plummer, R. Todd, J. Sludden, M. Griffin, L. Robson, J. Cassidy, D. Bissett, A. Bernareggi, M. W. Verrill, and A. H. Calvert, *A phase I and pharmacokinetic study of paclitaxel poliglumex (XYOTAX), investigating both 3-weekly and 2-weekly schedules*, *Clinical Cancer Research* **11** (2005), no. 21 7834–7840.

[105] J. Homsi, G. R. Simon, C. R. Garrett, G. Springett, R. De Conti, A. A. Chiappori, P. N. Munster, M. K. Burton, S. Stromatt, C. Allievi, P. Angiuli, A. Eisenfeld, D. M. Sullivan, and A. I. Daud, *Phase I trial of poly-L-glutamate camptothecin (CT-2106) administered weekly in patients with advanced solid malignancies*, *Clinical Cancer Research* **13** (2007), no. 19 5855–5861.

[106] F. Greco and M. J. Vicent, *Combination therapy: opportunities and challenges for polymer-drug conjugates as anticancer nanomedicines.*, *Advanced drug delivery reviews* **61** (nov, 2009) 1203–13.

[107] Y. Yamamoto, I. Hyodo, M. Takigahira, Y. Koga, M. Yasunaga, M. Harada, T. Hayashi, Y. Kato, and Y. Matsumura, *Effect of combined treatment with the epirubicin-incorporating micelles (NC-6300) and 1,2-diaminocyclohexane platinum (II)-incorporating micelles (NC-4016) on a human gastric cancer model*, *International Journal of Cancer* **135** (2014), no. 1 214–223.

[108] X. Zhang, J. Li, and M. Yan, *Targeted hepatocellular carcinoma therapy: transferrin modified, self-assembled polymeric nanomedicine for co-delivery of cisplatin and doxorubicin*, *Drug Development and Industrial Pharmacy* **9045** (2016), no. May 1–10.

[109] H. Xiao, H. Song, Q. Yang, H. Cai, R. Qi, L. Yan, S. Liu, Y. Zheng, Y. Huang, T. Liu, and X. Jing, *A prodrug strategy to deliver cisplatin(IV) and paclitaxel in nanomicelles to improve efficacy and tolerance*, *Biomaterials* **33** (2012), no. 27 6507–6519.

[110] X. Wei, Y. Wang, X. Xiong, X. Guo, L. Zhang, X. Zhang, and S. Zhou, *Codelivery of a pi Stacked Dual Anticancer Drug Combination with Nanocarriers for Overcoming Multidrug Resistance and Tumor Metastasis*, *Advanced Functional Materials* **26** (2016), no. 45 8266–8280.

[111] K. M. Camacho, S. Kumar, S. Menegatti, D. R. Vogus, A. C. Anselmo, and S. Mitragotri, *Synergistic antitumor activity of camptothecin-doxorubicin combinations and their conjugates with hyaluronic acid.*, *Journal of controlled release : official journal of the Controlled Release Society* **210** (2015) 198–207.

[112] D. Cao, J. He, J. Xu, M. Zhang, L. Zhao, G. Duan, Y. Cao, R. Zhou, and P. Ni, *Polymeric prodrugs conjugated with reduction-sensitive dextrancamptothecin and pH-responsive dextrandoxorubicin: an effective combinatorial drug delivery platform for cancer therapy*, *Polymer Chemistry* **7** (2016) 4198–4212.

[113] S. M. Cohen, R. Mukerji, S. Cai, I. Damjanov, M. L. Forrest, and M. S. Cohen, *Subcutaneous delivery of nanoconjugated doxorubicin and cisplatin for locally advanced breast cancer demonstrates improved efficacy and decreased toxicity at lower doses than standard systemic combination therapy in vivo*, *American Journal of Surgery* **202** (2011), no. 6 646–653.

[114] E. Markovsky, H. Baabur-Cohen, and R. Satchi-Fainaro, *Anticancer polymeric nanomedicine bearing synergistic drug combination is superior to a mixture of individually-conjugated drugs*, *Journal of Controlled Release* **187** (2014) 145–157.

[115] H. Baabur-Cohen, L. I. Vossen, H. R. Krüger, A. Eldar-boock, E. Yeini, N. Landa-Rouben, G. Tiram, S. Wedepohl, E. Markovsky, J. Leor, M. Calderon, and R. Satchi-Fainaro, *In vivo comparative study of distinct polymeric architectures bearing a combination of paclitaxel and doxorubicin at a synergistic ratio*, *Journal of Controlled Release* **257** (2017) 118–131.

[116] T. Lammers, V. Subr, K. Ulbrich, P. Peschke, P. E. Huber, W. E. Hennink, and G. Storm, *Simultaneous delivery of doxorubicin and gemcitabine to tumors in vivo using prototypic polymeric drug carriers*, *Biomaterials* **30** (jul, 2009) 3466–75.

[117] M. Šírová, J. Strohalm, P. Chytil, O. Lidický, J. Tomala, B. íhová, and T. Etrych, *The structure of polymer carriers controls the efficacy of the experimental combination treatment of tumors with HPMA copolymer conjugates carrying doxorubicin and docetaxel*, *Journal of Controlled Release* **246** (2017) 1–11.

[118] Y. Zhou, J. Yang, J. S. Rhim, and J. Kopeček, *HPMA copolymer-based combination therapy toxic to both prostate cancer stem/progenitor cells and differentiated cells induces durable anti-tumor effects*, *Journal of Controlled Release* **172** (2013), no. 3 946–953.

[119] Q. Yang, J. Cai, S. Sun, X. Kang, J. Guo, Y. Zhu, L. Yan, X. Jing, and Z. Wang, *Polymer nanoparticle delivery of dichloroacetate and DACH-Pt to enhance antitumor efficacy and lower systemic toxicity*, *Biomater. Sci.* **4** (2016), no. 4 661–669.

[120] S. Luo, Y. Gu, Y. Zhang, P. Guo, J. F. Mukerabigwi, M. Liu, S. Lei, Y. Cao, H. He, and X. Huang, *Precise Ratiometric Control of Dual Drugs through a Single Macromolecule for Combination Therapy*, *Molecular Pharmaceutics* **12** (2015) 2318–2327.

[121] E. Koziolová, O. Janoušková, L. Cuchalová, Z. Hvězdová, J. Hraběta, T. Eckschlager, L. Sivák, K. Ulbrich, T. Etrych, and V. Šubr, *Overcoming multidrug resistance in Dox-resistant neuroblastoma cell lines via treatment with HPMA copolymer conjugates containing anthracyclines and P-gp inhibitors*, *Journal of Controlled Release* **233** (2016) 136–146.

[122] X. Duan, J. Xiao, Q. Yin, Z. Zhang, H. Yu, S. Mao, Y. Li, M. Medica, and C. Academy, *Smart pH-Sensitive and Temporal- Controlled Polymeric Micelles for E ff ective Combination Therapy of Doxorubicin and Disulfiram*, *ACS Nano* (2013), no. 7 5858–5869.

[123] K. Miller, R. Erez, E. Segal, D. Shabat, and R. Satchi-Fainaro, *Targeting bone metastases with a bispecific anticancer and antiangiogenic polymer-alendronate-taxane conjugate*, *Angewandte Chemie - International Edition* **48** (2009), no. 16 2949–2954.

[124] K. Miller, A. Eldar-boock, D. Polyak, E. Segal, L. Benayoun, Y. Shaked, and R. Satchi-fainaro, *Antiangiogenic Antitumor Activity of HPMA Copolymer-Paclitaxel-Alendronate Conjugate on Breast Cancer Bone Metastasis Mouse Model*, *Molecular Pharmaceutics* **8** (2011) 1052–1062.

[125] C. Clementi, K. Miller, A. Mero, R. Satchi-Fainaro, and G. Pasut, *Dendritic poly(ethylene glycol) bearing paclitaxel and alendronate for targeting bone neoplasms*, *Molecular Pharmaceutics* **8** (2011), no. 4 1063–1072.

[126] K. Miller, C. Clementi, D. Polyak, A. Eldar-Boock, L. Benayoun, I. Barshack, Y. Shaked, G. Pasut, and R. Satchi-Fainaro, *Poly(ethylene glycol)-paclitaxel-alendronate self-assembled micelles for the targeted treatment of breast cancer bone metastases*, *Biomaterials* **34** (2013), no. 15 3795–3806.

[127] W. Xu, R. Thapa, D. Liu, T. Nissinen, S. Granroth, A. Närvänen, M. Suvanto, H. a. Santos, and V.-P. Lehto, *Smart Porous Silicon Nanoparticles with Polymeric Coatings*

for Sequential Combination Therapy, *Molecular Pharmaceutics* **12** (2015), no. 11 4038–4047.

[128] X. Li, N. Wu, Y. Rojanasakul, and Y. Liu, *Selective stamp bonding of PDMS microfluidic devices to polymer substrates for biological applications*, *Sensors and Actuators A: Physical* **193** (apr, 2013) 186–192.

[129] R. Zhang, J. Yang, M. Sima, Y. Zhou, and J. Kopeček, *Sequential combination therapy of ovarian cancer with degradable N-(2-hydroxypropyl)methacrylamide copolymer paclitaxel and gemcitabine conjugates.*, *Proceedings of the National Academy of Sciences of the United States of America* **111** (aug, 2014) 12181–6.

[130] A. Duangjai, K. Luo, Y. Zhou, J. Yang, and J. Kopeček, *Combination cytotoxicity of backbone degradable HPMA copolymer gemcitabine and platinum conjugates toward human ovarian carcinoma cells*, *European Journal of Pharmaceutics and Biopharmaceutics* **87** (2014), no. 1 187–196.

[131] T. C. Chou and P. Talalay, *Quantitative analysis of dose-effect relationships: the combined effects of multiple drugs or enzyme inhibitors*, *Advances in Enzyme Regulation* **22** (jan, 1984) 27–55.

[132] T. R. Fraser, *XXI.An Experimental Research on the Antagonism between the Actions of Physostigma and Atropia*, *Earth and Environmental Science Transactions of the The Royal Society of Edinburgh* **26** (jan, 1871) 529–713.

[133] Z. W. Guo and J. M. Gallo, *Selective protection of 2',2'-difluorodeoxycytidine (gemcitabine)*, *Journal of Organic Chemistry* **64** (1999), no. 22 8319–8322.

[134] S. Cai, S. Thati, T. R. Bagby, H. M. Diab, N. M. Davies, M. S. Cohen, and M. L. Forrest M. Laird, *Localized doxorubicin chemotherapy with a biopolymeric nanocarrier improves survival and reduces toxicity in xenografts of human breast cancer*, *Journal of Controlled Release* **146** (2010), no. 2 212–218.

[135] O. P. Oommen, J. Garousi, M. Sloff, and O. P. Varghese, *Tailored doxorubicin-hyaluronan conjugate as a potent anticancer glyco-drug: An alternative to prodrug approach*, *Macromolecular Bioscience* **14** (2014) 327–333.

[136] C. DeSantis, J. Ma, L. Bryan, and A. Jemal, *Breast cancer statistics, 2013.*, *CA: a cancer journal for clinicians* **64** no. 1 52–62.

[137] *SEER Cancer Statistics: Breast Cancer. National Cancer Institute. Bethesda, MD*, 2014.

[138] A. Ahmad, *Breast Cancer Metastasis and Drug Resistance*. Springer, 2013.

[139] R. M. Neve, K. Chin, J. Fridlyand, J. Yeh, F. L. Baehner, T. Fevr, L. Clark, N. Bayani, J.-P. Coppe, F. Tong, T. Speed, P. T. Spellman, S. DeVries, A. Lapuk, N. J. Wang, W.-L. Kuo, J. L. Stilwell, D. Pinkel, D. G. Albertson, F. M. Waldman, F. McCormick, R. B. Dickson, M. D. Johnson, M. Lippman, S. Ethier, A. Gazdar, and J. W. Gray, *A collection of breast cancer cell lines for the study of functionally distinct cancer subtypes.*, *Cancer cell* **10** (dec, 2006) 515–27.

[140] M. Lacroix and G. Leclercq, *Relevance of breast cancer cell lines as models for breast tumours: an update.*, *Breast cancer research and treatment* **83** (feb, 2004) 249–89.

[141] Deborah L Holliday, *Choosing the right cell line for breast cancer research*, *Breast Cancer Research* **13** (2011), no. 4 215.

[142] J. C. Kathryn, G. Sireesha V, and L. Stanley, *Triple Negative Breast Cancer Cell Lines: One Tool in the Search for Better Treatment of Triple Negative Breast Cancer*, *Breast Disease* **32** (2010), no. 1-2 35–48.

[143] E. Y. Lasfargues, W. G. Coutinho, and E. S. Redfield, *Isolation of two human tumor epithelial cell lines from solid breast carcinomas.*, *Journal of the National Cancer Institute* **61** (oct, 1978) 967–78.

[144] R. Cailleau, R. Young, M. Olive, and J. Reeves, W. J., *Breast Tumor Cell Lines From Pleural Effusions*, *J Natl Cancer Inst* **53** (1974), no. 3 661–674.

[145] M. Martin, T. Pienkowski, J. Mackey, M. Pawlicki, J.-P. Guastalla, C. Weaver, E. Tomiak, T. Al-Tweigeri, L. Chap, E. Juhos, R. Guevin, A. Howell, T. Fornander, J. Hainsworth, R. Coleman, J. Vinholes, M. Modiano, T. Pinter, S. C. Tang, B. Colwell, C. Prady, L. Provencher, D. Walde, A. Rodriguez-Lescure, J. Hugh, C. Loret, M. Rupin, S. Blitz, P. Jacobs, M. Murawsky, A. Riva, and C. Vogel, *Adjuvant docetaxel for node-positive breast cancer.*, *The New England journal of medicine* **352** (2005), no. 22 2302–2313.

[146] M. Martín, M. A. Seguí, A. Antón, A. Ruiz, M. Ramos, E. Adrover, I. Aranda, A. Rodríguez-Lescure, R. Grosse, L. Calvo, A. Barnadas, D. Isla, P. Martinez del Prado, M. Ruiz Borrego, J. Zaluski, A. Arcusa, M. Muñoz, J. M. López Vega, J. R. Mel, B. Munarriz, C. Llorca, C. Jara, E. Alba, J. Florián, J. Li, J. A. López García-Asenjo, A. Sáez, M. J. Rios, S. Almenar, G. Peiró, and A. Lluch, *Adjuvant docetaxel for high-risk, node-negative breast cancer.*, *The New England journal of medicine* **363** (2010), no. 23 2200–2210.

[147] M. Citron and D. Berry, *Randomized trial of dose-dense versus conventionally scheduled and sequential versus concurrent combination chemotherapy as postoperative adjuvant treatment of*, *Journal of clinical oncology* (2003).

[148] E. H. Romond, E. A. Perez, J. Bryant, V. J. Suman, C. E. Geyer, N. E. Davidson, E. Tan-Chiu, S. Martino, S. Paik, P. A. Kaufman, S. M. Swain, T. M. Pisansky, L. Fehrenbacher, L. A. Kutteh, V. G. Vogel, D. W. Visscher, G. Yothers, R. B. Jenkins, A. M. Brown, S. R. Dakhil, E. P. Mamounas, W. L. Lingle, P. M. Klein, J. N. Ingle, and N. Wolmark, *Trastuzumab plus adjuvant chemotherapy for operable HER2-positive breast cancer.*, *The New England journal of medicine* **353** (2005), no. 16 1673–1684.

[149] M. Martin, A. Villar, A. Sole-Calvo, R. Gonzalez, B. Massuti, J. Lizon, C. Camps, A. Carrato, A. Casado, M. T. Candel, J. Albanell, J. Aranda, B. Munarriz, J. Campbell, and E. Diaz-Rubio, *Doxorubicin in combination with fluorouracil and cyclophosphamide (i.v. FAC regimen, day 1, 21) versus methotrexate in combination with fluorouracil and cyclophosphamide (i.v. CMF regimen, day 1, 21) as adjuvant chemotherapy for operable breast cancer: a* , *Annals of oncology: official journal of the European Society for Medical Oncology* **14** (jun, 2003) 833–42.

[150] D. A. Gewirtz, *A critical evaluation of the mechanisms of action proposed for the antitumor effects of the anthracycline antibiotics adriamycin and daunorubicin.*, *Biochemical pharmacology* **57** (apr, 1999) 727–41.

[151] G. Minotti, P. Menna, E. Salvatorelli, G. Cairo, and L. Gianni, *Anthracyclines: molecular advances and pharmacologic developments in antitumor activity and cardiotoxicity.*, *Pharmacological reviews* **56** (jun, 2004) 185–229.

[152] D. J. Slamon, B. Leyland-Jones, S. Shak, H. Fuchs, V. Paton, A. Bajamonde, T. Fleming, W. Eiermann, J. Wolter, M. Pegram, J. Baselga, and L. Norton, *Use of chemotherapy plus a monoclonal antibody against HER2 for metastatic breast cancer that overexpresses HER2.*, *The New England journal of medicine* **344** (mar, 2001) 783–92.

[153] A. D. Seidman, D. Berry, C. Cirrincione, L. Harris, H. Muss, P. K. Marcom, G. Gipson, H. Burstein, D. Lake, C. L. Shapiro, P. Ungaro, L. Norton, E. Winer, and C. Hudis, *Randomized phase III trial of weekly compared with every-3-weeks paclitaxel for metastatic breast cancer, with trastuzumab for all HER-2 overexpressors and random assignment to trastuzumab or not in HER-2 nonoverexpressors: final results of Cancer and Leu*, *Journal of clinical oncology : official journal of the American Society of Clinical Oncology* **26** (apr, 2008) 1642–9.

[154] M. A. Jordan and L. Wilson, *Microtubules as a target for anticancer drugs.*, *Nature Reviews Cancer* **4** (apr, 2004) 253–65.

[155] K. Torres and S. B. Horwitz, *Mechanisms of Taxol-induced Cell Death Are Concentration Dependent*, *Cancer Research* **58** (aug, 1998) 3620–3626.

[156] S. Puhalla and A. Brufsky, *Ixabepilone: A new chemotherapeutic option for refractory metastatic breast cancer*, *Biologics: Targets and Therapy* **2** (2008), no. 3 505–515.

[157] L. T. Vahdat, E. Thomas, R. Li, J. Jassem, H. Gomez, H. Chung, R. Peck, P. Mukhopadhyay, J. Klimovsky, and H. Roché, *Phase III trial of ixabepilone plus capecitabine compared to capecitabine alone in patients with metastatic breast cancer (MBC) previously treated or resistant to an anthracycline and resistant to taxanes*, *Journal of Clinical Oncology* **25** (jun, 2007) 1006.

[158] S. M. Tolaney Dr., J. Najita, J. Sperinde, W. Huang, W. Y. Chen, J. Savoie, M. Fornier, E. P. Winer, C. Bunnell, and I. E. Krop, *A phase II study of ixabepilone and trastuzumab for metastatic HER2-positive breast cancer*, *Annals of Oncology* **24** (2013), no. 7 1841–1847.

[159] J. A. Sparano, E. Vrdoljak, O. Rixe, B. Xu, A. Manikhas, C. Medina, S. C. V. Da Costa, J. Ro, G. Rubio, M. Rondinon, G. P. Manga, R. Peck, V. Poulart, and P. Conte, *Randomized Phase III trial of ixabepilone plus capecitabine versus capecitabine in patients with metastatic breast cancer previously treated with an anthracycline and a taxane*, *Journal of Clinical Oncology* **28** (2010), no. 20 3256–3263.

[160] C. E. Geyer, J. Forster, D. Lindquist, S. Chan, C. G. Romieu, T. Pienkowski, A. Jagiello-Gruszfeld, J. Crown, A. Chan, B. Kaufman, D. Skarlos, M. Campone, N. Davidson, M. Berger, C. Oliva, S. D. Rubin, S. Stein, and D. Cameron, *Lapatinib plus capecitabine for HER2-positive advanced breast cancer.*, *The New England journal of medicine* **355** (2006), no. 26 2733–2743.

[161] G. E. Konecny, M. D. Pegram, N. Venkatesan, R. Finn, G. Yang, M. Rahmeh, M. Untch, D. W. Rusnak, G. Spehar, R. J. Mullin, B. R. Keith, T. M. Gilmer, M. Berger, K. C. Podratz, and D. J. Slamon, *Activity of the dual kinase inhibitor lapatinib (GW572016) against HER-2-overexpressing and trastuzumab-treated breast cancer cells.*, *Cancer research* **66** (mar, 2006) 1630–9.

[162] D. Tripathy, *Overview: gemcitabine as single-agent therapy for advanced breast cancer.*, *Clinical breast cancer* **3** (2002) S8–S11.

[163] K. S. Albain, S. M. Nag, G. Calderillo-Ruiz, J. P. Jordaan, A. C. Llombart, A. Pluzanska, J. Rolski, A. S. Melemed, J. M. Reyes-Vidal, J. S. Sekhon, L. Simms, and J. O'Shaughnessy, *Gemcitabine plus paclitaxel versus paclitaxel monotherapy in patients with metastatic breast cancer and prior anthracycline treatment*, *Journal of Clinical Oncology* **26** (2008), no. 24 3950–3957.

[164] J. a. O'Shaughnessy, S. Vukelja, T. Marsland, G. Kimmel, S. Ratnam, and J. E. Pippen, *Phase II Study of Trastuzumab plus Gemcitabine in Chemotherapy-Pretreated Patients with Metastatic Breast Cancer*, *Clinical Breast Cancer* **5** (2004), no. 2 142–147.

[165] P. Cappella, D. Tomasoni, M. Faretta, M. Lupi, F. Montalenti, F. Viale, F. Banzato, M. D'Incalci, and P. Ubezio, *Cell cycle effects of gemcitabine*, *Int J Cancer* **93** (2001), no. May 401–408.

[166] D. Liu, Y. Chen, X. Feng, M. Deng, G. Xie, J. Wang, L. Zhang, Q. Liu, and P. Yuan, *Micellar nanoparticles loaded with gemcitabine and doxorubicin showed synergistic effect.*, *Colloids and surfaces. B, Biointerfaces* **113** (jan, 2014) 158–68.

[167] S. N. Richter, G. Cartei, M. Nadai, A. Trestin, L. Barzon, M. Palumbo, and G. Palù, *In vitro basis for schedule-dependent interaction between gemcitabine and topoisomerase-targeted drugs in the treatment of colorectal cancer*, *Annals of Oncology* **17** (2006), no. suppl_5 v20–v24.

[168] W. Zoli, L. Ricotti, F. Barzanti, M. Dal Susino, G. L. Frassineti, C. Milandri, D. Casadei Giunchi, and D. Amadori, *Schedule-dependent interaction of doxorubicin, paclitaxel and gemcitabine in human breast cancer cell lines.*, *International Journal of Cancer* **80** (jan, 1999) 413–416.

[169] O. Bar-On, M. Shapira, and D. D. Hershko, *Differential effects of doxorubicin treatment on cell cycle arrest and Skp2 expression in breast cancer cells.*, *Anti-cancer drugs* **18** (2007) 1113–1121.

[170] Y. H. Ling, a. K. El-Naggar, W. Priebe, and R. Perez-Soler, *Cell cycle-dependent cytotoxicity, G2/M phase arrest, and disruption of p34cdc2/cyclin B1 activity induced by doxorubicin in synchronized P388 cells.*, *Molecular pharmacology* **49** (1996) 832–841.

[171] J. L. Tonkinson, J. F. Worzalla, C. H. Teng, and L. G. Mendelsohn, *Cell cycle modulation by a multitargeted antifolate, LY231514, increases the cytotoxicity and antitumor activity of gemcitabine in HT29 colon carcinoma.*, *Cancer research* **59** (1999) 3671–6.

[172] M. B. Chougule, A. R. Patel, T. Jackson, and M. Singh, *Antitumor activity of Noscapine in combination with Doxorubicin in triple negative breast cancer.*, *PloS one* **6** (2011), no. 3 e17733.

[173] A. Bandyopadhyay, L. Wang, J. Agyin, Y. Tang, S. Lin, I.-T. Yeh, K. De, and L.-Z. Sun, *Doxorubicin in combination with a small TGFbeta inhibitor: a potential novel therapy for metastatic breast cancer in mouse models.*, *PloS one* **5** (2010), no. 4 e10365.

[174] I. Y. Kim, Y. S. Kang, D. S. Lee, H. J. Park, E. K. Choi, Y. K. Oh, H. J. Son, and J. S. Kim, *Antitumor activity of EGFR targeted pH-sensitive immunoliposomes encapsulating gemcitabine in A549 xenograft nude mice*, *Journal of Controlled Release* **140** (2009), no. 1 55–60.

[175] S. Miura, Y. Yoshimura, M. Endo, and H. Satoh, *Comparison of 1- (2-deoxy-2-uoro-4-thio-b-d- arabinofuranosyl) cytosine with gemcitabine in its antitumor activity*, *Drugs* **144** (1999) 177–182.

[176] P. K. Julka, R. T. Chacko, S. Nag, R. Parshad, A. Nair, D. S. Oh, Z. Hu, C. B. Koppiker, S. Nair, R. Dawar, N. Dhindsa, I. D. Miller, D. Ma, B. Lin, C. M. Perou, and B. Awasthy, *A phase II study of sequential neoadjuvant gemcitabine plus doxorubicin followed by gemcitabine plus cisplatin in patients with operable breast cancer: prediction of response using molecular profiling*, *British Journal of Cancer* **98** (2008), no. 8 1327–1335.

[177] P. K. Julka, R. T. Chacko, S. Nag, R. Parshad, A. Nair, C. B. Koppiker, F. C. R. Xue, H. Barraclough, N. Dhindsa, A. Seth, A. Majumdar, and T. Puri, *A phase 2 study of sequential neoadjuvant chemotherapy with gemcitabine and doxorubicin followed by gemcitabine and cisplatin in patients with large or locally advanced operable breast cancer: results from long-term follow-up.*, *Breast Cancer* **20** (2013), no. 4 357–62.

[178] A. Passardi, I. Massa, W. Zoli, L. Gianni, C. Milandri, F. Zumaglini, O. Nanni, R. Maltoni, G. L. Frassineti, and D. Amadori, *Phase II study of gemcitabine, doxorubicin and paclitaxel (GAT) as first-line chemotherapy for metastatic breast cancer: a translational research experience.*, *BMC cancer* **6** (jan, 2006) 76.

[179] T. S. Yang, C. H. Wang, R. K. Hsieh, J. S. Chen, and M. C. Fung, *Gemcitabine and doxorubicin for the treatment of patients with advanced hepatocellular carcinoma: A phase I-II trial*, *Annals of Oncology* **13** (2002), no. 11 1771–1778.

[180] G. Perez-Manga, A. Lluch, E. Alba, J. A. Morena-Nogueira, M. Palomera, J. Garcia-Conde, D. Khayat, and N. Rivelles, *Gemcitabine in Combination With Doxorubicin in Advanced Breast Cancer : Final Results of a Phase II Pharmacokinetic Trial*, *Journal of Clinical Oncology* **18** (2000), no. 13 2545–2552.

[181] E. Rivera, V. Valero, B. Arun, M. Royce, R. Adinin, K. Hoelzer, R. Walters, J. L. Wade, L. Pusztai, and G. N. Hortobagyi, *Phase II study of pegylated liposomal doxorubicin in combination with gemcitabine in patients with metastatic breast cancer.*, *Journal of clinical oncology : official journal of the American Society of Clinical Oncology* **21** (sep, 2003) 3249–54.

[182] J. G. Croissant, D. Zhang, S. Alsaiari, J. Lu, L. Deng, F. Tamanoi, J. I. Zink, and N. M. Khashab, *2016, J Control Rel, J Croissant et al, Protein-gold clusters-capped mesoporous silica nanoparticles for drug co-delivery and in-vivo imaging*, *Journal of Controlled Release* **229** (2016) 183–191.

[183] S. Mallik, T. Anajafi, M. D. Scott, S. You, X. Yang, Y. Choi, S. Y. Qian, and S. Mallik, *Acridine Orange Conjugated Polymersomes for Simultaneous Nuclear Delivery of Gemcitabine and Doxorubicin to Pancreatic Cancer Cells*, *Bioconjugate Chemistry* **27** (2016), no. 3 762–771.

[184] R. Nahire, M. K. Haldar, S. Paul, A. H. Ambre, V. Meghnani, B. Layek, K. S. Katti, K. N. Gange, J. Singh, K. Sarkar, and S. Mallik, *Multifunctional polymersomes for*

cytosolic delivery of gemcitabine and doxorubicin to cancer cells, *Biomaterials* **35** (2014), no. 24 6482–6497.

[185] C. Wang, G. Zhang, G. Liu, J. Hu, and S. Liu, *Photo- and thermo-responsive multicompartment hydrogels for synergistic delivery of gemcitabine and doxorubicin*, *Journal of Controlled Release* (2016).

[186] S. Arpicco, P. Milla, B. Stella, and F. Dosio, *Hyaluronic acid conjugates as vectors for the active targeting of drugs, genes and nanocomposites in cancer treatment.*, *Molecules* **19** (jan, 2014) 3193–230.

[187] E. Dalla Pozza, C. Lerda, C. Costanzo, M. Donadelli, I. Dando, E. Zoratti, M. T. Scupoli, S. Beghelli, A. Scarpa, E. Fattal, S. Arpicco, and M. Palmieri, *Targeting gemcitabine containing liposomes to CD44 expressing pancreatic adenocarcinoma cells causes an increase in the antitumoral activity.*, *Biochimica et biophysica acta* **1828** (may, 2013) 1396–404.

[188] H. J. Cho, H. Y. Yoon, H. Koo, S. H. Ko, J. S. Shim, J. H. Lee, K. Kim, I. Chan Kwon, and D. D. Kim, *Self-assembled nanoparticles based on hyaluronic acid-ceramide (HA-CE) and Pluronic for tumor-targeted delivery of docetaxel*, *Biomaterials* **32** (oct, 2011) 7181–7190.

[189] S. Song, H. Qi, J. Xu, P. Guo, F. Chen, F. Li, X. Yang, N. Sheng, Y. Wu, and W. Pan, *Hyaluronan-based nanocarriers with CD44-overexpressed cancer cell targeting*, *Pharmaceutical Research* **31** (may, 2014) 2988–3005.

[190] Y. Zhong, K. Goltsche, L. Cheng, F. Xie, F. Meng, C. Deng, Z. Zhong, and R. Haag, *Hyaluronic acid-shelled acid-activatable paclitaxel prodrug micelles effectively target and treat CD44-overexpressing human breast tumor xenografts in vivo*, *Biomaterials* **84** (2016) 250–261.

[191] S. Cai, Y. Xie, T. R. Bagby, M. S. Cohen, and M. L. Forrest, *Intralymphatic Chemotherapy Using a Hyaluronan-Cisplatin Conjugate*, *Journal of Surgical Research* **147** (2008), no. 2 247–252.

[192] H. Lee, K. Lee, and G. P. Tae, *Hyaluronic acid-paclitaxel conjugate micelles: Synthesis, characterization, and antitumor activity*, *Bioconjugate Chemistry* **19** (2008) 1319–1325.

[193] R. D. Dubey, R. Klippstein, J. T.-W. Wang, N. Hodgins, K.-C. Mei, J. Sosabowski, R. C. Hider, V. Abbate, P. N. Gupta, and K. T. Al-Jamal, *Novel Hyaluronic Acid Conjugates for Dual Nuclear Imaging and Therapy in CD44-Expressing Tumors in Mice In Vivo*, *Nanotheranostics* **1** (2017), no. 1 59–79.

[194] A. Mero and M. Campisi, *Hyaluronic acid bioconjugates for the delivery of bioactive molecules*, *Polymers* **6** (2014) 346–369.

[195] I. Noh, H.-O. Kim, J. Choi, Y. Choi, D. K. Lee, Y.-M. Huh, and S. Haam, *Co-delivery of paclitaxel and gemcitabine via CD44-targeting nanocarriers as a prodrug with synergistic antitumor activity against human biliary cancer*, *Biomaterials* **53** (2015) 763–774.

[196] X. Song, P. L. Lorenzi, C. P. Landowski, B. S. Vig, J. M. Hilfinger, and G. L. Amidon, *Amino acid ester prodrugs of the anticancer agent gemcitabine: Synthesis, bioconversion, metabolic bioevasion, and hPEPT1-mediated transport*, *Molecular Pharmaceutics* **2** (2005), no. 2 157–167.

[197] D. Zhang, D. M. Bender, F. Victor, J. A. Peterson, R. D. Boyer, G. A. Stephenson, A. Azman, and J. R. McCarthy, *Facile rearrangement of N4-(alpha-aminoacyl)cytidines to N-(4-cytidinyl)amino acid amides*, *Tetrahedron Letters* **49** (2008), no. 13 2052–2055.

[198] M. Dasari, A. P. Acharya, D. Kim, S. Lee, S. Lee, J. Rhea, R. Molinaro, and N. Murthy, *H-Gemcitabine: A New Gemcitabine Prodrug for Treating Cancer*, *Bioconjugate Chemistry* **24** (2013), no. 1 4–8.

[199] D. Xin, Y. Wang, and J. Xiang, *The use of amino acid linkers in the conjugation of paclitaxel with hyaluronic acid as drug delivery system: Synthesis, self-assembled property, drug release, and in vitro efficiency*, *Pharmaceutical Research* **27** (2010), no. 2 380–389.

[200] D. A. Yardley, L. Hart, L. Bosserman, M. N. Salleh, D. M. Waterhouse, M. K. Hagan, P. Richards, M. L. Desilvio, J. M. Mahoney, and Y. Nagarwala, *Phase II study evaluating lapatinib in combination with nab-paclitaxel in HER2-overexpressing metastatic breast cancer patients who have received no more than one prior chemotherapeutic regimen*, *Breast Cancer Research and Treatment* **137** (2013), no. 2 457–464.

[201] A. Di Leo, H. L. Gomez, Z. Aziz, Z. Zvirbule, J. Bines, M. C. Arbushites, S. F. Guerrera, M. Koehler, C. Oliva, S. H. Stein, L. S. Williams, J. Dering, R. S. Finn, and M. F. Press, *Phase III, double-blind, randomized study comparing lapatinib plus paclitaxel with placebo plus paclitaxel as first-line treatment for metastatic breast cancer.*, *Journal of clinical oncology* **26** (dec, 2008) 5544–52.

[202] N. M. Iyengar, M. N. Fornier, S. M. Sugarman, M. Theodoulou, T. A. Troso-Sandoval, G. M. D'Andrea, P. R. Drullinsky, D. Gajria, S. B. Goldfarb, E. A. Comen, D. E. Lake, S. Modi, T. A. Traina, M. E. Lacouture, M. F. Chen, S. Patil, J. Baselga, L. Norton, C. A. Hudis, and C. T. Dang, *A Pilot Study of Dose-Dense Paclitaxel with Trastuzumab and Lapatinib for Node-negative HER2-Overexpressed Breast Cancer*, *Clinical Breast Cancer* **16** (2016), no. 2 87–94.

[203] R. S. Finn, M. F. Press, J. Dering, M. Arbushites, M. Koehler, C. Oliva, L. S. Williams, and A. Di Leo, *Estrogen receptor, progesterone receptor, human epidermal growth factor receptor 2 (HER2), and epidermal growth factor receptor expression and benefit from lapatinib in a randomized trial of paclitaxel with lapatinib or placebo as first-line treatment in*, *Journal of clinical oncology* **27** (2009), no. 24 3908–3915.

[204] J. Baselga, I. Bradbury, H. Eidtmann, S. Di Cosimo, E. De Azambuja, C. Aura, H. Gómez, P. Dinh, K. Fauria, V. Van Dooren, G. Aktan, A. Goldhirsch, T. W. Chang, Z. Horváth, M. Coccia-Portugal, J. Domont, L. M. Tseng, G. Kunz, J. H. Sohn, V. Semiglazov, G. Lerzo, M. Palacova, V. Probachai, L. Pusztai, M. Untch, R. D. Gelber, and M. Piccart-Gebhart, *Lapatinib with trastuzumab for HER2-positive early breast cancer (NeoALTTO): A randomised, open-label, multicentre, phase 3 trial*, *The Lancet* **379** (2012), no. 9816 633–640.

[205] A. J. Chien, J. A. Illi, A. H. Ko, W. M. Korn, L. Fong, L.-m. Chen, M. Kashani-Sabet, C. J. Ryan, J. E. Rosenberg, S. Dubey, E. J. Small, T. M. Jahan, N. M. Hylton, B. M. Yeh, Y. Huang, K. M. Koch, and M. M. Moasser, *A phase I study of a 2-day lapatinib chemosensitization pulse preceding nanoparticle albumin-bound Paclitaxel for advanced solid malignancies.*, *Clinical Cancer Research* **15** (sep, 2009) 5569–75.

[206] F. Li, M. Danquah, S. Singh, H. Wu, and R. Mahato, *Paclitaxel- and lapatinib-loaded lipopolymer micelles overcome multidrug resistance in prostate cancer*, *Drug Delivery and Translational Research* **1** (2011), no. 6 420–428.

[207] Y. Wei, S. Xu, F. Wang, A. Zou, S. Zhang, Y. Xiong, S. Cao, Q. Zhang, Y. Wang, and X. Jiang, *A novel combined micellar system of lapatinib and paclitaxel with enhanced antineoplastic effect against human epidermal growth factor receptor-2 positive breast tumor in vitro*, *Journal of Pharmaceutical Sciences* **104** (2015), no. 1 165–177.

[208] P. Dehghan Kelishady, E. Saadat, F. Ravar, H. Akbari, and F. Dorkoosh, *Pluronic F127 polymeric micelles for co-delivery of paclitaxel and lapatinib against metastatic breast cancer: preparation, optimization and in vitro evaluation*, *Pharmaceutical Development and Technology* **20** (2015), no. 8 1009–1017.

[209] P. Dehghankelishadi, E. Saadat, F. Ravar, M. Safavi, M. Pordeli, M. Gholami, and F. A. Dorkoosh, *In vitro and in vivo evaluation of paclitaxellapatinib-loaded F127 pluronic micelles*, *Drug Development and Industrial Pharmacy* **43** (2017), no. 3 390–398.

[210] F. Ravar, E. Saadat, P. D. Kelishadi, and F. A. Dorkoosh, *Liposomal formulation for co-delivery of paclitaxel and lapatinib, preparation, characterization and optimization*, *Journal of Liposome Research* **2104** (2015), no. March 2017 1–13.

[211] H. Hu, Z. Lin, B. He, W. Dai, X. Wang, J. Wang, X. Zhang, H. Zhang, and Q. Zhang, *A novel localized co-delivery system with lapatinib microparticles and paclitaxel*

nanoparticles in a peritumorally injectable in situ hydrogel, *Journal of Controlled Release* **220** (2015) 189–200.

[212] D. Vergara, C. Bellomo, X. Zhang, V. Vergaro, A. Tinelli, V. Lorusso, R. Rinaldi, Y. M. Lvov, S. Leporatti, and M. Maffia, *Lapatinib/Paclitaxel polyelectrolyte nanocapsules for overcoming multidrug resistance in ovarian cancer.*, *Nanomedicine : nanotechnology, biology, and medicine* **8** (aug, 2012) 891–9.

[213] K. J. Lee, J. Yoon, and J. Lahann, *Recent advances with anisotropic particles*, *Current Opinion in Colloid and Interface Science* **16** (2011), no. 3 195–202.

[214] K.-h. Roh, D. C. Martin, and J. Lahann, *Biphasic Janus particles with nanoscale anisotropy.*, *Nature materials* **4** (2005), no. 10 759–763.

[215] S. Rahmani, A. M. Ross, T. H. Park, H. Durmaz, A. F. Dishman, D. M. Prieskorn, N. Jones, R. A. Altschuler, and J. Lahann, *Dual Release Carriers for Cochlear Delivery*, *Advanced Healthcare Materials* **5** (2016), no. 1 94–100.

[216] A. C. Misra, S. Bhaskar, N. Clay, and J. Lahann, *Multicompartmental particles for combined imaging and siRNA delivery*, *Advanced Materials* **24** (2012), no. 28 3850–3856.

[217] S. Rahmani, T. H. Park, A. F. Dishman, and J. Lahann, *Multimodal delivery of irinotecan from microparticles with two distinct compartments*, *Journal of Controlled Release* **172** (2013), no. 1 239–245.

[218] S. Rahmani, S. Ashraf, R. Hartmann, A. F. Dishman, M. V. Zyuzin, C. K. J. Yu, W. J. Parak, and J. Lahann, *Engineering of nanoparticle size via electrohydrodynamic jetting*, *Bioengineering & Translational Medicine* **1** (2016), no. 1 82–93.

[219] S. Rahmani, C. H. Villa, A. F. Dishman, M. E. Grabowski, D. C. Pan, H. Durmaz, A. C. Misra, L. Colón-Meléndez, M. J. Solomon, V. R. Muzykantov, and J. Lahann, *Long-circulating Janus nanoparticles made by electrohydrodynamic co-jetting for systemic drug delivery applications*, *Journal of Drug Targeting* **23** (2015), no. 7-8 750–758.

[220] Y. S. Kwon, S. Y. Chun, K. S. Nam, and S. Kim, *Lapatinib sensitizes quiescent MDA-MB-231 breast cancer cells to doxorubicin by inhibiting the expression of multidrug resistance-associated protein-1*, *Oncology Reports* **34** (2015), no. 2 884–890.

[221] J. Perry, E. Ghazaly, C. Kitromilidou, E. H. McGrowder, S. Joel, and T. Powles, *A Synergistic Interaction between Lapatinib and Chemotherapy Agents in a Panel of Cell Lines Is Due to the Inhibition of the Efflux Pump BCRP*, *Molecular Cancer Therapeutics* **9** (2010), no. 12 3322–3329.

[222] S. Lee, W. Yang, K.-H. Lan, S. Sellappan, K. Klos, G. Hortobagyi, M.-C. Hung, and D. Yu, *Enhanced Sensitization to Taxol-induced Apoptosis by Herceptin Pretreatment in ErbB2-overexpressing Breast Cancer Cells*, *Cancer research* **62** (oct, 2002) 5703–5710.

[223] T. Ahmed, T. S. Shimizu, and R. Stocker, *Bacterial chemotaxis in linear and nonlinear steady microfluidic gradients.*, *Nano letters* **10** (sep, 2010) 3379–85.

[224] N. Li Jeon, H. Baskaran, S. K. W. Dertinger, G. M. Whitesides, L. Van de Water, and M. Toner, *Neutrophil chemotaxis in linear and complex gradients of interleukin-8 formed in a microfabricated device.*, *Nature biotechnology* **20** (aug, 2002) 826–30.

[225] P. J. Hung, P. J. Lee, P. Sabounchi, N. Aghdam, R. Lin, and L. P. Lee, *A novel high aspect ratio microfluidic design to provide a stable and uniform microenvironment for cell growth in a high throughput mammalian cell culture array.*, *Lab on a chip* **5** (jan, 2005) 44–8.

[226] H.-J. Koo, K. V. Waynant, C. Zhang, and P. V. Braun, *Polymer Brushes Patterned with Micrometer-Scale Chemical Gradients Using Laminar Co-Flow.*, *ACS applied materials & interfaces* **6** (jul, 2014) 14320–6.

[227] X. Zhang, X. Gao, L. Jiang, and J. Qin, *Flexible generation of gradient electrospinning nanofibers using a microfluidic assisted approach.*, *Langmuir : the ACS journal of surfaces and colloids* **28** (jul, 2012) 10026–32.

[228] J. N. L. Albert, T. D. Bogart, R. L. Lewis, K. L. Beers, M. J. Fasolka, J. B. Hutchison, B. D. Vogt, and T. H. Epps, *Gradient solvent vapor annealing of block copolymer thin films using a microfluidic mixing device.*, *Nano letters* **11** (mar, 2011) 1351–7.

[229] N. L. Jeon, S. K. W. Dertinger, D. T. Chiu, I. S. Choi, A. D. Stroock, and G. M. Whitesides, *Generation of solution and surface gradients using microfluidic systems*, *Langmuir* **16** (2000), no. 22 8311–8316.

[230] S. K. W. Dertinger, D. T. Chiu, N. L. Jeon, and G. M. Whitesides, *Generation of Gradients Having Complex Shapes Using Microfluidic Networks*, *Analytical Chemistry* **73** (mar, 2001) 1240–1246.

[231] D. Ahmed, C. Y. Chan, S.-C. S. Lin, H. S. Muddana, N. Nama, S. J. Benkovic, and T. J. Huang, *Tunable, pulsatile chemical gradient generation via acoustically driven oscillating bubbles.*, *Lab on a chip* **13** (mar, 2013) 328–31.

[232] D. C.-W. Tan, L.-Y. L. Yung, and P. Roy, *Controlled microscale diffusion gradients in quiescent extracellular fluid.*, *Biomedical microdevices* **12** (jun, 2010) 523–32.

[233] E. Choi, H.-k. Chang, C. Y. Lim, T. Kim, and J. Park, *Concentration gradient generation of multiple chemicals using spatially controlled self-assembly of particles in microchannels.*, *Lab on a chip* **12** (oct, 2012) 3968–75.

[234] J. S. Paustian, R. N. Azevedo, S.-T. B. Lundin, M. J. Gilkey, and T. M. Squires, *Microfluidic Microdialysis: Spatiotemporal Control over Solution Microenvironments Using Integrated Hydrogel Membrane Microwindows*, *Physical Review X* **3** (nov, 2013) 041010.

[235] J. Palacci, C. Cottin-Bizonne, C. Ybert, and L. Bocquet, *Osmotic traps for colloids and macromolecules based on logarithmic sensing in salt taxis*, *Soft Matter* **8** (2012), no. 4 980–994.

[236] J. J. VanDersarl, A. M. Xu, and N. a. Melosh, *Rapid spatial and temporal controlled signal delivery over large cell culture areas.*, *Lab on a chip* **11** (sep, 2011) 3057–63.

[237] S.-Y. Cheng, S. Heilman, M. Wasserman, S. Archer, M. L. Shuler, and M. Wu, *A hydrogel-based microfluidic device for the studies of directed cell migration*, *Lab on a Chip* **7** (2007), no. 6 763–9.

[238] J. Diao, L. Young, S. Kim, E. a. Fogarty, S. M. Heilman, P. Zhou, M. L. Shuler, M. Wu, and M. P. DeLisa, *A three-channel microfluidic device for generating static linear gradients and its application to the quantitative analysis of bacterial chemotaxis*, *Lab on a Chip* **6** (2006), no. 3 381–8.

[239] A. M. Tentori and A. E. Herr, *Photopatterned materials in bioanalytical microfluidic technology.*, *Journal of micromechanics and microengineering : structures, devices, and systems* **21** (may, 2011) 54001.

[240] S. E. Barnes, Z. T. Cygan, J. K. Yates, K. L. Beers, and E. J. Amis, *Raman spectroscopic monitoring of droplet polymerization in a microfluidic device.*, *The Analyst* **131** (sep, 2006) 1027–33.

[241] L. Daubersies, J. Leng, and J.-B. Salmon, *Confined drying of a complex fluid drop: phase diagram, activity, and mutual diffusion coefficient*, *Soft Matter* **8** (2012), no. 21 5923–32.

[242] L. Daubersies, J. Leng, and J.-B. Salmon, *Steady and out-of-equilibrium phase diagram of a complex fluid at the nanolitre scale: combining microevaporation, confocal Raman imaging and small angle X-ray scattering.*, *Lab on a chip* **13** (mar, 2013) 910–9.

[243] K. L. A. Chan and S. G. Kazarian, *FT-IR spectroscopic imaging of reactions in multiphase flow in microfluidic channels.*, *Analytical chemistry* **84** (may, 2012) 4052–6.

[244] D. Schafer, J. A. Squier, J. van Maarseveen, D. Bonn, M. Bonn, and M. Müller, *In situ quantitative measurement of concentration profiles in a microreactor with submicron resolution using multiplex CARS microscopy.*, *Journal of the American Chemical Society* **130** (sep, 2008) 11592–3.

[245] A. Crespi, Y. Gu, B. Ngamsom, H. J. W. M. Hoekstra, C. Dongre, M. Pollnau, R. Ramponi, H. H. van den Vlekkert, P. Watts, G. Cerullo, and R. Osellame, *Three-dimensional Mach-Zehnder interferometer in a microfluidic chip for spatially-resolved label-free detection.*, *Lab on a chip* **10** (may, 2010) 1167–73.

[246] D. J. Bornhop, J. C. Latham, A. Kussrow, D. a. Markov, R. D. Jones, and H. S. Sørensen, *Free-solution, label-free molecular interactions studied by back-scattering interferometry.*, *Science (New York, N.Y.)* **317** (sep, 2007) 1732–6.

[247] A. Ymeti, J. S. Kanger, J. Greve, G. a. J. Besselink, P. V. Lambeck, R. Wijn, and R. G. Heideman, *Integration of microfluidics with a four-channel integrated optical Young interferometer immunosensor.*, *Biosensors & bioelectronics* **20** (jan, 2005) 1417–21.

[248] H. Shao, D. Kumar, S. Feld, and K. Lear, *Fabrication of a FabryPérot cavity in a microfluidic channel using thermocompressive gold bonding of glass substrates*, *Journal of Microelectomechanical Systems* **14** (2005), no. 4 756–762.

[249] G. Gervinskas, P. Trocha, R. Buividas, D. J. Day, E. Scheer, P. Leiderer, and S. Juodkazis, *Fabry-Pérot sensors: microfluidic channels and transparent membranes*, in *Proceedings of SPIE* (S. Juodkazis and M. Gu, eds.), p. 82043Q, International Society for Optics and Photonics, dec, 2011.

[250] J. Tian, Y. Lu, Q. Zhang, and M. Han, *Microfluidic refractive index sensor based on an all-silica in-line Fabry-Perot interferometer fabricated with microstructured fibers.*, *Optics express* **21** (mar, 2013) 6633–9.

[251] K. M. van Delft, J. C. T. Eijkel, D. Mijatovic, T. S. Druzhinina, H. Rathgen, N. R. Tas, A. van den Berg, and F. Mugele, *Micromachined Fabry-Pérot interferometer with embedded nanochannels for nanoscale fluid dynamics.*, *Nano letters* **7** (feb, 2007) 345–50.

[252] J. Israelachvili, *Thin film studies using multiple-beam interferometry*, *Journal of Colloid and Interface Science* **44** (aug, 1973) 259–272.

[253] P. Hariharan, *Basics of interferometry*. Elsevier, Burlington, MA, 2 ed., 2007.

[254] *Concentrative properties of aqueous solutions: density, refractive index, freezing point depression, and viscosity*, in *CRC Handbook of Chemistry and Physics, 85th Edition* (D. R. Lide, ed.). 2004.

[255] G. Ternström, A. Sjöstrand, G. Aly, and Å. Jernqvist, *Mutual Diffusion Coefficients of Water + Ethylene Glycol and Water + Glycerol Mixtures*, *Journal of Chemical & Engineering Data* **41** (jan, 1996) 876–879.

[256] K. Pratt and W. Wakeham, *The mutual diffusion coefficient of ethanol-water mixtures: determination by a rapid, new method*, *Proceedings of the Royal Society London* **336** (1974) 393–406.

[257] K. Pratt and W. Wakeham, *The mutual diffusion coefficient for binary mixtures of water and the isomers of propanol*, *Proceedings of the Royal Society London* **342** (1975) 401–419.

[258] A. C. F. Ribeiro, O. Ortona, S. M. N. Simões, C. I. A. V. Santos, P. M. R. A. Prazeres, A. J. M. Valente, V. M. M. Lobo, and H. D. Burrows, *Binary Mutual Diffusion Coefficients of Aqueous Solutions of Sucrose, Lactose, Glucose, and Fructose in the Temperature Range from (298.15 to 328.15) K*, *Journal of Chemical & Engineering Data* **51** (sep, 2006) 1836–1840.

[259] P. Henrion, *Diffusion in the sucrose+ water system*, *Trans. Faraday Soc.* **60** (1964) 72–4.

[260] M. Castaldi, G. D'Errico, L. Paduano, and V. Vitagliano, *Transport Properties of the Binary System GlucoseWater at 25 C. A Velocity Correlation Study*, *Journal of Chemical & Engineering Data* **43** (jul, 1998) 653–657.

[261] E. Cussler, *Diffusion: Mass transfer in fluid systems*. Cambridge University Press, New York, NY, 1984.

[262] A. Hoffman, *Hydrogels for biomedical applications*, *Advanced drug delivery reviews* (2012).

[263] A. Vashist, A. Vashist, Y. K. Gupta, and S. Ahmad, *Recent advances in hydrogel based drug delivery systems for the human body*, *J. Mater. Chem. B* **2** (2014), no. 2 147–166.

[264] B. Amsden, *Solute Diffusion within Hydrogels. Mechanisms and Models*, *Macromolecules* **31** (1998) 8382–8395.

[265] L. Masaro and X. X. Zhu, *Physical models of diffusion for polymer solutions, gels and solids*, *Progress in Polymer Science* **24** (1999), no. 5 731–775.

[266] S. H. Gehrke, J. P. Fisher, M. Palasis, and M. E. Lund, *Factors determining hydrogel permeability.*, *Annals of the New York Academy of Sciences* **831** (1997), no. 1 179–207.

[267] J. Gutenwik, B. Nilsson, and A. Axelsson, *Effect of hindered diffusion on the adsorption of proteins in agarose gel using a pore model*, *Journal of Chromatography A* **1048** (2004), no. 2 161–172.

[268] J. Wu, A. P. Sassi, H. W. Blanch, and J. M. Prausnitz, *Partitioning of proteins between an aqueous solution and a weakly-ionizable polyelectrolyte hydrogel*, *Polymer* **37** (1996), no. 21 4803–4808.

[269] N. Hirota, Y. Kumaki, T. Narita, J. P. Gong, and Y. Osada, *Effect of Charge on Protein Diffusion in Hydrogels*, *The Journal of Physical Chemistry B* **104** (2000), no. 42 9898–9903.

[270] E. W. Merrill, K. A. Dennison, and C. Sung, *Partitioning and diffusion of solutes in hydrogels of poly(ethylene oxide)*, *Biomaterials* **14** (1993), no. 15 1117–1126.

[271] M. T. Am Ende and N. A. Peppas, *Transport of ionizable drugs and proteins in crosslinked poly(acrylic acid) and poly(acrylic acid-co-2-hydroxyethyl methacrylate) hydrogels. II. Diffusion and release studies*, *Journal of Controlled Release* **48** (1997), no. 1 47–56.

[272] J. Kim and A. Chauhan, *Dexamethasone transport and ocular delivery from poly(hydroxyethyl methacrylate) gels*, *International Journal of Pharmaceutics* **353** (2008), no. 1-2 205–222.

[273] C. C. Peng, M. T. Burke, and A. Chauhan, *Transport of topical anesthetics in vitamin e loaded silicone hydrogel contact lenses*, *Langmuir* **28** (2012), no. 2 1478–1487.

[274] J. L. Stringer and N. A. Peppas, *Diffusion of small molecular weight drugs in radiation-crosslinked poly(ethylene oxide) hydrogels*, *Journal of Controlled Release* **42** (1996), no. 2 195–202.

[275] D. E. Liu, C. Kotsmar, F. Nguyen, T. Sells, N. O. Taylor, J. M. Prausnitz, and C. J. Radke, *Macromolecule Sorption and Diffusion in HEMA / MAA Hydrogels*, *Industrial & Engineering Chemistry Research* **52** (2013), no. 50 18109–18120.

[276] D. E. Liu, T. J. Dursch, N. O. Taylor, S. Y. Chan, D. T. Bregante, and C. J. Radke, *Diffusion of water-soluble Sorptive drugs in HEMA/MAA hydrogels*, *Journal of Controlled Release* **239** (2016) 242–248.

[277] C.-C. Lin and K. S. Anseth, *PEG hydrogels for the controlled release of biomolecules in regenerative medicine.*, *Pharmaceutical research* **26** (mar, 2009) 631–43.

[278] H. Liu and M. Hai, *Investigation on the interaction between sodium dodecyl sulfate and nonionic polymer with electrolytes by viscosity and surface tension*, *Journal of Chemical and Engineering Data* **55** (2010), no. 1 354–357.

[279] J. Kim, Y. Gao, C. Hebebrand, E. Peirtsegaele, and M. E. Helgeson, *Polymersurfactant complexation as a generic route to responsive viscoelastic nanoemulsions*, *Soft Matter* **9** (2013), no. 29 6897.

[280] A. Banerjee, I. Williams, R. N. Azevedo, M. E. Helgeson, and T. M. Squires, *Soluto-inertial phenomena: Designing long-range, long-lasting, surface-specific interactions in suspensions*, *Proceedings of the National Academy of Sciences* **113** (2016), no. 31 8612–8617.

[281] H. Yasuda, a. Peterlin, C. Colton, K. Smith, and E. Merril, *Permeability of solutes through hydrogel polymer membranes*, *Makromol. Chem* **118** (1969), no. 3086 19–35.

[282] Y. H. Wu, H. B. Park, T. Kai, B. D. Freeman, and D. S. Kalika, *Water uptake, transport and structure characterization in poly(ethylene glycol) diacrylate hydrogels*, *Journal of Membrane Science* **347** (2010) 197–208.

[283] K. R. Rupprecht, E. Z. Lang, S. D. Gregory, J. M. Bergsma, T. D. Rae, and J. R. Fishpaugh, *A precise spectrophotometric method for measuring sodium dodecyl sulfate concentration*, *Analytical Biochemistry* **486** (2015) 78–80.